REPORT DOCUMENTATION PAGE

Form Approved OMB NO. 0704-0188

1. REPORT DATE (DD-MM-YYYY)	2. REPORT TYPE	3. DATES COVERED (From - To)
30-08-2019	Final Report	1-Apr-2016 - 31-Mar-2019

4. TITLE AND SUBTITLE	5a. CONTRACT NUMBER
Final Report: Nonlinear constitutive modeling of viscoelastic foams: Application to impact protection	W911NF-16-1-0084
	5b. GRANT NUMBER
	5c. PROGRAM ELEMENT NUMBER 611102
6. AUTHORS	5d. PROJECT NUMBER
	5e. TASK NUMBER
	5f. WORK UNIT NUMBER

7. PERFORMING ORGANIZATION NAMES AND ADDRESSES	8. PERFORMING ORGANIZATION REPORT NUMBER
Brown University Office of Sponsored Projects Box 1929 Providence, RI 02912 -9093	
9. SPONSORING/MONITORING AGENCY NAME(S) AND ADDRESS (ES) U.S. Army Research Office P.O. Box 12211 Research Triangle Park, NC 27709-2211	10. SPONSOR/MONITOR'S ACRONYM(S) ARO 11. SPONSOR/MONITOR'S REPORT NUMBER(S) 68393-EG.3

12. DISTRIBUTION AVAILIBILITY STATEMENT

Approved for public release; distribution is unlimited.

13. SUPPLEMENTARY NOTES

The views, opinions and/or findings contained in this report are those of the author(s) and should not contrued as an official Department of the Army position, policy or decision, unless so designated by other documentation.

14. ABSTRACT

15. SUBJECT TERMS

16. SECURITY CLASSIFICATION OF:			17. LIMITATION OF ABSTRACT	15. NUMBER OF PAGES	19a. NAME OF RESPONSIBLE PERSON
a. REPORT	b. ABSTRACT	c. THIS PAGE			David Henann
UU	UU	UU	UU		19b. TELEPHONE NUMBER 401-863-1475

RPPR Final Report
as of 16-Sep-2019

Agency Code:

Proposal Number: 68393EG **Agreement Number: W911NF-16-1-0084**

INVESTIGATOR(S):

Name: David Henann
Email: David_Henann@brown.edu
Phone Number: 4018631475
Principal: Y

Organization: **Brown University**
Address: Office of Sponsored Projects, Providence, RI 029129093
Country: USA

DUNS Number: 001785542 EIN: 050258809

Report Date: 30-Jun-2019 Date Received: 30-Aug-2019

Final Report for Period Beginning 01-Apr-2016 and Ending 31-Mar-2019

Title: Nonlinear constitutive modeling of viscoelastic foams: Application to impact protection

Begin Performance Period: 01-Apr-2016 **End Performance Period:** 31-Mar-2019

Report Term: 0-Other

Submitted By: David Henann Email: David_Henann@brown.edu
Phone: (401) 863-1475

Distribution Statement: 1-Approved for public release; distribution is unlimited.

STEM Degrees: 1 **STEM Participants:** 2

Major Goals: Open-cell elastomeric foams are materials made up of two continuous phases: a polymeric elastomer matrix and a connected, air-filled pore space. Due to their elastomeric matrix and porous structure, these materials are highly compliant and capable of undergoing large, reversible deformations involving substantial changes in volume. Moreover, due to the viscoelasticity of the elastomeric matrix, many elastomeric foams display a highly dissipative, rate-dependent mechanical response, manifesting in rate-dependence of the stress/strain response and hysteresis under reversed loading. These materials are widely-used in situations, in which both compliance and energy dissipation are necessary, e.g., impact protection, cushioning, and vibration damping, and appear in a wide variety of specific applications, such as personal protective equipment.

The scientific objective of this project was to develop a comprehensive methodology for the experimental characterization and constitutive modeling of non-localizing, isotropic, open-cell elastomeric foam materials under large deformations. The constitutive model was informed by a comprehensive experimental program and validated against experiments in inhomogeneous deformation modes. Our systematic approach integrates experiments, theory, and computation, as follows:

1 - Homogeneous experiments: We have experimentally characterized several densities of PORON XRD (an isotropic, polyurethane-based elastomeric foam) in simple compression/tension over a finite-deformation range – axial stretches ranging from roughly 0.3 to 1.5 – and a strain-rate range of 10e-3 to 10e-1 1/s.

2 - Constitutive modeling: We have formulated a general three-dimensional, finite-deformation, nonlinear constitutive model for the mechanical response of elastomeric foams, applicable to a wide range of specific elastomeric foam materials. Our theoretical approach is based upon a decomposition of the mechanical response into a hyperelastic, equilibrium response and a series of dissipative, non-equilibrium contributions. Both the equilibrium response as well as the non-equilibrium mechanisms account for coupled isochoric and volumetric deformation. Model formulation is based upon experimental input generated in the previous bullet point.

3 - Validation through inhomogeneous experiments and simulation: Constitutive modeling is then thoroughly validated against inhomogeneous loading situations not used for model development. We have performed quasi-static finite-deformation experiments of (1) spherical and conical indentation, (2) simple-shear-like deformation without and with pre-compression, and (3) tension of a specimen with circular holes to validate aspects of the model. Through corresponding finite-element simulations (achieved using an implementation of the constitutive theory in Abaqus), the model is validated over its calibrated range.

RPPR Final Report

as of 16-Sep-2019

Accomplishments: The accomplishments of this project are described in detail in the attached final report. The major contributions of this work are briefly summarized below:

1 - Advances in experimental methods for porous foam materials: We have introduced a new 2D DIC technique, based on our previously developed finite deformation IDM FIDVC technique, that incorporates the concept of a cross-correlation quality factor. Two q-factors were utilized in this new qDIC technique, the peak-to-correlation-energy ratio and the peak-to-information-entropy. The q-factors improved the robustness and accuracy of the DIC for distorted speckle patterns arising from large finite deformations. By including the q-factors as a metric for image decorrelation, an intelligent hybrid incremental-cumulative switching scheme was implemented. The new qDIC algorithm showed improved performance over our previous FIDIC across all validation and benchmarking cases, i.e., rigid-body, homogeneous and inhomogenous modes of deformation displacement fields. To increase access to DIC and promote engagement in the development process of tools widely used in experimental mechanics, the open source codebase for qDIC is freely available to download from the Franck Lab GitHub page (https://github.com/FranckLab).

2 - Homogeneous experimental testing: We presented an extensive new set of quasi-static (low strain-rate) experiments on three densities of the polyurethane-based, open-cell elastomeric foam ``Poron XRD''. Experiments consisted of homogeneous simple compression/tension as well as three types of inhomogeneous experiments: spherical and conical indentation, simple-shear-like deformation without and with pre-compression, and tension of a specimen with circular holes.

3 - Hyperelastic model development: A phenomenological, isotropic, finite-deformation, hyperelastic constitutive model based on invariants of the logarithmic, Hencky strain was proposed. A key simplifying assumption of our modeling approach is that volumetric/distortional coupling only involves low-order dependence on the magnitude of distortional deformation - which leads to a more straightforward interpretation of the fitting functions and a systematic path for material parameter estimation from simple compression/tension data. In compression and tension, the fitted model for each of the three densities of Poron XRD faithfully captures the nonlinear stress versus axial strain and lateral strain versus axial strain responses, in particular, the tension/compression asymmetry featuring a nearly-flat plateau regime in compression. All simple compression/tension experimental data and resulting fitted model data for Poron XRD has been made available to the community via GitHub (https://github.com/FranckLab).

4 - Validation: The constitutive model was implemented in Abaqus/Standard using a user-material subroutine, which was used to obtain model predictions in inhomogeneous deformation settings for the purpose of validation. The model predictions were shown to be consistent with experimental data in the inhomogenous validation cases across compression, shear, and tension-dominated settings. The user-material subroutine implementation of the constitutive model and sample input files for several of validation cases have been made available to the community (https://github.com/HenannResearchGroup).

5 - Characterization and viscoelastic constitutive modeling at elevated strain-rates: The characterization and modeling methodology has been extended to the elevated strain-rate range of 10e-3 to 10e-1 1/s. We presented a set of homogeneous simple compression/tension experiments on the high-density Poron XRD foam and proposed a phenomenological, finite-deformation viscoelastic constitutive model, based on a decomposition of the response into a hyperelastic, equilibrium response and a series of dissipative, non-equilibrium mechanisms. The fitted model captures the observed rate-dependence of the engineering stress/strain response, including hysteretic behavior upon unloading, as well as the lateral strain versus axial strain response.

Training Opportunities: Two graduate students, Alexander Landauer and Xiuqi Li, have worked on the project over its course, focusing on constitutive modeling and experimental characterization, respectively. The two students received one-on-one mentoring from the PI and co-PI. In addition to one-on-one meetings, the students present weekly updates of their research at meetings attended by all four participants in the project and receive feedback not only on their scientific work but also their communication skills. Over the course of the project, the students gave presentations at several professional conferences, such as the Society of Engineering Science Technical Meeting and the Society of Experimental Mechanics Annual Conference and Exposition. Conference presentations are listed under the Dissemination section. One of the students, Alexander Landauer, completed his PhD thesis and defended on August 15, 2019. The other student, Xiuqi Li, is on track to complete her PhD thesis in the coming year.

RPPR Final Report
as of 16-Sep-2019

Results Dissemination: Papers published:

- Alexander K. Landauer, Mohak Patel, David L. Henann, and Christian Franck. A q-factor-based digital image correlation algorithm (qDIC) for resolving finite deformations with degenerate speckle patterns. Experimental Mechanics 58 (2018) 815-830.

- Alexander K. Landauer, Mohak Patel, David L. Henann, and Christian Franck. Experimental characterization and hyperelastic constitutive modeling of open-cell elastomeric foams. Journal of the Mechanics and Physics of Solids, doi:10.1016/j.jmps.2019.103701.

Conference presentations:

- Alexander Landauer, Xiuqi Li, Christian Franck, and David L. Henann. Mechanical characterization and modeling of viscoelastic polyurethane foams. ASME International Mechanical Engineering Congress and Exposition, Phoenix, AZ, November 17, 2016 (Oral Presentation).

- Xiuqi Li, Alexander Landauer, Christian Franck, and David L. Henann. Micromechanically-based development of a hyperelastic model for foam rubbers. SES Technical Meeting, Boston, MA, July 28, 2017 (Oral Presentation).

- Alexander Landauer, Mohak Patel, Xiuqi Li, David L. Henann, and Christian Franck. A Q-factor-based Digital Image Correlation Algorithm (qDIC) for resolving finite deformations in poor signal to noise environments. SES Technical Meeting, Boston, MA, July 28, 2017 (Oral Presentation).

- Xiuqi Li, Alexander Landauer, Christian Franck, and David L. Henann. Mechanical characterization and hyperelastic constitutive modeling of elastomeric foams. ASME International Mechanical Engineering Congress and Exposition, Tampa, FL, November 9, 2017 (Oral Presentation).

- Alexander K. Landauer. Correlation Quality Factors Improve Motion Reconstruction in Digital Image and Volume Correlation Measurements. SEM Annual Conference and Exposition, Greenville, SC, June 4, 2018 (Oral Presentation).

- Christian Franck, Alexander Landauer, Xiuqi Li, David L. Henann. qDIC-based Experimental Characterization of Hyperelastic, Highly Compressible Elastomeric Foams. SEM Annual Conference and Exposition, Greenville, SC, June 5, 2018 (Oral Presentation).

- Alexander Landauer. Porous material deformation characterized by 3D light field imaging. 16th Pan-American Congress of Applied Mechanics, Ann Arbor, MI, May 20, 2019 (Oral Presentation).

- Alexander Landauer, Xiuqi Li, David L. Henann, and Christian Franck. Characterization of the Viscoelastic Response of Strain-Rate Sensitive Elastomeric Foams. SEM Annual Conference and Exposition, Reno, NV, June 6, 2019 (Oral Presentation).

PhD thesis:

- Alexander Landauer. Elastic Foam Characterization for Rate-Dependent Nonlinear Material Model Development. Brown University, August 15, 2019.

Honors and Awards: David Henann – Pi Tau Sigma Gold Medal (ASME, 2016)
Christian Franck – Young Investigator Award (SEM, 2017)
Alexander Landauer – NIST National Academies/National Research Council (NRC) Postdoctoral Program (2019)

Protocol Activity Status:

Technology Transfer: Nothing to Report

PARTICIPANTS:

Participant Type: PD/PI

Participant: David Henann
Person Months Worked: 1.00 **Funding Support:**
Project Contribution:
International Collaboration:
International Travel:
National Academy Member: N
Other Collaborators:

Participant Type: Co PD/PI
Participant: Christian Franck
Person Months Worked: 1.00 **Funding Support:**
Project Contribution:
International Collaboration:
International Travel:
National Academy Member: N
Other Collaborators:

Participant Type: Graduate Student (research assistant)
Participant: Xiuqi Li
Person Months Worked: 12.00 **Funding Support:**
Project Contribution:
International Collaboration:
International Travel:
National Academy Member: N
Other Collaborators:

Participant Type: Graduate Student (research assistant)
Participant: Alexander Landauer
Person Months Worked: 12.00 **Funding Support:**
Project Contribution:
International Collaboration:
International Travel:
National Academy Member: N
Other Collaborators:

ARTICLES:

RPPR Final Report
as of 16-Sep-2019

Publication Type: Journal Article Peer Reviewed: Y **Publication Status:** 1-Published
Journal: Journal of the Mechanics and Physics of Solids
Publication Identifier Type: DOI Publication Identifier: 10.1016/j.jmps.2019.103701
Volume: 133 Issue: First Page #: 103701
Date Submitted: 9/5/19 12:00AM Date Published: 8/23/19 12:00PM
Publication Location:

Article Title: Experimental characterization and hyperelastic constitutive modeling of open-cell elastomeric foams

Authors: Alexander K. Landauer, Xiuqi Li, Christian Franck, David L. Henann

Keywords: foam material; constitutive behavior; elastic material; finite strain; mechanical testing

Abstract: Open-cell elastomeric foams exhibit mechanical behavior marked by compressibility and coupling between the volumetric and distortional responses. We present a methodology for the experimental characterization and constitutive modeling of non-localizing, isotropic, open-cell elastomeric foams under quasi-static, equilibrium loading. We conduct large-deformation, homogeneous simple compression/tension experiments on three relative densities of a polyurethane-based elastomeric foam to inform a phenomenological, isotropic, hyperelastic constitutive model. The model is based on the invariants of the logarithmic strain and accounts for compressibility and volumetric-distortional coupling. To validate the predictive capability of the model, we consider three types of validation experiments that involve inhomogeneous deformation: spherical and conical indentation, simple-shear-like deformation without and with a fixed amount of pre-compression, and tension of a specimen with circular holes.

Distribution Statement: 1-Approved for public release; distribution is unlimited.
Acknowledged Federal Support: **Y**

Final report

Nonlinear constitutive modeling of viscoelastic foams: Application to impact protection (Grant #68393-EG)

David L. Henann and Christian Franck* (Brown University)
Attention: Dr. Denise Ford (Research Area 1.2)

Executive Summary

Open-cell elastomeric foams are materials made up of two continuous phases: a polymeric elastomer matrix and a connected, air-filled pore space. Due to their elastomeric matrix and porous structure, these materials are highly compliant and capable of undergoing large, reversible deformations involving substantial changes in volume. Moreover, due to the viscoelasticity of the elastomeric matrix, many elastomeric foams display a highly dissipative, rate-dependent mechanical response, manifesting in rate-dependence of the stress/strain response and hysteresis under reversed loading. These materials are widely-used in situations, in which both compliance and energy dissipation are necessary, e.g., impact protection, cushioning, and vibration damping, and appear in a wide variety of specific applications, such as personal protective equipment. In this project, we developed a comprehensive methodology for the experimental characterization and constitutive modeling of non-localizing, isotropic, open-cell elastomeric foam materials under large deformations and quasi-static strain-rates.

First, accurate kinematic measurements are needed for robust experimental characterization of soft materials, such as elastomeric foams. The digital image correlation (DIC) technique – a non-contact, full-field displacement and strain measurement method – is ideal for this purpose. However, issues unique to elastomeric foams – such as surface roughness, compressibility, and large deformations – limit the signal quality of such measurements, and these demanding experimental conditions necessitate a custom DIC algorithm. The typical local DIC algorithm relies on image subset matching using cross-correlations to determine the motion field between images of a speckle pattern. We developed a new open-source DIC algorithm (qDIC) that incorporates cross-correlation quality factors (q-factors), which are specifically designed to assess the quality of the reconstructed displacement estimate during the motion reconstruction process. A q-factor provides a robust assessment of the uniqueness and sharpness of the cross-correlation peak, and thus a quantitative estimate of the subset-based displacement measure per given image subset and level of applied deformation. We showed that the incorporation of energy- and entropy-based q-factor metrics leads to substantially improved displacement predictions, lower noise floor, and reduced decorrelation even at significant levels of image distortion or poor speckle quality.

Next, using the new qDIC technique, we conducted large-deformation, homogeneous simple compression/tension experiments on three relative densities of a polyurethane-based elastomeric foam to inform a phenomenological, isotropic, hyperelastic constitutive model for the equilibrium (low strain-rate) response of elastomeric foams. The model is based on the invariants of the logarithmic strain and accounts for high compressibility and strong volumetric-distortional coupling. To

*Now at the University of Wisconsin-Madison.

validate the predictive capability of the model, we considered three types of validation experiments that involve inhomogeneous deformation: spherical and conical indentation, simple-shear-like deformation both without and with a fixed amount of pre-compression, and tension of a specimen with circular holes. We compared load-displacement responses as well as full displacement fields from the validation experiments against corresponding model predictions obtained using finite-element-based numerical simulations and demonstrated that the model is capable of accurately capturing the experimental response.

Finally, we extended our experimental characterization and constitutive modeling approach to the elevated strain-rate range of 10^{-3}-$10^{-1}\,\mathrm{s}^{-1}$. We conducted a set of large-deformation, homogeneous simple compression/tension experiments on one density of the polyurethane-based elastomeric foam over this elevated strain-rate range. We then developed a phenomenological, finite-deformation viscoelastic constitutive model, based on a decomposition of the response into a hyperelastic, equilibrium response – using our new hyperelastic model – and a series of dissipative, non-equilibrium mechanisms. The fitted model captures the observed rate-dependence of the engineering stress/strain response, including hysteretic behavior upon unloading, as well as the lateral strain versus axial strain response.

In short, this project addressed the need for a methodology for experimental characterization and predictive constitutive modeling of light-weight elastomeric foam materials and resulted in the first comprehensive constitutive model for open-cell, polyurethane-based foams. Army applications, specifically in impact protection, involve complex loadings and severe constraints, and hence, this predictive model will be a boon to the design of Army protective equipment, enabling weight and volume reduction of equipment and eliminating the need for expensive testing.

Contents

1 Introduction

Open-cell elastomeric foams are materials consisting of two continuous phases: a polymeric elastomer and a connected gas-filled pore space. Due to the elastomeric matrix and porous structure, these materials are highly compliant and capable of undergoing large, reversible deformations involving substantial volume change (Gibson and Ashby, 1997; Hilyard and Cunningham, 1994). Moreover, due to the viscoelasticity of the elastomeric matrix, many elastomeric foams display a dissipative mechanical response, manifesting in rate-dependence and hysteresis under reversed loading. Elastomeric foams are widely used in situations in which compliance, compressibility, and energy dissipation are necessary, such as in impact protection and cushioning, and appear in a wide variety of applications, including personal protective equipment.

The mechanical behavior of open-cell elastomeric foams is quite complex, involving large deformations, substantial compressibility, and strong tension/compression asymmetry. Consider, as an illustrative example, the behavior of a commercially-available impact protection foam – a polyurethane-based, open-cell elastomeric foam that has been the focus of our work – whose response to external load is demonstrated in Fig. 1 for three different relative densities (Poron XRD, Rogers Corp, Rogers, CT). For each density, Fig. 1 shows the experimentally-measured engineering stress versus axial engineering strain response in the left column and the corresponding lateral engineering strain versus axial engineering strain response in the right column for quasi-static (low strain-rate) simple compression/tension (experimental details are discussed in Section 6). The response in all three cases is highly nonlinear and displays substantial asymmetry between tension and compression. In particular, in compression, the response is initially linear, but as the axial strain magnitude increases, the response gradually transitions into a "plateau" in which both the axial stress and the lateral strain vary minimally as the axial strain magnitude increases. The plateau regime is generally associated with buckling in the elastomeric-matrix microstructure and concomitant closure of the pore space (Gibson and Ashby, 1997). Importantly, the plateau regime for Poron XRD is not completely flat, and we observe homogeneous deformation with no evidence of strain localization in our compression experiments. Then, as the material is compressed beyond the plateau regime, rapid stiffening is observed in the axial stress response. However, in tension neither a plateau regime nor a rapidly stiffening response is observed. Upon unloading in both compression and tension, some hysteresis but no permanent set is observed at this low strain-rate. For higher strain-rates, the stress/strain response is rate-dependent and displays increased hysteresis – but still no permanent set – upon reversed loading. This is in contrast to the inelastic behavior of crushable foams (e.g., Neilsen et al., 1995; Zhang et al., 1997; Deshpande and Fleck, 2001; Liu and Subhash, 2004), which yield and display permanent set upon unloading. In this project, we focused on the mechanics of elastic foams that exhibit neither deformation localization nor permanent set.

Due to the complexity of the mechanical behavior of open-cell elastomeric foams, developing predictive constitutive models remains challenging despite the ubiquity of these materials. There is a substantial history of constitutive modeling of porous and foam materials (e.g., Gibson and Ashby, 1997; Gong et al., 2005). First, we discuss on hyperelastic modeling approaches for capturing the equilibrium, elastic response described in the preceding paragraph. Commonly, Ogden-type hyperelastic models (Ogden, 1972a; Storakers, 1986), which utilize a phenomenological free-energy density function that depends on the principal stretches, are used to capture data for highly-compressible foams in the large-stretch regime (e.g., Jemiolo and Turteltaub, 2000; Mills and Gilchrist, 2000; Briody et al., 2012; Chen et al., 2012; Ju et al., 2013). While models of this type are

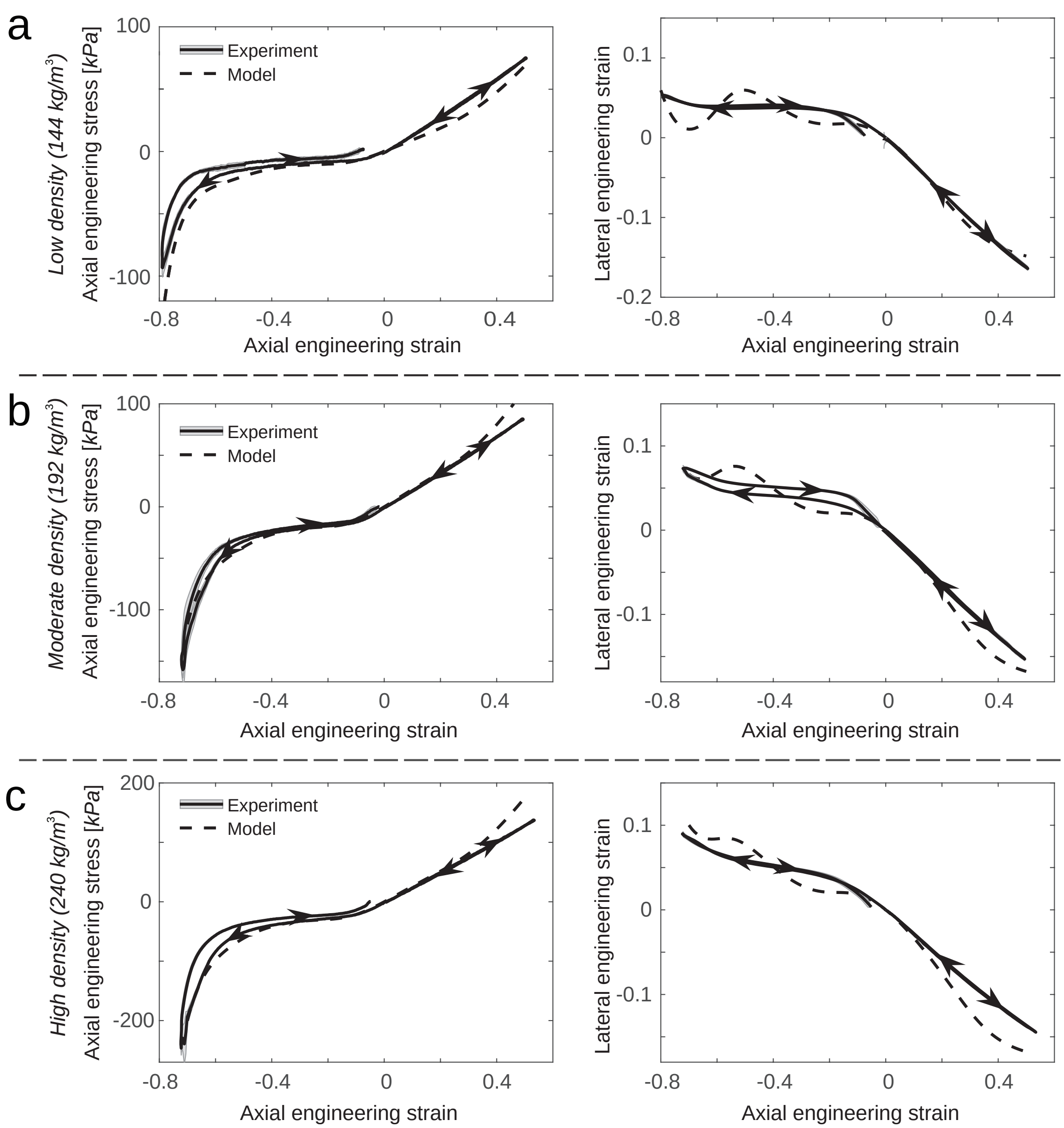

Figure 1: (Left) Axial engineering stress versus axial engineering strain curves and (right) lateral engineering strain versus axial engineering strain curves for polyurethane-based, open-cell elastomeric foams of (a) low ($144\,\mathrm{kg/m^3}$), (b) moderate ($192\,\mathrm{kg/m^3}$), and (c) high ($240\,\mathrm{kg/m^3}$) density with the same matrix composition. The solid lines with shaded error areas (one standard deviation, nine experiments) indicate experimental data, and the dashed lines are constitutive model fits. Note that for (a), (b), and (c), the stress axes differ in range. For all densities, note both the plateau regime in compression in both the stress and lateral strain histories as a function of axial strain, and the small lateral strain magnitudes under large axial strain magnitudes as characteristic features of deformation in open-cell elastomeric foams.

capable of describing the features of the equilibrium, hyperelastic response of open-cell elastomeric foams, they can be unwieldy to work with (e.g., Petre et al., 2006; Widdle Jr. et al., 2008). Material parameter fitting is a challenge, and a fitted model typically has minimal extrapolative potential, often providing poor predictions in loading scenarios not used in fitting or becoming unstable beyond the fitted range. Other hyperelasticity models utilize free-energy density functions that depend on the principal invariants of the Cauchy-Green deformation tensors, including the well-known Blatz-Ko hyperelasticity model (Blatz and Ko, 1962) and its extensions (e.g., Murphy, 2000; Ciambella and Saccomandi, 2014). The Blatz-Ko model can capture the response of compressible foams up to moderate stretches but is not equipped to describe large-stretch behavior – specifically, the plateau regime in compression. Other invariant-based approaches include polynomial-type free-energy density functions (Yang and Shim, 2004; Anani and Alizadeh, 2011). Furthermore, homogenization-based approaches (Danielsson et al., 2004; Lopez-Pamies and Ponte Castañeda, 2007a,b; Shrimali et al., 2019) consider porous elastomers with microstructures consisting of closed-cell pores and result in explicit, invariant-based hyperelastic models that incorporate the effects of microstructural features, such as the void volume fraction, pore size dispersion, and pore shape. However, since these models invoke closed-cell microstructures in their derivations and do not account for buckling in elastomeric-matrix ligaments, they cannot be expected to capture the response of highly-compressible, open-cell foams under large compressive deformations – in particular, the response in the plateau regime. We note that fully-micromechanical models, based on strut-type unit cells (e.g., Shulmeister et al., 1998; Wang and Cuitiño, 2000; Brydon et al., 2005; Sabuwala and Gioia, 2013; Gong and Kyriakides, 2005) or unit cells involving cylindrical or spherical voids (e.g., Guo et al., 2008; Chen et al., 2018; Shrimali et al., 2019), have been used to capture the equilibrium behavior of elastomeric foams with different microstructures. While such modeling approaches provide important physical insights, they are computationally expensive to apply to problems involving length scales much greater than the characteristic size of the porous microstructure, and hence, explicit hyperelastic models are valuable. Second, we discuss viscoelastic modeling approaches for capturing the rate-dependent response of open-cell elastomeric foams at elevated strain-rates. Less work exists on this point. A common approach is to adapt techniques from linear viscoelasticity, such as using a Prony series to describe a time-dependent modulus in a hyperelasticity model (e.g., Yang and Shim, 2004; Anani and Alizadeh, 2011; Briody et al., 2012; Ju et al., 2015); however, this approach is not thermodynamically-consistent. A more rigorous modeling approach has been undertaken by Bergström (2006) with some success.

The purpose of this project was to develop a comprehensive methodology for the experimental characterization and constitutive modeling of non-localizing, isotropic, open-cell elastomeric foam materials. One challenge is obtaining accurate full-field kinematic measurements, which is crucial to ensure that deformation is homogeneous during characterization experiments and to measure both axial and lateral strains under large deformations. Digital image correlation (DIC) has become a widely utilized non-contact, full-field displacement measurement technique for obtaining accurate material kinematics. Despite the significant advances made to date, high resolution reconstruction of finite deformations for images with intrinsically low quality speckle patterns or poor signal-to-noise content – both of which occur for elastomeric foams – has not been fully addressed. In particular, large image distortions imposed by materials undergoing finite deformations create significant challenges for most classical DIC approaches. To address this issue, we developed a new open-source DIC algorithm (qDIC) that incorporates cross-correlation quality factors (q-factors), which are specifically designed to assess the quality of the reconstructed displacement estimate during the motion reconstruction process. A q-factor provides a robust assessment of the uniqueness and sharpness of the cross-correlation peak, and thus a quantitative estimate of the subset-based displacement measure per given image subset and level of applied deformation. The incorporation of energy- and entropy-based q-factor metrics leads to substantially improved displacement predictions, lower noise floor, and reduced decorrelation even at significant levels of image distortion or poor speckle quality. Furthermore, q-factors can be utilized as a quantitative metric for constructing a hybrid incremental-cumulative displacement correlation scheme for accurately resolving very large homogeneous and inhomogeneous deformations, even in the presence of significant image data loss. This contribution is described in Landauer et al. (2018).

Next, hyperelastic model development and material parameter estimation are informed by the homogeneous simple compression/tension experiments shown in Fig. 1. Rather than basing our isotropic hyperelasticity model on the principal invariants of the Cauchy-Green deformation tensors, our hyperelastic model adopts those of Criscione et al. (2000), which are based on the invariants of the logarithmic strain (Hencky, 1931, 1933). This choice is made on pragmatic grounds, since the logarithmic-strain invariants of Criscione et al. (2000) may be associated with specific aspects of deformation, enabling a more straightforward path to choosing and calibrating phenomenological fitting functions that capture experimental data. For perspective, a number of isotropic, logarithmic-strain-based hyperelasticity models have been proposed in the literature. Importantly, the work of Anand (1979, 1986), showed that a simple quadratic free-energy function employing the logarithmic strain is capable of capturing experimental data for a wide class of materials in the moderate-stretch regime. Since then, various models have been successfully applied to incompressible and nearly-incompressible materials in the large-stretch regime (e.g., Kakavas, 2000; Diani and Gilormini, 2005; Horgan and Murphy, 2009; Xiao, 2013). Our work extends this literature towards a constitutive modeling approach for highly-compressible materials. We decompose the free-energy function into terms that represent the coupled volumetric/distortional, purely distortional, and purely volumetric contributions to the response and select phenomenological fitting functions for each term that capture our experimental data for open-cell polyurethane foam. We perform several validation tests that probe the predictive capability of the hyperelastic model in a variety of deformation modes, namely, compression, shear, and tension-dominated situations. This work is described in Landauer et al. (2019).

Then, we extend the experimental characterization and constitutive modeling approach to elevated strain-rates (10^{-3}-10^{-1} s^{-1}). Our constitutive modeling approach is based upon a phenomenological decomposition of the response into a hyperelastic, equilibrium response and a series of dissipative, non-equilibrium contributions (e.g., Bergström and Boyce, 1998; Reese and Govindjee, 1998; Anand et al., 2009; Chester, 2012; Toyjanova et al., 2014). Our intent is to provide an accessible characterization and modeling framework for highly-compressible elastic materials, and we expect that future works will consider other specific, perhaps micromechanically-based, fitting functions and extend the approach to other open-cell elastomeric foam materials.

The remainder of this report is organized as follows. Section 2 provides background on digital image correlation (DIC) and describes the need for improved techniques. In Section 3, the basic 2D adaptation of Fast Iterative Digital Volume Correlation (FIDIVC) and its features are described; the addition of q-factors for both point-wise quality assurance and global reference switching is introduced; and the incremental-cumulative finite deformation summation scheme is discussed. Section 4 presents the validation of the new q-factor based 2D-FIDVC (qDIC) algorithm. Our new algorithm is used to experimentally measure the full-field deformation of an elastomeric foam in

Section 5, which features poor speckle characteristics due to the high porosity of the material. In Section 6, we describe our experimental program for characterizing the mechanical response of the isotropic, polyurethane-based elastomeric foam, marketed under the “Poron XRD” trademark, using homogeneous simple compression/tension experiments as well as our approach for validation testing. Then, in Section 7, we present our hyperelastic constitutive model for the elastic behavior of isotropic, open-cell elastomeric foams and apply the model to Poron XRD. In Section 8, the constitutive model is validated in three configurations: first, spherical and conical indentation, second, simple-shear-like deformation both without and with fixed-displacement pre-compression, and third, tension of a specimen with circular holes, where the conditions are specifically chosen to probe the model in compression, shear, and tension-dominated situations. In Section 9, we discuss issues of stability and compare the proposed model with other important models from the literature. Section 10 describes the experimental characterization of Poron XRD at elevated strain-rates (10^{-3}-10^{-1} s^{-1}) and presents our viscoelastic model for isotropic, open-cell elastomeric foams. Finally, we close with a summary and a discussion of the limits of the modeling approach and future research directions in Section 11.

2 Background on digital image correlation (DIC)

Digital image correlation (DIC) is a longstanding image based non-contact, full-field displacement measurement technique (Chu et al., 1985; Sutton et al., 1983; Schreier et al., 2009). Extensive effort has been expended in developing and improving DIC algorithms, quantifying errors, and extending the technique to 3D surface (3D-DIC) (Luo et al., 1993; Sutton, 2013) and full volumetric (digital volume correlation) measurement (Bay et al., 1999; Bay, 2008; Franck et al., 2007; Pierron et al., 2011; Fu et al., 2013) since its inception. Substantial prior work has focused on accurately resolving small (i.e., subpixel), spatially varying displacement fields of either unknown (local DIC) or known (global DIC) character and/or boundary conditions (Schreier et al., 2009; Hild and Roux, 2012). Several contemporary algorithms have implemented DIC-based tracking for large finite deformations and have discussed the ongoing challenges distinct to resolving finite deformations within the DIC framework (Blaber et al., 2015; Pan et al., 2012).

In the DIC method, intensity variations in an image of the specimen surface encode a unique descriptor for a particular sub-region of the image. The intensity variations can be due to natural specimen texture, or, more typically, a pattern of random “speckles" that are transferred to the specimen prior to testing. Full-field displacements are determined by tracking the motion of image subsets between an image of the reference (i.e., undeformed) configuration and a current (i.e., deformed) configuration by cross-correlation of image subset pairs (Schreier et al., 2009). Usually, a transform, or shape, function of order n is adopted to map the reference configuration to the deformed configuration, and the transformation parameters are iteratively adjusted to minimize a cross-correlation matching error metric. Subpixel accuracy is achieved by interpolation of the pixel-level cross-correlation.

For finite deformations, particularly in compression dominated modes, the matching between reference and deformed configurations is more challenging for three primary reasons: (1) the speckle pattern becomes highly distorted, (2) the portion of the image field of view subtended by the specimen is reduced, and (3) large 0^{th}-order (rigid body) motion exists. Each of these effects are apparent in the diagram of Fig. 2. Thus, for tracking large finite deformations, DIC algorithms have used “reliability-guided" non-linear optimization schemes to obtain the parameters of a higher-order shape function and utilized incremental (image n is compared to image $n + 1$) or hybridized incremental-cumulative image switching, rather than a purely cumulative (image 0 is compared to image n) based comparison (Blaber et al., 2015; Pan et al., 2012). Cumulatively switching offers lower error than incremental switching until image decorrelation begins, and it is therefore important to carefully choose reference update points in a hybrid scheme.

A copious portion of the literature concerning DIC has discussed error sources, propagation, mitigation, and error evaluation strategies at various measurement stages throughout the system, from the speckling pattern to the final processing steps (Wang et al., 2016; Reu, 2013; Hild and Roux, 2012; Schreier et al., 2009). The accuracy of the displacement reconstruction depends upon the quality and characteristics (e.g., the gradients of intensity captured in a subset) of the intensity pattern from which image subsets are sampled, in addition to the algorithm details (Estrada and Franck, 2015; Pan et al., 2010; Dong and Pan, 2017; Crammond et al., 2013). For finite deformations, speckle pattern quality can become degenerate, particularly in the transverse directions to the principal deformation axis. The plots of spatial variation in intensity and intensity gradient in Fig. 2 illustrate this in a synthetically generated image pair. Speckle pattern degeneracy as a result of deformation-based image distortion or from regions that contain insufficient gradient information has been quantified by a number of techniques. These were recently reviewed in detail by Dong and Pan (2017) and by Crammond et al. (2013). The speckle pattern assessment techniques provide a quality parameter either for an entire image or an image subset using either image intensity distributions, e.g., by measuring intensity gradients (Pan et al., 2008, 2010), fluctuations (Hua et al., 2011), speckle size/morphology (Yaofeng and Pang, 2007; Lecompte et al., 2006; Crammond et al., 2013), or entropy (Yaofeng and Pang, 2007; Liu et al., 2015), or correlation-based heuristics, such as autocorrelation peak sharpness (Bossuyt, 2013) or autocorrelation tallest peak to secondary

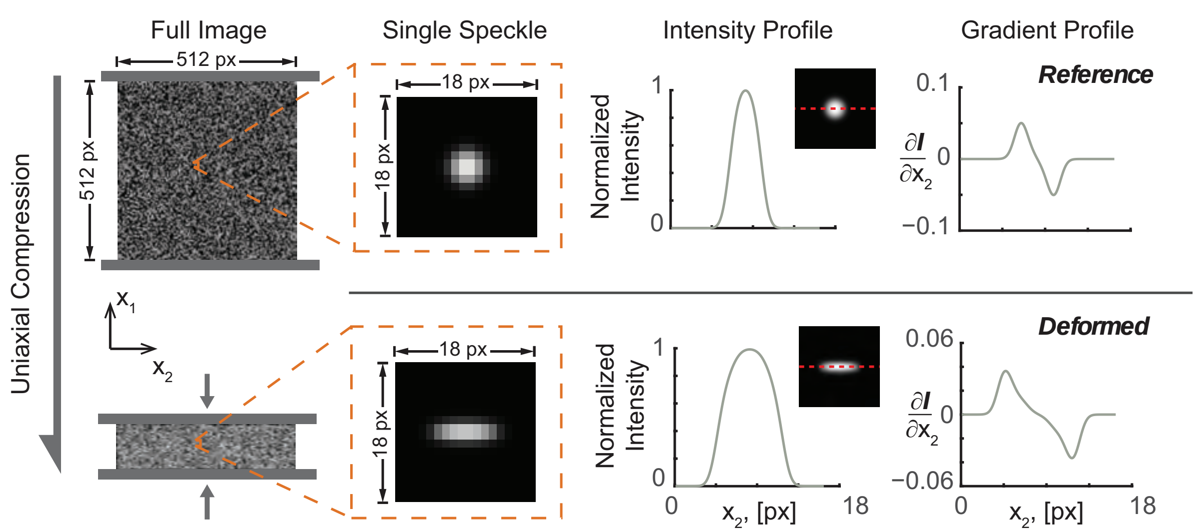

Figure 2: Schematic and synthetically generated example images undergoing finite deformation uniaxial compression. At large deformations, the speckles and pattern become highly anisotropic. In the transverse direction, the information-carrying content of the speckle, the grayscale gradient, becomes degenerate in both its magnitude and sharpness (slope), decreasing the overall quality of the motion reconstruction process

peak ratio (Stoilov et al., 2012). These metrics provide a deterministic way for quantifying the information carrying potential and signal-to-noise ratio within a DIC image. The autocorrelation-based measures are related to the idea of cross-correlation quality factors used within particle image velocimetry algorithms that shall be discussed in detail later in this work.

To approach the issue of poor regions for correlation or decorrelation due to image distortion within the DIC algorithm, several authors (Pan et al., 2012; Blaber et al., 2015) have developed “reliability-guided" DIC (RG-DIC) implementations. In the RG-DIC technique, peak magnitudes for zero-normalized cross-correlation (ZNCC) below a predefined threshold are used as indicators for points to be skipped and re-evaluated when a better initial guess for certain shape function parameters is available from nearby interrogation points. While the peak-value of the ZNCC offers a basic indication of decorrelation, it is an incomplete metric of the signal quality of matching. More complete evaluation of the loss-of-signal in cross-correlation is possible with the use of a cross-correlation quality-factor (q-factor) (Kumar and Hassebrook, 1990; Xue et al., 2014). There are four common q-factor metrics. First, the simplest and least informative is the peak-to-peak ratio, in which the highest peak in the cross-correlation space is compared to the second highest peak (Javidi, 1989). Second, the peak to root-mean-square ratio compares the overall signal noise magnitude to the magnitude of the peak (Horner and Leger, 1985). Third, the peak to correlation energy quantifies the distinctness of the primary peak energy from the correlation energy (Kumar and Hassebrook, 1990). The fourth, peak to information entropy, compares the random correlation noise to the height of the primary correlation peak (Xue et al., 2014). The final three q-factors are based on analytical derivation from signal processing theory and the definition of signal-to-noise. When incorporated into a DIC algorithm, q-factors may provide a reliable and mathematically robust method for evaluating each measurement point, which we show to improve the measurement accuracy.

The algorithm developed in this project utilizes a non-traditional technique originally introduced for particle velocimetry applications of image correlation, termed the iterative deformation method (IDM) (Scarano, 2002) in place of non-linear optimization of the deformation shape functions. With the IDM a simple matching function with no optimization parameter is employed to estimate the motion field, and this motion field estimate is used to iteratively warp the reference and deformed configuration images. The total deformation field motion tracking problem is thus linearized into a series of 0^{th}-order deformation steps, such that large, arbitrary deformations are reconstructed accurately and few switching points are required in the hybridized reference updating scheme.

3 q-factor based digital image correlation (qDIC)

The new algorithm that forms the basis for this work introduces q-factors to a computationally efficient implementation for large deformation DIC. Considered in addition to the underlying IDM framework, this improves the overall accuracy for finite deformation measurements in environments with poor speckle patterns. The q-factor is used as a loss-of-signal metric in both local evaluation of individual measurement points and global evaluation of image-pair decorrelation. For local assessment, the individual displacement measurement point quality is estimated and used as a threshold criterion. To reconstruct large deformations with global quality information, the algorithm employs a hybrid incremental-cumulative image pairing scheme with switching informed by the global q-factor assessment.

3.1 Fast iterative digital image correlation

A 2D version of FIDVC, which is extensively described by Bar-Kochba et al. (2015), formed the basis for this work. The basic 3D to 2D conversion of FIDVC is termed FIDIC; both FIDVC and FIDIC are made freely available[1] to the community. The FIDVC algorithm is a Fast Fourier Transform-based implementation of the IDM (Jambunathan et al., 1995; Scarano, 2002) designed to reconstruct large deformations in 3D volumes, the salient features of which are summarized below and outlined in the *Modified 2D-FIDVC framework* box of Fig. 3. For either technique an image pair containing an image of the reference configuration of the specimen (the reference image) and a second image of the deformed configuration (the deformed image) are analyzed to reconstruct the encoded differential motion field.

During DIC processing, the images are divided into overlapping subsets with a given initial square subset size, w_i, and spacing, d_i, and the motion of each subset center is tracked via a matching function. The final resolution of any subset-based algorithm is determined by the final subset size and spacing. In the IDM scheme, the subset size and spacing are refined to w and d respectively during the iterative deformation process, allowing low spatial frequency components of the displacement to be captured in initial iterations, and higher frequency signals to be reconstructed as the process continues. In general, the motion field estimate $d\mathbf{u}$ between subsets of image n and $n+m$ for iteration k is computed via

$$I_n^{k-1}(\mathbf{x}) \otimes \hat{I}_{n+m}^{k-1}(\mathbf{x}) \rightarrow d\mathbf{u} \tag{3.1}$$

where $\otimes$ is the cross-correlation operator, and k is an integer counter starting at one. See the diagram in Fig. 4(a) for a schematic description of this process. The image subset windows are treated independently such that computation is highly parallelizable. In the cross-correlation space returned for each subset, a 3$^{\text{rd}}$-order Gaussian polynomial is fit to the region surrounding the peak value to determine the peak location, and hence the displacement estimate, with subpixel resolution. To improve accuracy and compensate for the moving-average nature of the cross-correlation function, a modular transfer function with weighing support for frequency fluctuation suppression as given by Nogueira et al. (2005), i.e.,

$$\begin{aligned}\omega(\mathbf{x}) = \Big(\prod_{i=1}^{3} 12\Big[\Big|\frac{x_i}{w}\Big|^2 - 12\Big|\frac{x_i}{w}\Big| + 3 + 0.15\cos(4\pi x_i/w) \\ + 0.2\cos(6\pi x_i/w) + 0.1\cos(8\pi x_i/w) + 0.05\cos(10\pi x_i/w)\Big]\Big)^{1/2}\end{aligned} \tag{3.2}$$

is incorporated into the cross-correlation operation, such that the complete formulation becomes

$$C(d\mathbf{u}) = \sum_{\mathbf{x}=-w/2}^{w/2} \omega(\mathbf{x}) f(\mathbf{x}) \cdot \omega(\mathbf{x}+d\mathbf{u}) \hat{f}(\mathbf{x}+d\mathbf{u}) \tag{3.3}$$

where f and $\hat{f}$ are the reference and deformed image subsets. As in Bar-Kochba et al. (2015), the cross-correlation C may be computed in Fourier space from

$$C(d\mathbf{u}) = \mathcal{F}^{-1}\{\mathcal{F}\{\omega(\mathbf{x}) f(\mathbf{x})\} \times \mathcal{F}\{\omega(\mathbf{x}+d\mathbf{u}) \hat{f}(\mathbf{x}+d\mathbf{u})\}\}, \tag{3.4}$$

[1]See GitHub, https://github.com/FranckLab

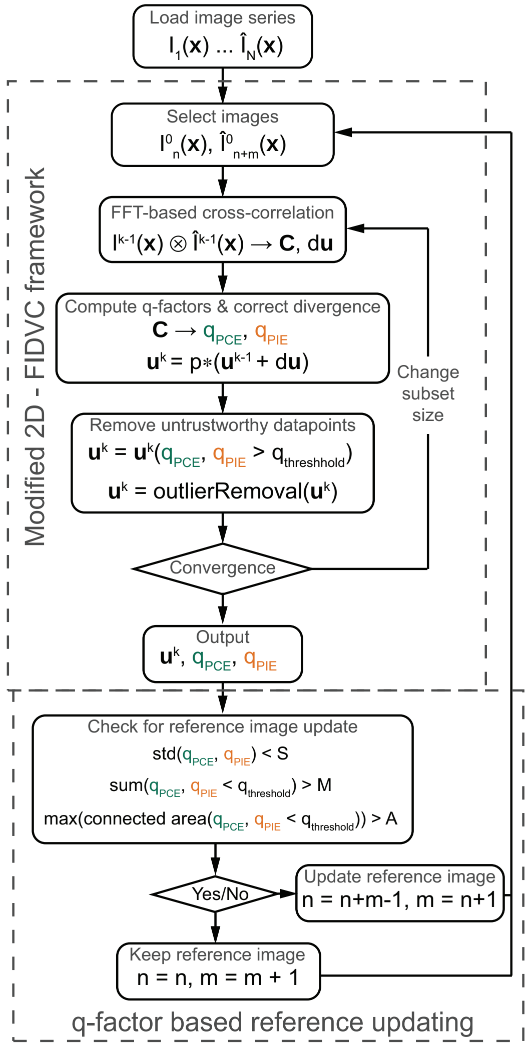

Figure 3: Algorithm outline showing the major steps taken to measure displacements from an image series containing N images. In the *Modified 2D - FIDVC framework* block, the displacement between an image pair consisting of a reference image (I_n, the n'th image in the series) and a deformed image ($\hat{I}_{n+m}$, the $(n+m)$'th image in the series) is measured and q-factors for each measurement point are calculated. The displacement measurement is conducted in an iterative deformation method framework where at each iteration, k, the images are warped with the displacement estimate from the previous step until they converge to identical images. After initial convergence, the process is repeated with decreasing subset size and spacing until the final desired resolution is reached. In *q-factor based reference updating*, several q-factor based measurement quality metrics are checked for indications of decorrelation between the reference and deformed images. The algorithm checks whether the standard deviation of q-factor values, the total number of low q-factors, and the maximum connected area of low q-factors is small. If any of the checks fail, a reference update is performed wherein the first image in the image pair is updated to the $(n+m-1)$'th image in the series. If no reference update is needed the second image in the image pair is updated with the next image in the series

where $\mathcal{F}$ indicates a Fourier transform. A normalized cross correlation formulation, which is used throughout this work, is optionally available although at considerable time-cost, in which case the Matlab formulation (based on Lewis (1995)) is directly utilized.

From the incremental motion field $d\mathbf{u}$, the total motion field must be built up by a series of linearized iterative steps. This is accomplished through the summation of the incremental fields,

$$\mathbf{u}^k = \sum_k \mathbf{u}^{k-1} + d\mathbf{u} \tag{3.5}$$

and symmetric warping of the original reference image (I^k) and deformed image ($\hat{I}^k$) by the new total displacement field estimate, i.e.,

$$\begin{aligned} I^k(\mathbf{x}) &= I^0(\mathbf{x} - \mathbf{u}^k/2) \\ \hat{I}^k(\mathbf{x}) &= \hat{I}^0(\mathbf{x} + \mathbf{u}^k/2). \end{aligned} \tag{3.6}$$

The warping function utilizes bicubic spline interpolation since the increased computation cost of the higher-order interpolant for 2D images is negligible.

In general, the IDM has no guarantee of convergence and can become unstable, so a specialized low-pass convolution filter $p(\xi)$ (Schrijer and Scarano, 2008) is applied during displacement summation, such that (3.5) becomes

$$\mathbf{u}^k = p * \left(\sum_k \mathbf{u}^{k-1} + d\mathbf{u} \right). \tag{3.7}$$

Additional spurious displacement measurement points (due to, e.g., mismatching or poorly defined cross-correlation peaks) are removed with a universal median test (Westerweel and Scarano, 2005) and replaced with an energy-minimizing plate metaphor-based interpolant using the displacement values from the adjacent measurement points.

Following the procedure described above, the algorithm continues iterating until a stopping criterion for convergence is met. Since the IDM attempts to warp the images toward each other, the relevant measure for ending iterations is image similarly. For this implementation, an error-rate based formulation is adopted where the change in normalized sum-of-squared-difference between the images in the image pair is tested against the stopping criterion. A stopping criterion is defined for each spatial resolution and as the criteria are met, the algorithm refines subset size and spacing until the final resolution, which is set by the user, e.g., $w = 16$ pixels (px) and $d = 8$ px, is achieved. After final convergence, the displacement field is output. For an image series, FIDIC can be run in either incremental or cumulative mode. Total displacements are either given by summation of the displacement increments (incremental) or computed directly with reference to the initial stress-free configuration (cumulative).

3.2 Cross-correlation assessment via q-factors

As shown in Figs. 3 and 4(a) , the incremental displacement measure, $d\mathbf{u}$, at each iteration step k is obtained by cross-correlating the subset image intensities in the reference and deformed images. A key improvement of the q-factor based qDIC method over the basic FIDIC is to add an additional level of signal quality assessment during cross-correlation via a performance

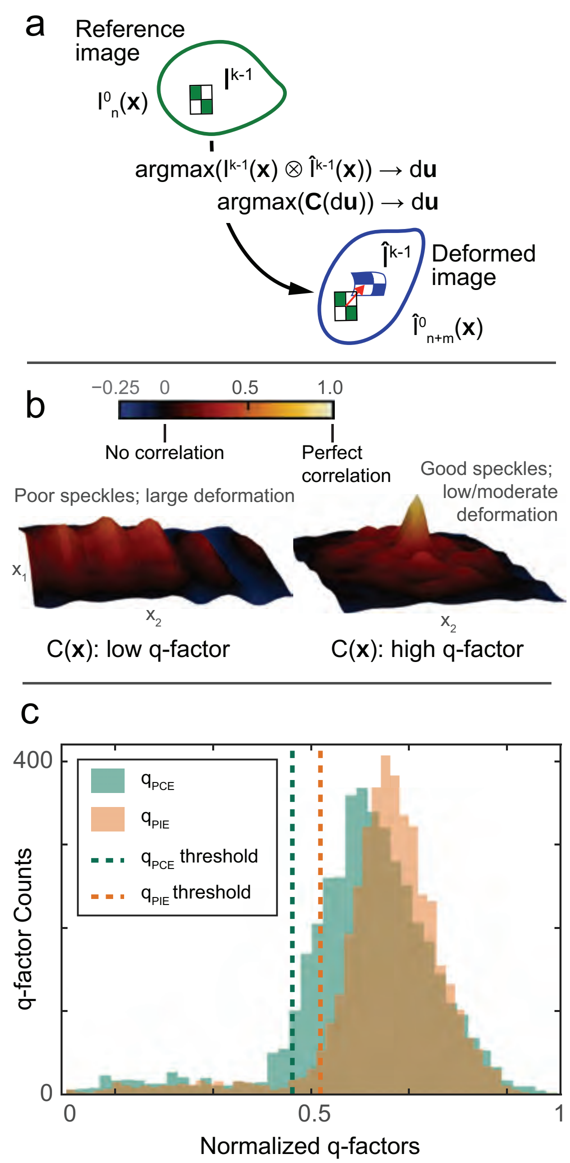

Figure 4: Quality factor (q-factor) based assessment in DIC. (a) For a given iteration, k, of mapping a reference image I_n^0 (the n'th image an image series) to a deformed image $\hat{I}_{n+m}^0$ (the $(n+m)$'th image) the displacement vector at a point in the image plane, $\mathbf{x}$, is given by the offset of the peak of the cross-correlation function between the images at that point. (b) Whether the peak of the cross-correlation function is sharp, strong, and uniquely defined depends upon the local image conditions. A cross-correlation quality factor (q-factor) is needed to assess if the cross-correlation function topology contains information sufficient to accurately and reliably measure the corresponding subset displacement. (c) In this work, two q-factors have been used as reliable metrics to judge cross-correlation quality. These are the peak-to-correlation-energy ratio (q_{PCE}) and the peak-to-information-entropy ratio (q_{PIE}). All q-factors are normalized, and a quality threshold is established as one standard deviation below the mean of the best fit Gaussian to each q-factor histogram

metric. Various metrics to estimate the signal-to-noise-ratio (SNR) of cross-correlation between two signals are well established (Kumar and Hassebrook, 1990). These techniques have been discussed extensively in the context of particle image velocimetry (PIV) for estimating motion fields in fluid flows (Charonko and Vlachos, 2013). By quantifying the sharpness and distinctness of the cross-correlation coefficient peak and comparing it to the underlying signal, these metrics offer a robust technique to establish the quality of the cross-correlation itself, hence the term quality-factors of cross-correlation. The q-factors directly evaluate the ability of the cross-correlation coefficient, $C(\mathbf{x})$, to give accurate and reliable displacement measurement results, and assess how trustworthy a particular motion estimate is. The distinction between a high and low q-factor is illustrated in Fig. 4(b).

Two q-factors are of particular note, the peak-to-correlation-energy ratio (q_{PCE}) and the peak-to-information-entropy ratio (q_{PIE}). The physical origin of both these methods is rooted in information theory, and they have been shown to offer reliable performance in providing accurate displacement measures over a variety of image sets (Kumar and Hassebrook, 1990; Xue et al., 2014). The q_{PCE} compares the magnitude of the strongest peak to the normalized correlation signal energy by computing

$$q_{PCE} = \frac{|C(\mathbf{x})_{max}|^2}{\frac{1}{L}\left(\sum_L |C(\mathbf{x})|^2\right)} \tag{3.8}$$

where $C(\mathbf{x})$ is the cross-correlation coefficient and L is the size of the cross-correlation space. Based on the Shannon entropy (Shannon, 1948) of the image cross-correlation coefficient, the q_{PIE} is computed from a 30-bin histogram of the cross-correlation space,

$$\frac{1}{q_{PIE}} = -\sum_{i=1}^{30} p_i \log p_i \tag{3.9}$$

where p_i is the probability of finding a given point in the i^{th} bin. The remaining two q-factors, first-to-second peak and peak to root-mean-squared signal, capture fewer features of the correlation space ($C(\mathbf{x})$) in a single metric and were found to offer less robust performance. Both the q-factors can be normalized in the range $[0, 1]$ for a given population, e.g., the set of q-factors drawn from correlating all subset points within an image pair.

Once q-factors have been computed, a threshold level must be defined to distinguish high and low quality correlation points, which in turn define a cutoff for reliable versus unreliable displacement estimates. For a given iteration in the IDM, the number of cross-correlated measurement points and q-factors is set by the image size and subset spacing. The population of q-factors for each q-factor type generally features a normal, Gaussian-like distribution sampled about an unknown mean. As one or more image regions become decorrelated, e.g., due to image degradation, the distribution becomes bi-modal. To establish an appropriate q-factor threshold, a maximum likelihood estimator (MLE) was used to fit a bi-modal Gaussian density function to the q-factor histogram. If the mean $\pm$ standard deviation of the the two estimated peaks overlapped, no second peak was recorded, and the MLE was recomputed for a uni-modal Gaussian density function. For either case, the quality threshold was the largest-q-factor-value peak minus one standard deviation (see Fig. 4(c)). Measurement points failing the quality threshold test were discarded from the displacement field and replaced with interpolated values via the plate-metaphor interpolation scheme as described in Section 3.1, supported by points with high q-factor scores. Edge points and discarded points within a prescribed distance from an edge typically have low, poor-quality cross-correlation coefficients due to limited data along the image periphery. Thus, in the final iteration these points are discarded.

3.3 q-factor based reference configuration updating

A balance of error sources exists between incremental and cumulative mode steps. Incremental steps contain less decorrelation error than cumulative image comparisons beyond image $n + 1$, but random errors are summed and may quickly grow. To minimize this effect, a hybridized incremental-cumulative technique was implemented for updating the reference image during a time-lapse experiment, as outlined in Fig. 3 in the *q-factor based reference updating* box. In this scheme the occurrence of extensive decorrelation was evaluated via the q-factor map of the final iteration of a given image pair. Three features of the q-factor map are important when considering overall decorrelation between an image pair. First, the total number of thresholded q-factors must not exceed a given percentage of the total displacement measurement points, typically set to 15%. Second, the largest simply-connected area multiplied by its eccentricity plus a small factor to prevent degeneracy must not exceed a specified area, typically 121 px. Third, and most importantly, the standard deviation of normalized q-factors, Gaussian distribution described in Section 3.2, must not exceed a predefined level, typically set to 0.13 px ± 0.01 px. These threshold numbers were empirically established by analyzing datasets of known displacement. The variability in width is to account for changes in sample size. If any of these conditions are exceeded, decorrelation is indicated. The reference image is updated to the image immediately prior to the current deformed configuration image, the location of the reference update is flagged, and the IDM is rerun with the new reference image. If adjacent images fail the q-factor check the pair is flagged again and the algorithm continues to the next image.

3.4 Incremental and hybrid displacement cumulation

DIC algorithms are usually run in either incremental or cumulative mode. However, while measuring large deformation in cumulative mode, significant decorrelation can occur between images in a pair (image 0 compared to image n) for large n, which leads to large displacement errors. To circumvent this issue, qDIC is executed in a hybrid incremental-cumulative mode and we explicitly utilize our q-factor metrics to inform reference image updates when significant decorrelation between an image pair occurs. Subsequently, the displacements from this hybrid incremental-cumulative mode are converted to cumulative displacement measures.

This displacement conversion is conducted as follows. Consider a time-lapse image series analyzed from image 0 to image N, where significant decorrelation is detected using q-factors when reconstructing the cumulative displacement between image 0 and image $m+1$. Consequently, image m is updated as the reference image, and the cumulative displacements are then computed between image m to image N. Up until image m the cumulative displacement (u_p^0 where $0 < p \leq m$) between image 0 and image p is computed at the grid points $\mathbf{x}_{grid_0}$ defined by the subset spacing in image 0. While between image m and image h, the cumulative displacement ($\mathbf{u}_q^m$ where $m < q \leq h$), between image m and image q, is computed at the grid points $\mathbf{x}_{grid_m}$ defined by subset spacing in image m. The original grid points $\mathbf{x}_{grid_0}$ in image 0 move to positions $\mathbf{x}_{grid_0} + \mathbf{u}_m^0$ in image m. The cumulative displacements $\mathbf{u}_q^m$ computed at $\mathbf{x}_{grid_m}$ in image m are interpolated using bi-cubic splines onto the original grid points in image m and summed with u_m^0 to compute the total cumulative displacement u_q^0. This step is similarly repeated for multiple reference image updates to compute the total cumulative displacement.

4 Validation of the qDIC algorithm

To assess the improvement in displacement measurement accuracy by employing both the q_{PCE} and q_{PIE} q-factor metrics, we generated synthetic image stacks with analytically imposed displacement fields. A four stage validation process was adopted where the performance, namely accuracy and precision, was first assessed for zero-displacement images with varying image distortion applied to both images in a pair. Second, the performance on a homogeneous displacement field was characterized. Third, we applied a known inhomogeneous displacement field, and fourth, the algorithm was executed on the SEM Challenge #14 dataset. Three minimum subset sizes were employed throughout the validation process.

4.1 Synthetic image generation

Synthetic images were constructed by seeding higher-intensity regions (i.e. speckles) into a dark background. Seeding locations were semi-randomly generated using the Poisson Disk sampling algorithm with a cut-off radius 0.5 px greater than the seeded speckle characteristic radius, typically 3 px. An integer number of seed locations were used such that the final fill factor of speckles was approximately 50%, typically 50,000-65,000 particles for a 2 MPx initial image.

Speckles were generated at high resolution, convolved with a point spread function (PSF), downsampled, and interpolated into the complete image. The original speckle intensity was defined by a top-hat function of radius r_0, given by

$$S(x_1, x_2) = \frac{1}{1 + \exp\left(-2\gamma\left[1 - x_1^2/r_0^2 - x_2^2/r_0^2\right]\right)} \tag{4.1}$$

which is parameterized by $\gamma = 1000$, the decay rate of the intensity. Image formation optics were idealized by a symmetric Gaussian approximation to the Bessel function of the PSF for a 40x microscope objective with green ($\lambda_0 = 532nm$) speckles,

$$PSF(x_1, x_2) = \exp\left(-\frac{x_1^2}{2s^2} - \frac{x_2^2}{2s^2}\right) \tag{4.2}$$

where $s = \frac{0.21L}{NA}$, with $L = \frac{\lambda_0 r}{0.5\times10^{-6}}$ and $NA = 0.7$ is the numerical aperture of the lens. Here r is the integer-valued radius of the speckle on the final pixel grid.

The speckle image is the convolution of the separable PSF and the intensity distribution of the speckle, thus,

$$\begin{aligned} B(x_1, x_2) &= PSF(x_1, x_2) * S(x_1, x_2) \\ &= \sum_{\xi_1=-2r}^{2r} \exp\left(-\frac{\xi_1^2}{2s^2}\right) \times \left[\sum_{\xi_2=-2r}^{2r} \exp\left(-\frac{\xi_2^2}{2s^2}\right) I\left(x_1 - \xi_1, x_2 - \xi_2\right)\right] \end{aligned} \tag{4.3}$$

gives the image of a single speckle on a grid of $4r + 1$ by $4r + 1$ pixels with the speckle at the center. After convolution, speckle images were downsampled to the final pixel grid via binning of intensities to mimic the light collection of an image sensor. For each seed point location in the final image the downsampled speckles were added using bicubic spline interpolation.

After all speckles were placed into the final image, noise was added. Two types of random noise were used to mimic noise present in typical experimental images. First, white Gaussian noise was added at a signal-to-noise ratio of 25 and a background black-level of approximately 2% to simulate random noise. Second, each pixel was resampled from a Poisson distribution to simulate shot noise during image acquisition. Any pixels above the saturation limit were then set to the limit, and the whole image was renormalized to 255 grey-levels (i.e., an 8-bit greyscale range). A 512x512 px^2 region in the center of the image was output as the final synthetic image.

4.2 Analytical displacement fields

To prescribe deformation fields in the synthetic images, the same image generation process was conducted with two additional steps. The locations of the seed points were changed according to the known, analytical deformation map, and the speckle images for each location were deformed according to the local, affine deformation. By simulating the motion field in this way large-deformation interpolation was avoided, reducing potential artifacts introduced due to the image warping process.

To alter bead locations, the deformation mapping function for the image is applied to each seed point. At seed point n the reference position X_i^n is updated to the deformed position x_i^n by adding the displacement $u_i^n(X_i^n)$ evaluated from the deformation mapping function, i.e.,

$$x_i^n = X_i^n + u_i^n(X_i^n), \tag{4.4}$$

which are the locations now to be seeded with speckle images. Speckles in the deformed configuration that moved farther than $2r$ pixels outside of the original image boundary were discarded. Speckles within this margin region were seeded, but the image was cropped to the original dimensions after seeding such that the image boundaries suffered no loss of speckle information.

Each speckle was deformed according to an affine approximation to the underlying displacement field before seeding into the deformed image. The analytical displacement field in a $2r$ px square centered at the seed point is densely sampled at ten times the pixel sampling frequency, and the local deformation gradient is determined via a least-squares plane fitting procedure (see Section 5.2). This deformation gradient is used to warp the high-resolution speckle image before convolution with the PSF and downsampling to the nominal post-binning size. The appropriately deformed speckle image for each seed point n is then added to the final image, as discussed in Section 4.1. Non-rigid speckles were thus simulated for large deformation without introducing interpolation artifacts. For all experiments, initial image sizes were chosen such that the final 512×512 px^2 region used as input to the qDIC algorithm was fully seeded with speckles throughout the deformation process.

4.3 Zero-displacement noise floor assessment with image distortion

To determine the noise floor as a function of speckle warping, and thus signal degradation, a series of zero-displacement image pairs at various levels of axial strain (schematically illustrated in Fig. 2)

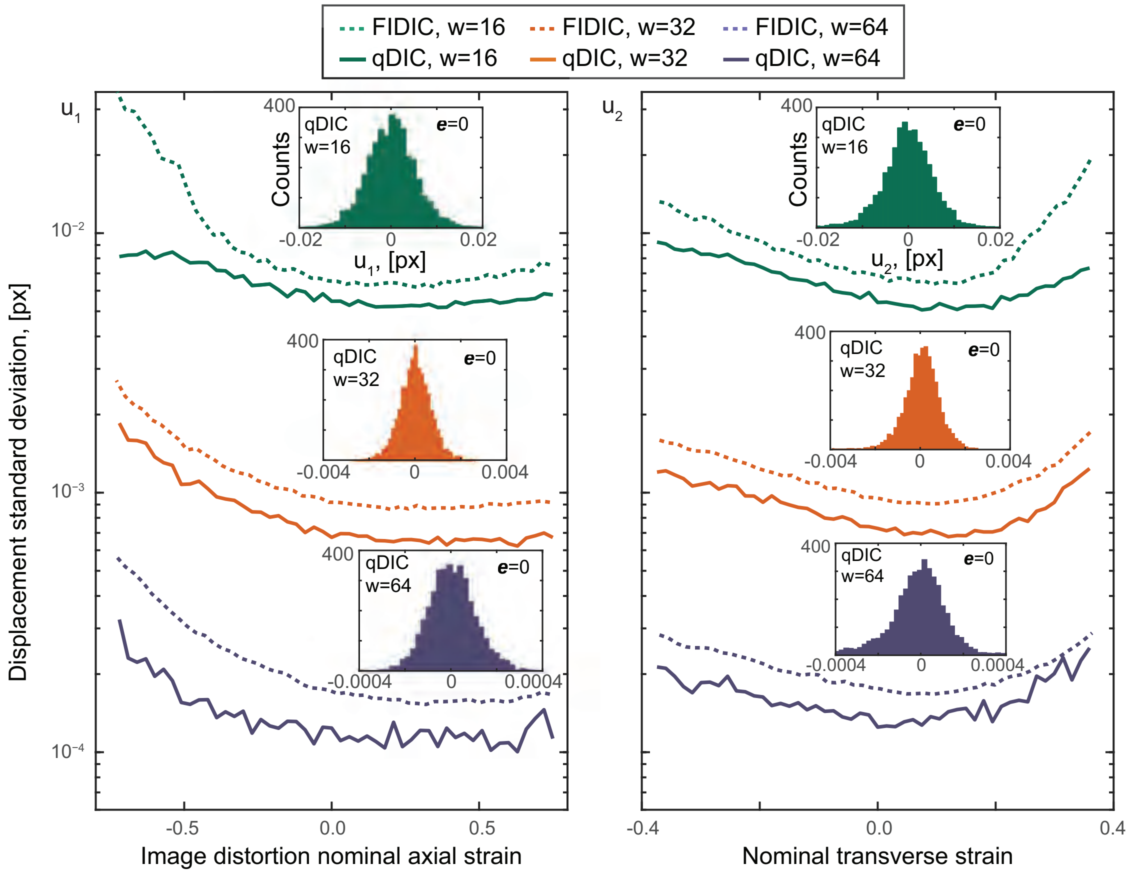

Figure 5: Standard deviation error from a rigid-body motion zero displacement field, plotted as a function of image distortion. Images in each pair contain unique synthetic noise and were analytically distorted via incompressible uniaxial compression or tension fields centered in the image in x_2 and the bottom edge of the image in x_1 to the given strain levels. The u_1 error is plotted as a function of the nominal axial image distortional strain, and u_2 error is plotted as a function of the transverse distortional strain for minimum subset sizes $w = 16, 32, 64$ px. The qDIC algorithm has lower error and is a flatter function of image distortion, indicating improved robustness to image noise and degenerating speckle quality. (*Insets*) Histograms of the recovered displacement for the distortion-free, zero-displacement cases for each qDIC minimum subset size (baseline)

was generated. In this synthetic dataset, each image contained unique Gaussian and Poisson noise but seed points were identical. Distorted images for pairs undergoing incompressible uniaxial compression and tension with prescribed nominal strains up to 75% in 1% increments were created to simulate the increasing degeneracy of the speckle pattern with increasing distortion (Fig. 5). This provides an assessment of the qDIC displacement measurement result between each image pair at given applied nominal axial strains. The mean and the standard deviation of the normally distributed displacement histogram yields a visual representation of the algorithm's accuracy and precision, respectively, in recovering the applied rigid body motion.

The noise level and matching error depend upon the amount of spatial averaging that the algorithm utilizes. Therefore, the minimum subset size, w, is a key factor in setting the noise floor, since smaller minimum subset sizes yield less spatial averaging, usually resulting in an increased noise floor, in the final displacement field. Three minimum subset sizes, $w = 16, 32, 64$ px, were utilized for the FIDIC and qDIC implementations presented here. Both algorithms include an error-minimizing iterative process and outlier removal. Since the qDIC algorithm extends outlier removal from the standard post-measurement fluctuation-based paradigm (Bar-Kochba et al., 2015) to include the newly introduced q-factors, the noise level is reduced. Both of these effects are present in the plot of standard deviation (1σ) of displacement versus the image distortional strains in Fig. 5. Representative displacement distributions for 0% distortion (baseline) are shown in histogram form for each subset minimum size in the three insets in Fig. 5. The characteristic distribution remains Gaussian-like, but the width dramatically decreases for larger subset sizes, due to the intrinsic smoothing operation of the larger correlation subset windows.

4.4 Homogeneous deformation reconstruction assessment

To assess the algorithm's performance in a more realistic deformation, an image dataset consisting of single images with a homogeneous deformation field was evaluated. The analytical field for this case was uniaxial compression to 75% nominal compressive strain. The center of the displacement field was located at the bottom center of the image, i.e., $x_1 = 0$, $x_2 = 255.5$ px. Transverse displacements were symmetric about the centerline of the image and u_1 increased linearly with x_1. Contours of these displacement fields are visualized in Fig. 6(b).

The mean displacement error is assessed by computing the mean squared pointwise displacement difference from the analytical field. This error measurement formulation is expressed as,

$$u_{err} = \frac{\sqrt{\sum_I \left(\mathbf{u}_{DIC} - \mathbf{u}_{analytical}\right)^2}}{N} \tag{4.5}$$

where $\sum_I$ indicates a sum across all measurement points in the image and N is the total number of measurement points. The plot of mean displacement error versus nominally applied axial strain is given in Fig. 6, comparing the performance for both the FIDIC and qDIC algorithms at minimum subset sizes of $w = 16, 32, 64$ px.

The plot in Fig. 6(a) shows that the error levels in both algorithms are comparable for displacement fields that are not highly distorted. The increased spatial averaging of larger minimum subset sizes tends to reduce error levels, which is expected for a homogeneous deformation field. At a critical strain (between 45% and 50% depending on the experimental details) the FIDIC algorithm accuracy, for smaller subset sizes, begins to decrease dramatically. Increases in error rate for both u_1 and u_2 occur at the same deformation step for FIDIC, but not qDIC, which benefits from the q-factor based hybrid incremental-cumulative switching scheme (Fig. 3).

4.5 Inhomogeneous deformation reconstruction accuracy

Since the most useful applications for DIC techniques involve the resolution of highly localized deformation fields, we evaluated the performance of our qDIC algorithm for an image set undergoing an inhomogeneous loading scenario. Here, we chose the well-characterized hole in an infinitely-thick plate problem featuring a hole of radius a under applied far-field compression. For this set of tests the hole was centered within each image. The linear elastic solution for the displacement

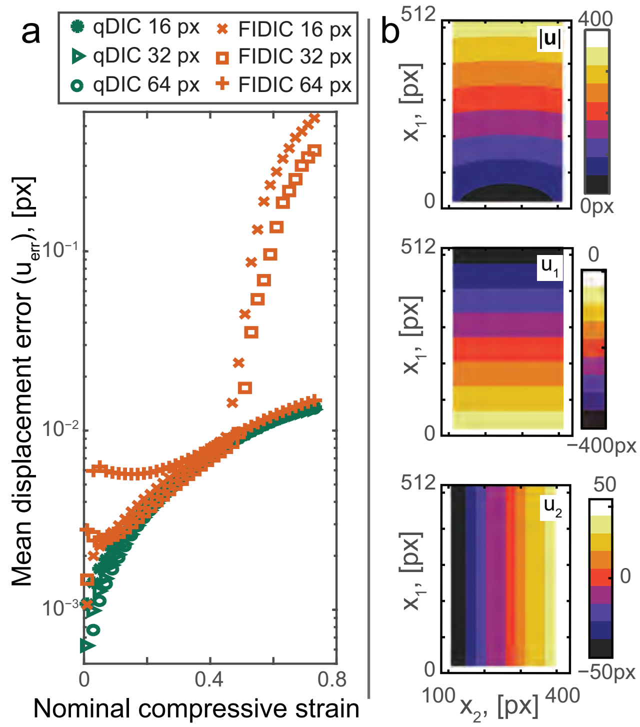

Figure 6: Mean displacement error determined from an analytically imposed homogeneous deformation field. (a) Mean displacement error as a function of applied strain. (b) Contour plots of the displacement magnitude, $|\mathbf{u}|$, u_1, and u_2 of the recovered deformation field via qDIC

fields is given by the Michell solution (Michell, 1899) under plane strain boundary conditions,

$$
\begin{aligned}
u_1(x_1, x_2) &= \frac{a\sigma_\infty}{8\mu}\left\{\frac{r}{a}(\kappa+1)\cos\theta + \frac{2a}{r}\left[(\kappa+1)\cos\theta + \cos 3\theta\right] - \frac{2a^3}{r^3}\cos 3\theta\right\}, \\
u_2(x_1, x_2) &= \frac{a\sigma_\infty}{8\mu}\left\{\frac{r}{a}(\kappa-3)\sin\theta + \frac{2a}{r}\left[(1-\kappa)\sin\theta + \sin 3\theta\right] - \frac{2a^3}{r^3}\sin 3\theta\right\},
\end{aligned}
\tag{4.6}
$$

where $\mu = \frac{E}{2(1+\nu)}$, $\kappa = \frac{3-\nu}{1+\nu}$, $r = \sqrt{x_1^2 + x_2^2}$, and $\theta = \arctan(x_2/x_1)$. The control variable to impose displacement is the far-field stress σ_∞, which is modulated such that strain steps are produced in approximately 1% increments. The two material properties, Young's modulus and Poisson's ratio, were taken as $E = 1$ MPa and $\nu = 0.3$ respectively. The hole radius was set to $a = 120$ px. The maximum axial compressive strain was restricted by the onset of the central hole closing. The linear elastic assumption no longer holds at these strain levels, however it suffices to provide well-defined analytical motion field for validation the reconstruction capability of the DIC algorithms.

The mean displacement error as a function of the applied far-field strain is given in Fig. 7(a), while Fig. 7(b) shows contours of the recovered displacement magnitude and displacement error between the analytically imposed and reconstructed displacement fields. As can be seen from Fig. 7(a) the error level as a function of minimum subset size behaves differently between the FIDIC and qDIC algorithms. For the qDIC algorithm the $w = 32$ px subset size balances spatial averaging and noise suppression, resulting in the lowest overall error. The higher inherent noise with FIDIC requires the additional smoothing of $w = 64$ px to reduce mean error, but is unable to

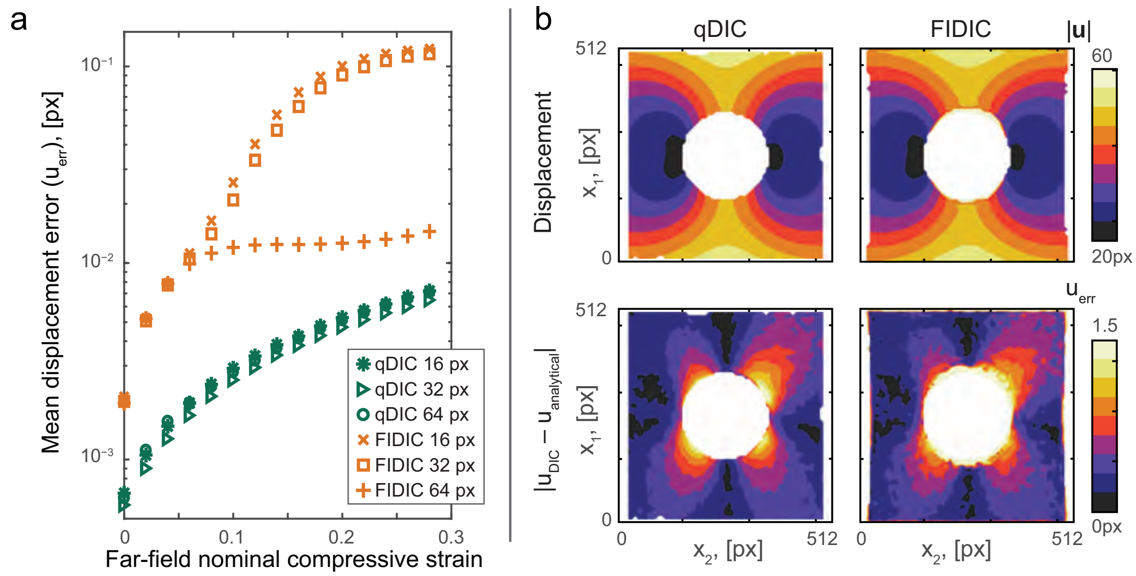

Figure 7: Assessment of qDIC performance under inhomogeneous loading. Note that the maximum far-field strain attainable is limited to approximately 30%, primarily to prevent full hole closure. (a) Comparison of the displacement error magnitude (see (4.5)) as a function of applied far-field strain at three minimum subset sizes for each algorithm. (b) Contour plots of the final displacement magnitude fields from both qDIC and FIDIC, and the absolute error from the analytical displacements. A minimum subset size w = 32 px was used for both algorithms in these plots

fully capture the higher spatial frequency displacement signal content of the u_1 field at that subset size.

The difference in reconstruction noise in the displacement signal is evident in the contour plots of Fig. 7(b), both of which are for a subset of w = 32 px. When examining both contour plots, it is visually apparent that qDIC outperforms FIDIC near boundaries where signal quality is lost due to incomplete information content in some subsets and in high-gradient regions where speckle distortions are greater. This is borne out by contours of displacement error magnitude, where large-gradient regions (i.e., tight banding in the displacement magnitude contours) tend to have comparatively large errors. Furthermore, the displacement errors in FIDIC are generally noisier.

4.6 SEM challenge #14

The Society for Experimental Mechanics provides several benchmark cases for evaluating DIC algorithm performance. The qDIC algorithm targets large displacement and high spatial frequency fields. Although not originally designed for large-deformations, the Sample #14 L5 test is a standard benchmark evaluating the reconstruction capability of DIC algorithms for varying spatial frequency signals. The image pair of Sample #14 L5 was analyzed via our qDIC algorithm, and the contour plot of the resultant displacement field is shown in Fig. 8(a). The mean and standard deviation of the resultant displacement field were taken in the x_1 direction for each pixel in x_2, and compared to the provided imposed displacement. Although optimized for large deformations this algorithm reconstructed the high-spatial frequency subpixel displacement field with overall pointwise absolute error of 5.4±4.4% (0.0054±0.0044 px) and root mean squared displacement

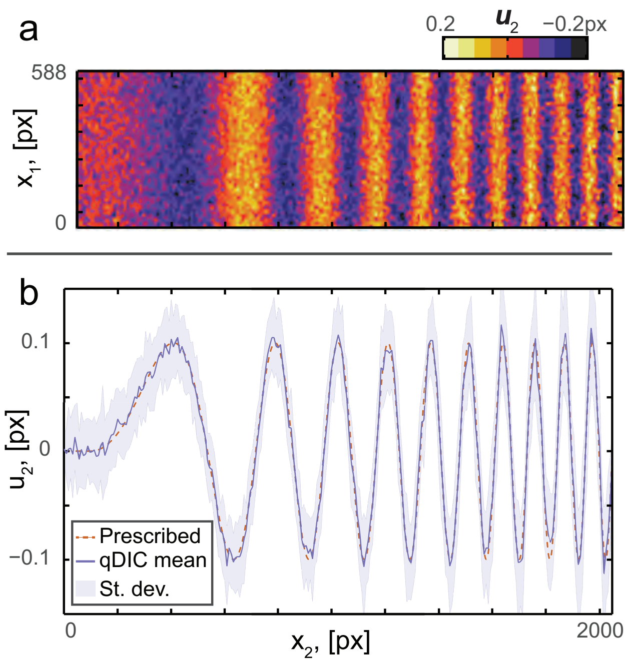

Figure 8: Contour and averaged displacement plots measured from the Society for Experimental Mechanics DIC Challenge Sample #14 L5 dataset. (a) Contour plot of measured u_2 displacement over the entire image area, using a minimum subset size $w = 16$ px and spacing $d = 8$ px. (b) Mean and one standard deviation (shaded region) of u_2 displacement averaged across the x_1 direction. The prescribed analytical displacement (dashed line) is shown for comparison

deviation $(\langle(u_{qDIC} - u_{analytical})^2\rangle)^{1/2} = 0.007$ px. At the highest spatial frequency in this sample, the qDIC algorithm continues to accurately track the displacement with minimal aliasing or amplitude attenuation due to the high spatial frequency reconstruction capacity of the IDM.

5 Experimental application of qDIC

As a real-world application of our new qDIC algorithm, an experimental test case consisting of uniaxial compression of an elastomeric foam to 65% nominal compressive strain was considered. In this experiment, a scientific camera and optical system was employed to image a face of the foam specimen that had been speckled. An image series was taken through the loading-unloading process, such that the entire deformation process was recorded.

5.1 Experimental setup

Load Frame Configuration: The load frame consisted of a custom benchtop system attached to a vibration isolated optical table. The loading apparatus was comprised, from top to bottom, as in Fig. 9(a), of a linear actuator (Ultra Motion, Cutchogue, NY; 0.6μm step resolution), load cell (LCFD-50, Omega Engineering, Stamford, CT), load alignment pivot, top and bottom platens, and two 90° opposed linear translation stages in an aluminum frame. Control and measurement was achieved via a data acquisition system (National Instruments, Austin, TX) operated through

LabView (National Instruments, Austin, TX). A schematic of the arrangement is shown in Fig. 9(a). Shear and bending loads on the specimen were minimized by the load alignment pivot consisting of a spherical indenter tip in contact with the flat top surface of the top platen. Platen thickness was chosen to minimize bending and ensure uniform contact pressure along the top surface of the sample to impose uniaxial compression. Top and bottom platens were machined from lubricious graphitic carbon steel and carefully lubricated to minimize frictional confinement (i.e., barreling). To this end, contact areas of the platens were dusted with $35\mu m$ spherical glass beads, such that rolling friction dominated the initial stages of compression. A layer of powered graphite lubricant minimized friction during subsequent compression.

Optical System Configuration: An optical system for single camera imaging of the specimen surface consisted of a camera with control computer, lens, polarizers, and lights was affixed to the optical table facing the load frame, see Fig. 9(b). The camera is a full-format 5.5 MPx greyscale sCMOS unit with 6.5μm pixel pitch (edge5.5, PCO-Tech Inc., Romulus, MI). A linearly polarized long-distance microscopy lens (K2/S, Infinity Photo-Optical Company, Boulder, CO) with 660 mm - ∞ focal distance and 1.8x magnification was used for image formation. The specimen surface was illuminated via a pair of high-intensity LED light panels (Lykos Daylight, Manfrotto, South Upper Saddle River, NJ) having a linear polarizing film (American Polarizers Inc., Reading, PA) attached at a 90° offset from the lens polarizer. The cross-polarization reduces glare and specular reflections from the load frame and specimen, improving image quality for DIC (LePage et al., 2016).

Specimen Preparation: The material used for this test case is a polyurathane-based 9 lb/ft^3 (void volume fraction approximately 80%) open-cell elastomeric foam that has been designed for impact protection (XRD, Rogers Corp., Rogers, CT). Specimens were excised from sheets of raw material via a vertical bandsaw and are approximately 13mm x 10mm x 10mm in size. One 13mm x 10mm face of the specimen is designated as the DIC face and prepared appropriately. A black background paint (Acrylic Ink!, Liquitex Artist Materials, Piscataway, NJ) with white speckling paint (High Flow, Golden Artist Colors Inc, New Berlin, NY) was used. Both paints are low-viscosity acrylic compounds and are applied using a gravity-feed dual-action airbrush (HP-C Plus, Iwata Medea Inc, Portland, OR) to create small, regularly sized, and high-contrast speckles. After speckling, the specimen cross-sectional area was measured, and the specimen was placed on the bottom platen, moved into the load frame such that the speckled face was at the focal plane of the lens, and the top platen set in place. Alignment under the compression device was an incremental process of applying small-to-moderate deformations while minimizing angular discrepancy between top and bottom platens. After alignment, the specimens were allowed to relax for approximately 1 hr prior to testing.

5.2 Experimental procedure

Once aligned a displacement controlled uniaxial compression experiment was conducted. A symmetric triangular displacement function peaking at 65% nominal compressive strain at a nominal strain-rate of $2 \times 10^{-4}\,\mathrm{s}^{-1}$ was utilized. Throughout the duration of the experiment, images were taken at 0.1 Hz and load data were acquired at 50 Hz. The image series was downsampled by a factor of three for computational tractability and input into the qDIC. A region of interest as show

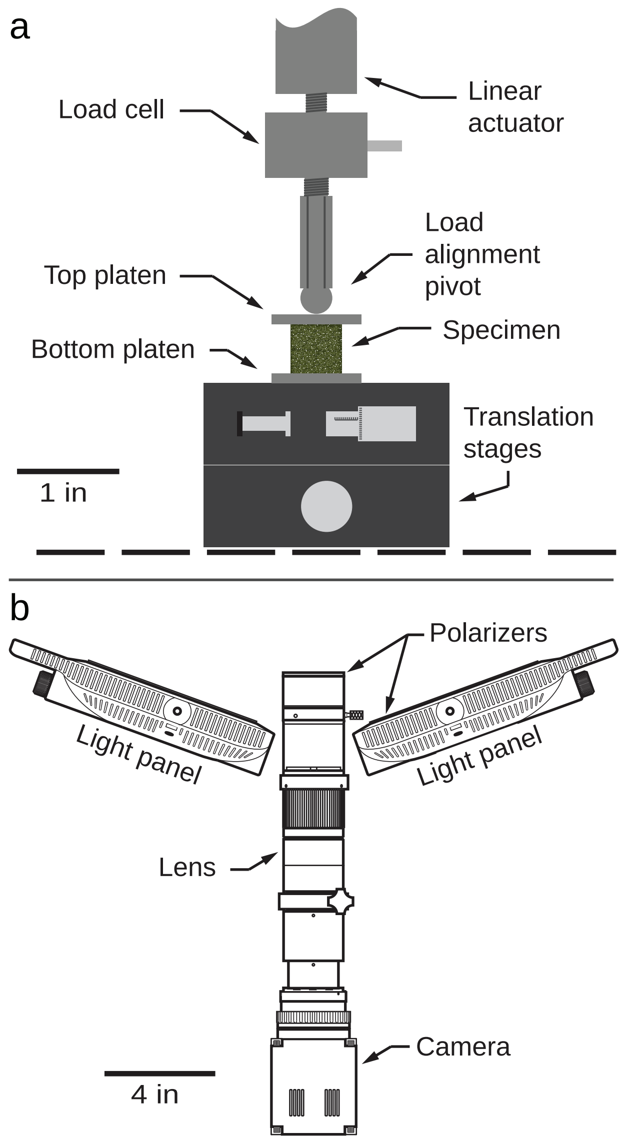

Figure 9: Schematic of the experimental uniaxial compression setup. (a) Front view of the compression device, showing the important components needed to deform the specimen, while minimizing shear and frictional forces and measuring the applied force. (b) Top view of the imaging platform used to collect experimental data for the qDIC algorithm. Light panels with linear polarization illuminated the specimen, while a long-distance microscope lens with perpendicular polarization formed images for the full-format scientific camera

in Fig. 10(a) was selected and the algorithm was run on 12 cores with 64Gb of memory on the Brown University Center for Computation and Visualization cluster. The qDIC settings were as given in Table 1. Homogenized spatial derivatives of displacement were taken by utilizing a global plane fitting procedure to the displacement field of a given displacement component, $i = 1, 2$. An example of such a displacement field pair is shown in Fig. 10(b). For a given displacement step, n, the coefficients of the best-fit plane p_{kl} determined by a robust bisquare linear least-squares fitting,

Specification	Details
Technique	Single Camera q-factor Based Digital Image Correlation
Camera noise	0.3 %
Pre-filtering	Gaussian, [3px,0.2]
Min. Subset Size	32 px
Min. Step Size	8 px
Correlation criterion	FFT-based ZNCC
Interpolation	Bicubic splines
Image size	513 x 1281 px^2
Measurement points	10465
Number of images	231 (0.1 Hz)
Pixel-to-mm conversion	1 px = 0.001 mm
Resolution: spatial	16 px = 0.016 mm
Resolution: noise	0.05 px, 0.00005 mm

Table 1: Digital image correlation specification details for the experimental test case

are computed such that,

$$u_i^n(x_j)_{plane} = p_{i0}^n + p_{ij}^n x_j, \tag{5.1}$$

where the summation convention is implied for $i, j = 1, 2$, and terms with zero subscripts are typical negligibly small rigid offsets. The deformation gradient is simply,

$$F_{ij} = p_{ij} + \delta_{ij}. \tag{5.2}$$

The polar decomposition of F_{ij} is $F_{ij} = R_{ik}U_{kj}$ where R_{ik} is the rotation tensor and U_{kj} is the right stretch tensor. The principal stretches are determined from the spectral decomposition of the right stretch tensor U_{kj}. Since the rotation tensor R_{ij} was determined experimentally to be close to identity (rotations are O(10^{-2}) smaller than stretches), $F_{ij} \approx U_{ij}$. In direct notation the spectral decomposition of $\mathbf{U}$ is then

$$\mathbf{U} = \lambda \mathbf{e}_1 \otimes \mathbf{e}_1 + \lambda_T \mathbf{e}_2 \otimes \mathbf{e}_2, \tag{5.3}$$

where λ is the stretch in the loading direction, λ_T is the stretch in the transverse direction, and $\mathbf{e}_1$ and $\mathbf{e}_2$ are the basis vectors of the measurement space (x_1, x_2), as given in Fig. 10. Under the conditions outlined above the nominal strain, as used in the validation cases, is simply $e = \lambda - 1$. The nominal uniaxial stress was computed by normalizing the measured force by the undeformed specimen cross-sectional area in the typical fashion. Image-based data and force data were temporally aligned by manually matching the onset of loading with the first observable deformation, and both engineering stress and stretch were resampled to 500 datapoints in the time domain using bi-cubic spline interpolation.

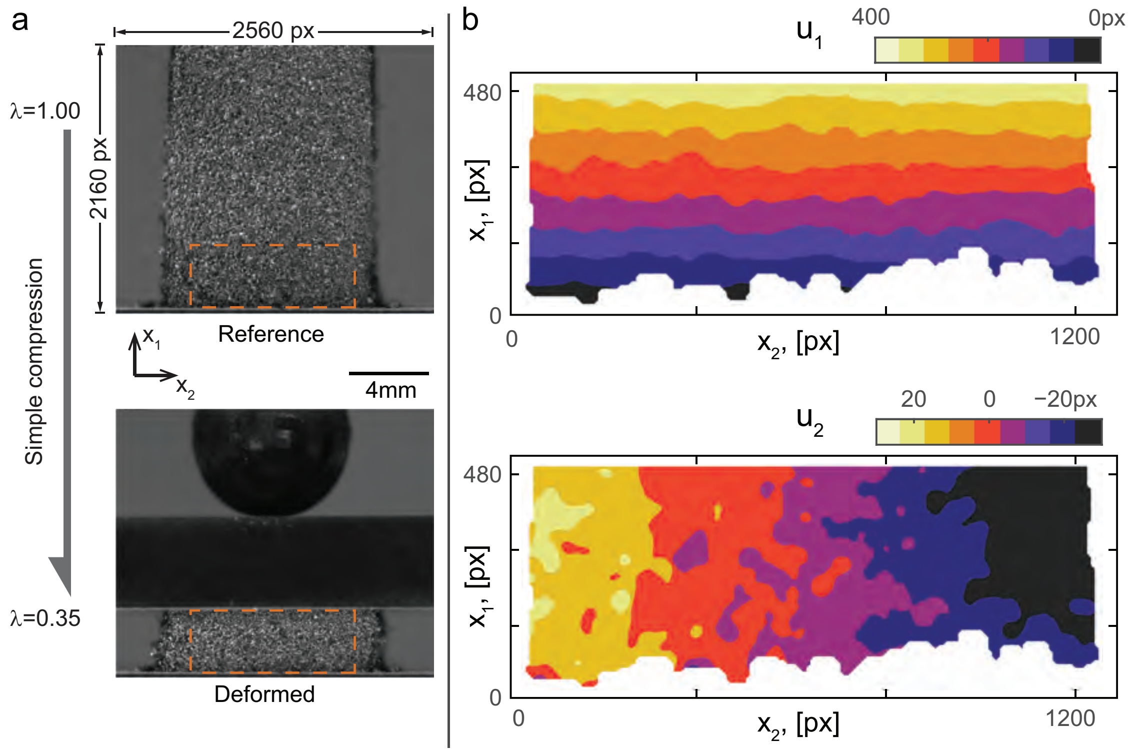

Figure 10: Experimental uniaxial compression images and contours of measured displacement fields. In this test case the foam undergoes large deformations and severe speckle distortions occur. The qDIC algorithm reconstructs up to about 400 pixels of displacement motion during the deformation process. (a) Example images from the experimental dataset showing the initial reference and fully deformed configuration. Note the relatively small Poisson effect and spherical load alignment pivot in the deformed image. The region of interest used to extract DIC images is denoted by the dashed box. (b) Contours of the qDIC measured displacement field for the fully-deformed configuration show flat uniform banding in u_1 indicating that little shear or displacement localization occurs. Banding is less distinct for u_2 since the signal level of the small lateral expansion is closer to the measurement noise floor

5.3 Experimental results

Initial diagnostic results from the qDIC on a zero-displacement noise assessment image pair are given in Table 1. The data listed show that the imaging system has relatively little shot noise. The spatial resolution is set by the choice of minimum subset size during the iterative refinement process; the minimum size of $w = 32$ is suitable to achieve the measurement goal while balancing spatial resolution and noise content in the images. Given this configuration, the noise-based displacement error indicates that the speckle pattern before deformation is sufficient for subpixel accuracy at a noise floor $O(10^{-2})$ px.

Displacement contours measured with qDIC from imaging results (e.g., Fig. 10(a)) for the fully-deformed configuration are shown in Fig. 10(b). For the axial u_1 displacement component case, the regular spacing of bands indicates a homogeneous displacement field with no compaction band formation or other localization observable on the surface of the specimen. The parallel and

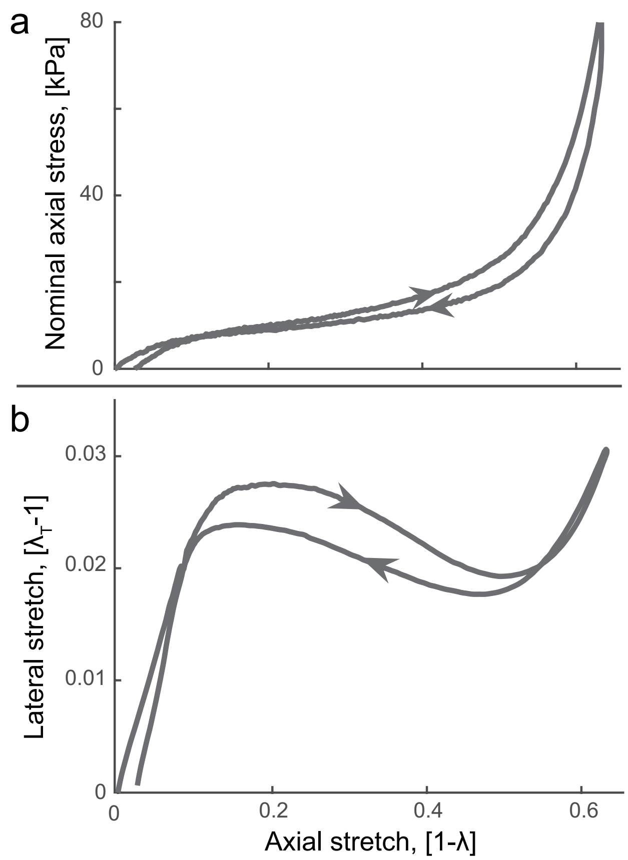

Figure 11: Experimentally measured nominal axial stress-stretch and transverse behavior of a polyurethane-based 9 lb/ft^3 open-cell elastomeric foam undergoing large deformation uniaxial compression. (a). The resultant engineering stress-stretch curve reconstructed from qDIC and force measurements at quasi-static $2 \times 10^{-4}\,\mathrm{s}^{-1}$ strain-rates. (b) The transverse engineering stretch $(\lambda_T - 1)$ computed from the qDIC displacement fields as a function of applied axial stretch $(1 - \lambda)$

horizontal nature demonstrates that shear, rotation, and bending are minimal. Despite the large deformation and associated measurement window size loss, qDIC tracks up to approximately 400 px of displacement. Resolving such large displacement, which has been extremely challenging with many previous DIC formulations, is a unique feature of the q-factor based hybrid incremental-cumulative qDIC computation scheme (Fig. 3). For transverse u_2 displacement, the banding is less well defined due to the high degree of compressibility, minimal transverse stretch, and significant speckle distortion (Fig. 10(a) resulting in a much lower signal-to-noise ratio in the u_2 displacements). The slight skewedness, curvature, and asymmetry visible particularly between x_2 = 1000 to 1200 px is due in large part to asymmetrical frictional confinement as a result of imperfections in the lubrication - an issue endemic to large deformation compression experiments.

Final stress-stretch and transverse-axial stretch curves are plotted in Fig. 11 for the complete load-unload cycle. In the stress-stretch plot of Fig. 11(a) the initial stiffening, plateau, and densification behavior typical of open cell foams is readily apparent. A small amount of hysteresis occurs, particularly at large levels of compression, which may be due to rate-dependant (i.e., polymer matrix viscoelasticity) or rate independent (e.g., frictional) effects. The apparent permanent set is a due to viscoelastic transients that do not completely decay during the imaging time-series. In the transverse versus axial stretch plot shown in Fig. 11(b) a similar characteristic pattern of increase-plateau-increase occurs, but at a much smaller amplitude. Note that although the plateau region appears to exhibit substantial auxeticity, this is in part a visual artifact. The decrease in transverse strain is less than $\sim 0.75\%$ over about 30% axial strain, i.e., a linearized Poisson-like ratio $\nu \approx -0.025$, during the plateau. The low noise floor of qDIC is needed in this challenging environment so that these small transverse strains remain measurable despite large axial deformation.

6 Experimental program for isotropic, elastomeric foams

In this section, we describe our process for experimentally testing the mechanical response of isotropic, elastomeric foams. We perform two classes of experiments: (1) homogeneous characterization experiments that are utilized to choose constitutive equations and estimate material parameters and (2) inhomogeneous validation experiments that are utilized to test constitutive model predictions. First, regarding characterization testing, we perform simple compression and simple tension experiments. All kinematic data in these experiments are obtained using full-field digital image correlation (DIC), which enables both axial and lateral strains to be obtained. Moreover, we are able to ensure that no unintended inhomogeneous deformation (e.g., specimen barreling or buckling, compaction banding, surface wrinkling, etc.) occurs during characterization experiments. Second, we perform a variety of inhomogeneous validation tests, namely, spherical and conical indentation, simple-shear-like deformation both without and with pre-compression, and tension of a specimen with circular holes, each of which are discussed further in Section 8. These validation experiments probe the predictive capability of the constitutive model in compression, shear, and tension-dominated situations.

6.1 Foam material

The experimental testing procedures and constitutive theory presented in this report are intended to be applicable to a large class of isotropic, open-cell elastomeric foams, provided that the material is capable of deforming homogeneously and does not exhibit localized deformation, such as compaction banding. In the present work, we consider three different relative densities of a single type of foam material. Our selection is a polyurethane-based open-cell elastomeric foam developed by Rogers Corporation (Poron XRD, Rogers, CT) for impact mitigation applications, which has been the subject of previous studies in the literature (Yang and Shim, 2004; Tang et al., 2017). The three relative densities considered, as specified by the manufacturer, are 144 kg/m^3, 192 kg/m^3, and 240 kg/m^3, which correspond to void volume fractions within the approximate range 0.75-0.95 and are hereafter referred to as the low, moderate, and high density foams, respectively. To get a sense of the foam microstructure, Fig. 12 shows (a) a macro-scale image, (b) a micro-scale image, and (c) a 3D volume render obtained via micro-computed tomography (μCT) for a representative sample of the moderate density foam. The pore structure is highly random, and based on optical microscopy measurements, the mean pore diameter is approximately 70 μm with a maximum pore diameter of up to about 500 μm for the moderate density foam.

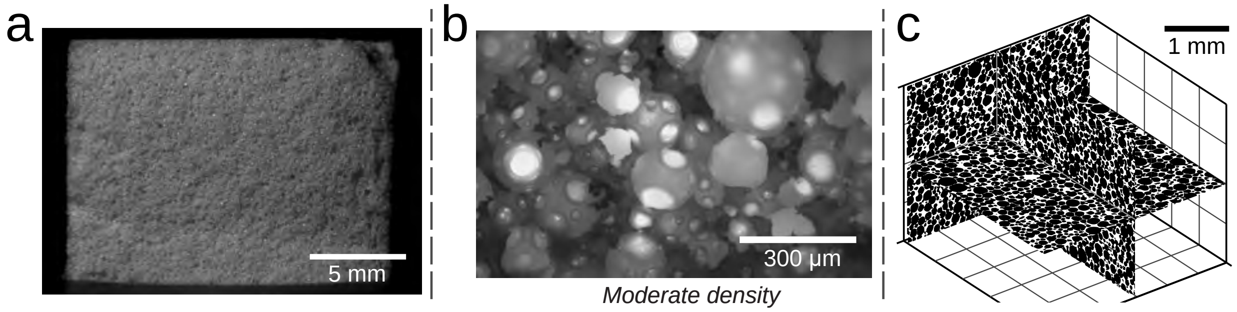

Figure 12: Three images of a representative moderate density foam sample at various scales. (a) The cut face of a foam cuboid. (b) Optical microscopy image of the microstructure of the surface of a cut face. (c) Micro-computed tomography 3D volumetric render of the foam microstructure (watershed-based binarization, in which black is void).

6.2 Specimen preparation

The details of specimen preparation depend on the specific type of test, but in general, specimens are collected from as-received approximately 12.9 mm-thick sheets of bulk material, speckled for digital image correlation, and then installed in appropriate fixtures. For compression testing, foam cuboids of approximately $10 \times 10 \times 12.9$ mm^3 are excised with a bandsaw. For tension testing, dogbone specimens are cut using a 75W CO_2 laser cutter (Universal Laser Systems Inc., Scottsdale, AZ) to the ASTM D3574 standard geometry for tensile testing of foam polymers. For indentation experiments (Section 8.1), $25.4 \times 25.4 \times 12.9$ mm^3 samples are laser cut and bonded to an aluminum backer on one of the large faces using a two-part epoxy (ITW Polymers Adhesives, Danvers, MA). For each simple-shear-like experiment (Section 8.2), two $30 \times 30 \times 12.9$ mm^3 specimens are laser cut, and each large, square face is epoxied to an aluminum backer. Finally, circular holes are cut out of tension specimens to be used for the third type of validation testing (Section 8.3). DIC measurements are used to obtain kinematic data in all experiments except for indentation testing, and to prepare specimens for DIC analysis, a face orthogonal to the testing axis is speckle-painted for each specimen. To speckle the specimens, a black base coat of acrylic ink (Liquitex Artist Materials, Piscataway, NJ) is airbrushed (HP-C Plus, Iwata Medea Inc, Portland, OR) on the surface, followed by a white speckle layer (Golden Artist Colors Inc., New Berlin, NY). For each configuration, the optical train employed is configured such that this technique yields speckles of approximately 3 to 7 pixels in size. Due to the inherent DIC challenges posed by mechanical testing of elastomeric foams – namely, that large speckle distortions and speckle loss due to cell collapse or opening arise when the material undergoes finite deformations – the custom, qDIC procedure described in the preceding sections is utilized, which incorporates the concept of cross-correlation quality factors to improve the accuracy of DIC measurements involving distorted speckle patterns undergoing large deformations. Finally, for all experiments, both characterization and validation, three specimens are tested, and each specimen is tested three times (i.e., nine total experiments per condition). For repeated experiments on the same specimen, we ensure that the wait-time between experiments is sufficiently long to allow complete relaxation of any time-dependent material physics, typically 3 hours or more in total test time.

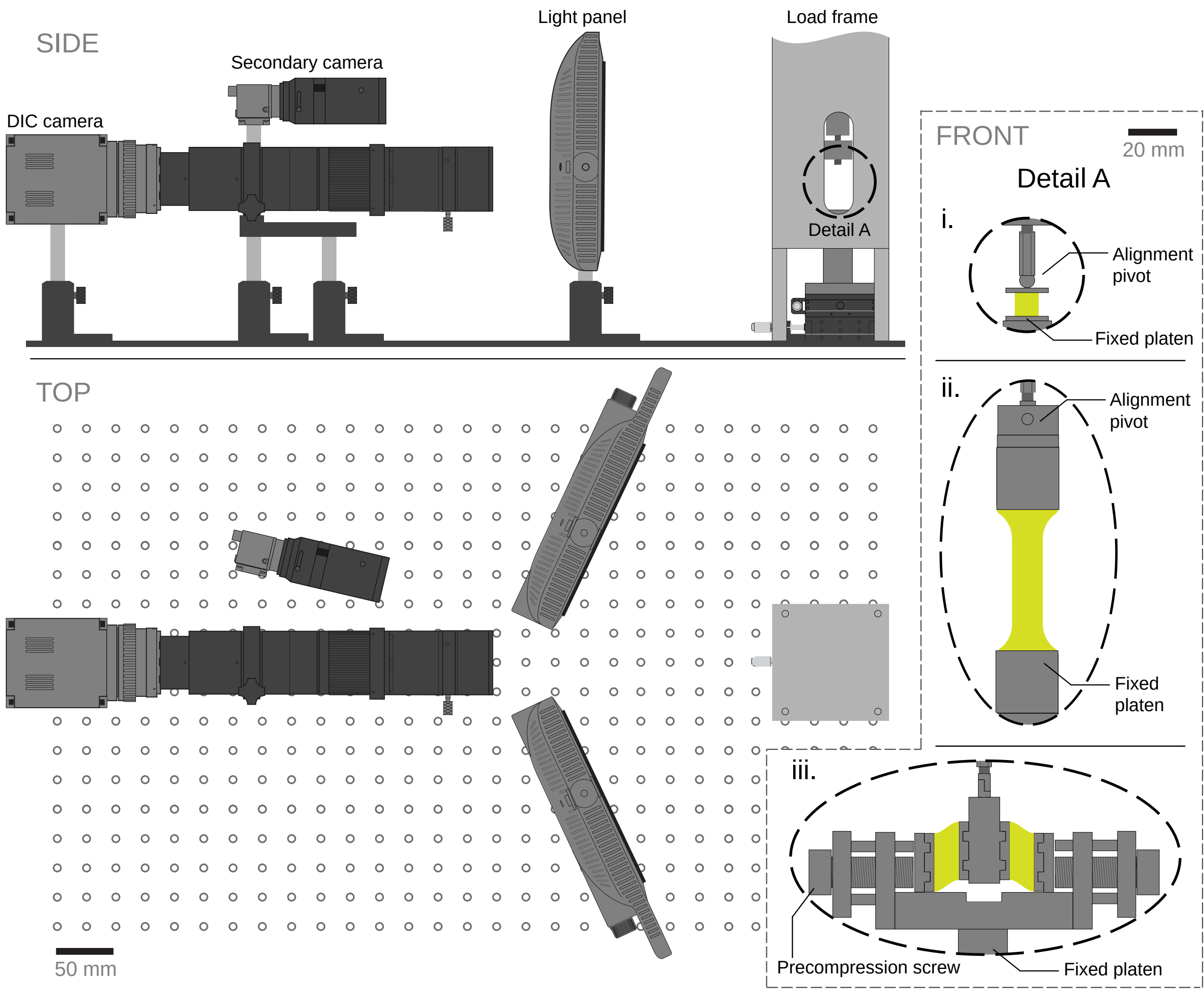

Figure 13: Schematic of the top and side views of the experimental setup as deployed on a vibration-isolated optical breadboard. The arrangement of the two cameras with lenses, light panels with linearly polarizing filters, and load frame is shown. Detail A gives front-view diagrams (i.e., as seen by the cameras) of the fixtures used for (i) simple compression, (ii) simple tension, and (iii) simple-shear-like deformation.

6.3 Experimental setup

A schematic layout of the optical system and loading apparatus used in our experiments is shown in Fig. 13. For all experiments, the loading apparatus and control software are the same as that described in Section 5.1 – namely, a screw-driven linear actuator (Ultra Motion, Cutchogue, NY) and a load cell (LCFD-50, Omega Engineering, Stamford, CT) with a custom LabView (National Instruments, Austin, TX) interface that allows synchronized actuator displacement control, actuator displacement measurement, imaging, and force data collection. The optical system utilized to collect data for two-dimensional DIC is comprised of a custom control computer, a scientific camera (edge5.5, PCO-Tech Inc., Romulus, MI), a long-distance microscopy lens (K2/S, Infinity Photo-Optical Company, Boulder, CO), polarizing filters (American Polarizers Inc., Reading, PA and Edmund Optics, Barrington, NJ), and LED light panels (Lykos Daylight, Manfrotto, South Upper Saddle River, NJ), which is assembled on the same vibration-isolated table as the loading apparatus. Additionally, for all experiments, a secondary imaging camera with a field-of-view encompassing the complete specimen and load frame is used to detect any potential anomalous loading conditions (e.g., onset of specimen failure at the grips).

For each experiment type, a custom load-frame insert is used to grip specimens during loading, and the three primary fixtures – simple compression, simple tension, and simple-shear-like deformation – are diagrammed in the insets of Fig. 13. By using modular inserts, the control procedures and DIC parameters remain consistent across experiment types. For simple compression, the insert consists of graphitic steel top and bottom platens compressed via a spherical indenter tip attached to the load cell. The spherical indenter tip acts as a pivot point, allowing any misalignment to be identified and eliminated in our compression experiments. The contact areas between the platens and the specimen are lubricated with graphite power and spherical glass microbeads (diameter 20-30 μm). For simple tension, screw-actuated wedge-and-pin-type grips – with the gripping-force screw acting as the pin – are attached to the base of the load frame and to the load cell. For the simple-shear-like validation experiments, a symmetric "double-shear" insert, involving two specimens with aluminum backers epoxied to both sides, is utilized, as shown in inset (iii) of Fig. 13. The center platen undergoes a vertical displacement prescribed by the linear actuator to shear the specimens. Additionally, horizontal screws on each side of the fixture may be adjusted to subject the specimens to a uniaxial pre-compression, which we set to be equal for both specimens in order to maintain symmetry, and which is held constant during the subsequent shear deformation.

6.4 Details of simple compression/tension tests

The characterization experiments, i.e., simple compression and tension, are conducted in displacement control to engineering strain limits of -0.75 (axial stretch of $\lambda = 0.25$) in compression and 0.5 (axial stretch of $\lambda = 1.5$) in tension and are loaded and unloaded at a constant, quasi-static engineering strain-rate magnitude of $2.0 \times 10^{-4}\ \mathrm{s}^{-1}$.[2] Illustrative example images of reference and deformed specimens for the high density foam are shown in Figs. 14(a) and (b) for compression and tension, respectively, where the direction of compression/tension is identified as the x_1-direction, and the selected regions-of-interest for DIC analysis are outlined with dashed lines. Contours of the resultant two-dimensional displacement fields – i.e., $u_1(x_1, x_2)$ and $u_2(x_1, x_2)$ – at sample levels of deformation, namely an axial stretch of $\lambda = 0.35$ for compression and $\lambda = 1.50$ for tension, calculated using the custom qDIC procedure are also shown in Fig. 14. In both examples, the contours reveal an axial displacement field u_1 that depends linearly on the axial referential coordinate x_1 and a lateral displacement field u_2 that depends linearly on the lateral referential coordinate x_2 – indicating that the intended homogeneous deformation without shearing and with minimal barreling has been achieved. Importantly, in our compression experiments, we do not observe evidence of strain localization into compaction bands, such as those that often arise during compression of very-low-density, "reticulated" foams (e.g., Lakes et al., 1993; Wang et al., 2000; Elliott et al., 2002). This is quantified via the histogram-based technique of Wang and Cuitiño (2002) (see Appendix A). Furthermore, at the spatial resolution of the DIC algorithm using a subset

[2]The choice of quasi-static strain-rate was informed by preliminary stress relaxation experiments on the moderate density foam.

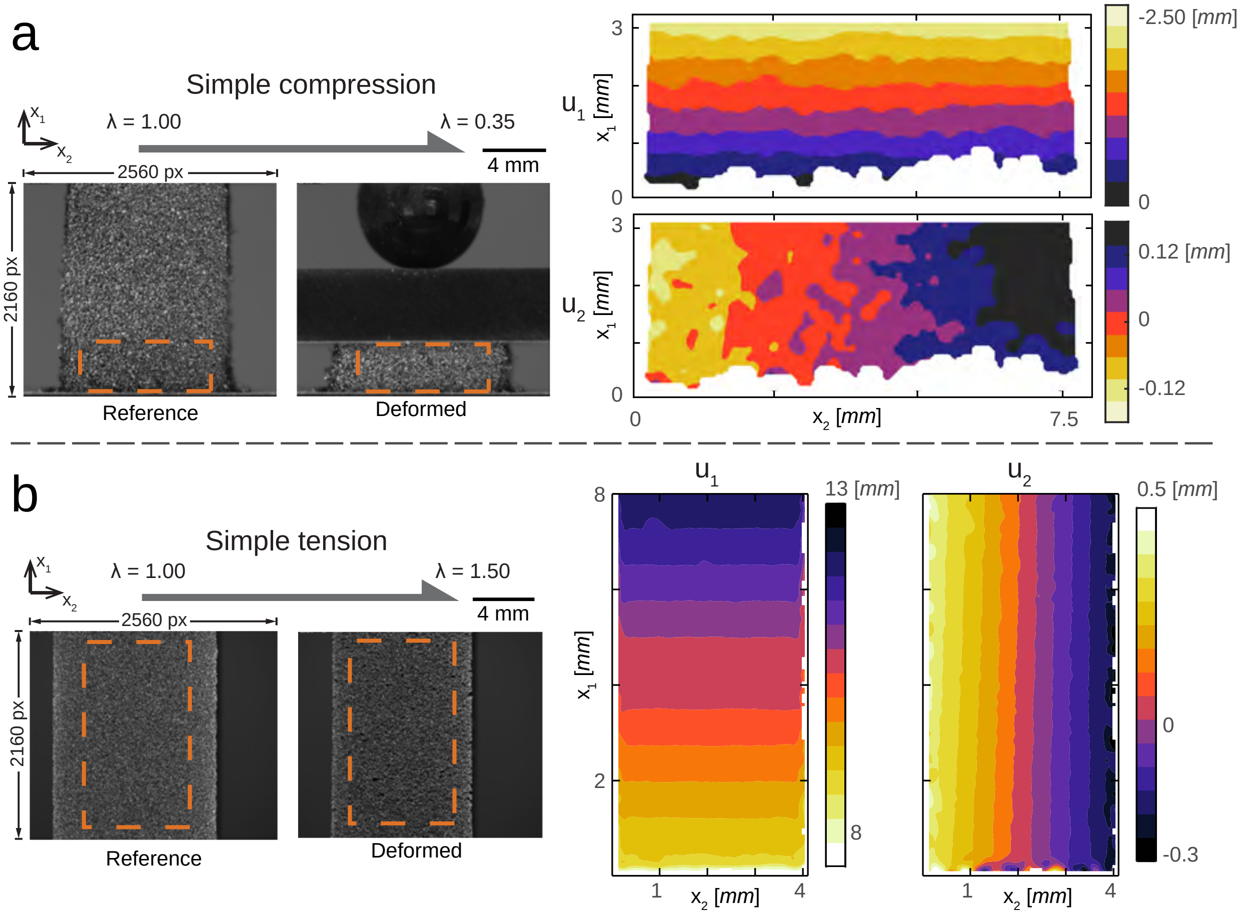

Figure 14: Example kinematic data collected from (a) simple compression (adapted from Fig. 10) and (b) simple tension experiments on the high density foam. (Left) Images of the respective specimens in the reference and deformed states with the regions-of-interest for DIC analysis outlined with dashed lines. DIC regions are approximately 1200×350 px^2 for compression and approximately 800×1900 px^2 for tension. (Right) Contours of the DIC-calculated, two-dimensional displacement fields for the axial (u_1) and lateral (u_2) displacement components.

size of 16×16 px^2 (see Appendix A), inhomogeneities in the displacement field are an order of magnitude smaller than displacement due to the globally applied deformation and of similar scale as the displacement noise floor.

Components of the global displacement gradient tensor are extracted from the displacement fields for each deformation step in each experiment via a global plane-fitting procedure, which is described in detail in Section 5.2, and the components du_1/dx_1 and du_2/dx_2 are identified as the axial engineering strain and lateral engineering strain, respectively. The corresponding axial engineering stress is computed from load-cell data and the previously-measured, referential cross-sectional area. A summary of the experimental data-flow used to reduce experimental data to axial engineering strain, lateral engineering strain, and axial engineering stress data is outlined in Fig. 15. The axial engineering stress versus axial engineering strain and lateral engineering strain versus axial engineering strain data are plotted as solid lines in Fig. 1 for the (a) low, (b) moderate, and (c) high density foams. The black curves represent the average of the nine instances of each experiment,

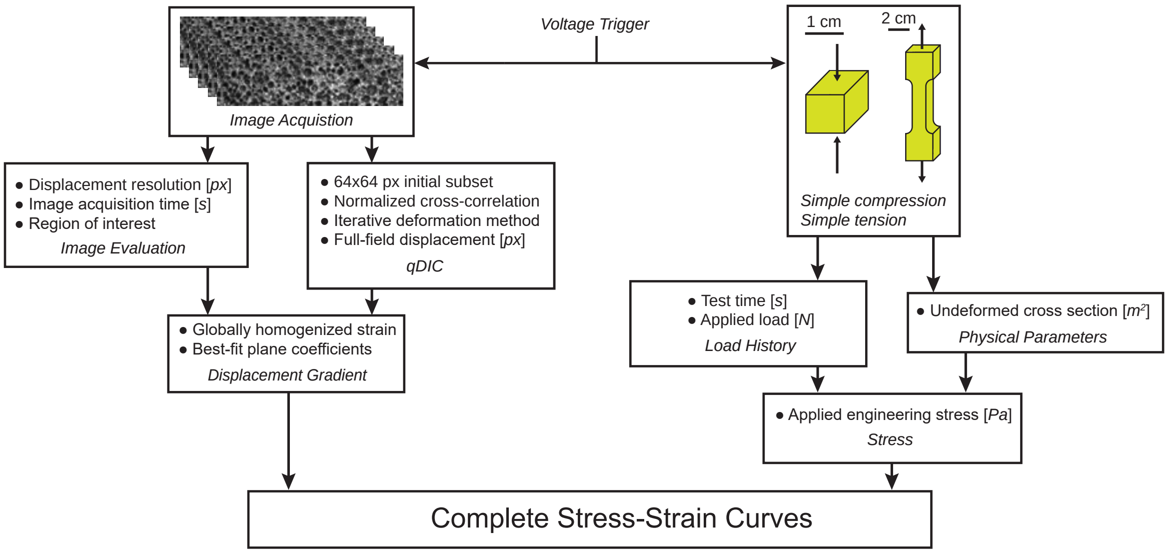

Figure 15: Outline of the experimental data-flow for quality-factor-based digital image correlation (qDIC) data, which is reduced to axial and lateral engineering strain data, and force data, which is used to compute the axial engineering stress. Experiments are initiated via a voltage signal provided when the imposed displacement history is begun, ensuring that time-synchronized load and images datasets are collected.

and the shaded areas surrounding the solid curves represent one standard deviation above and below the average, which indicate good repeatability in our experiments. Arrows indicate loading and unloading, demonstrating that hysteresis is minimal in our experiments and that the strain-rate is sufficiently low so that the experimentally-measured behavior represents the equilibrium, elastic response of the material. Finally, we note that characterization of the foam material in simple compression along each of the three orthogonal directions of the as-received sheets revealed no discernible difference in the experimentally-measured behavior. This observation, along with the random microstructure of the foam material (Fig. 12), supports our choice to model the foam material as isotropic.

7 Hyperelastic constitutive theory

In this section, we describe our hyperelastic constitutive model for the elastic behavior of isotropic, elastomeric foams and apply the model to three densities of Poron XRD foam.

7.1 Basic kinematics

We consider a body B identified with the region of space it occupies in a fixed reference configuration and denote an arbitrary material point within B as $\mathbf{x}$. The referential body B then undergoes a motion $\mathbf{y} = \chi(\mathbf{x}, t)$ to the deformed body $\mathcal{B}_t$ at each time t. The deformation gradient is given by $\mathbf{F} = \nabla\chi$, such that the ratio of referential to deformed volume is strictly greater than zero, i.e., $J = \det \mathbf{F} > 0$.[3] The displacement field is denoted as $\mathbf{u}(\mathbf{x}, t) = \chi(\mathbf{x}, t) - \mathbf{x}$, and the left and right Cauchy-Green deformation tensors are $\mathbf{B} = \mathbf{F}\mathbf{F}^\top$ and $\mathbf{C} = \mathbf{F}^\top\mathbf{F}$, respectively. The deformation tensors admit the spectral decompositions $\mathbf{B} = \sum_{i=1}^{3} \lambda_i^2 \mathbf{l}_i \otimes \mathbf{l}_i$ and $\mathbf{C} = \sum_{i=1}^{3} \lambda_i^2 \mathbf{r}_i \otimes \mathbf{r}_i$, where $\{\lambda_i | i = 1, 2, 3\}$ are the principal stretches, $\{\mathbf{l}_i | i = 1, 2, 3\}$ are the principal directions of $\mathbf{B}$, and $\{\mathbf{r}_i | i = 1, 2, 3\}$ are the principal directions of $\mathbf{C}$. Finally, we introduce the logarithmic (Hencky) finite-strain tensor in the deformed body: $\mathbf{E} = \sum_{i=1}^{3} (\ln \lambda_i) \mathbf{l}_i \otimes \mathbf{l}_i$.

7.2 An isotropic free-energy function

The constitutive response of a hyperelastic material is specified through the free-energy density function ψ. In general, ψ is a function of the right Cauchy-Green tensor $\mathbf{C}$, i.e., $\psi = \hat{\psi}(\mathbf{C})$, but for an isotropic material, the free-energy function is an isotropic function of $\mathbf{C}$ and may be represented as a function of the principal stretches or three independent invariants. Stretch-based, Ogden-type free-energy functions of the form $\psi = \check{\psi}(\lambda_1, \lambda_2, \lambda_3)$ are commonly used to model both incompressible (Ogden, 1972b) and compressible (Ogden, 1972a; Storakers, 1986) elastomers; however, as mentioned in Section 1, this approach can be unwieldy to work with for highly-compressible materials. Alternatively, invariant-based free-energy functions utilizing the principal invariants of $\mathbf{C}$, i.e., $I_1 = \operatorname{tr} \mathbf{C}$, $I_2 = (1/2)((\operatorname{tr} \mathbf{C})^2 - \operatorname{tr}(\mathbf{C}^2))$, $I_3 = \det \mathbf{C} = J^2$, may be invoked, and indeed, several hyperelastic models for porous elastomers fall in this category (e.g., Blatz and Ko, 1962; Yang and Shim, 2004; Danielsson et al., 2004; Anani and Alizadeh, 2011; Shrimali et al., 2019). However, developing free-energy functions of the form $\psi = \breve{\psi}(I_1, I_2, I_3)$ that depend on all three invariants, which is necessary to capture experimental data for compressible foams, is difficult, since it is not straightforward to isolate the effect of each invariant.[4] To address this challenge, we develop a free-energy function that depends on invariants of the logarithmic strain tensor $\mathbf{E}$, as proposed by Criscione et al. (2000). The logarithmic-strain invariants of Criscione et al. (2000), which we denote as $\{K_1, K_2, K_3\}$, represent specific aspects of deformation, enabling a more tractable path to introducing phenomenological fitting functions that capture experimental data. The three invariants are defined as follows:

1. The first invariant is $K_1 = \operatorname{tr}(\mathbf{E}) = \ln(J) = \ln(\lambda_1 \lambda_2 \lambda_3)$ and represents the volume change of the material with positive values for dilatation and negative values for compaction.

2. The second invariant is $K_2 = |\operatorname{dev}(\mathbf{E})| \geq 0$ and represents the magnitude of constant-volume distortion in the material. In terms of the principal stretches, the second invariant is given by $K_2 = \sqrt{(\ln \lambda_1 - (1/3)K_1)^2 + (\ln \lambda_2 - (1/3)K_1)^2 + (\ln \lambda_3 - (1/3)K_1)^2}$. Defining the tensorial direction of deviatoric strain as $\mathbf{N} = \operatorname{dev}(\mathbf{E})/K_2$, such that $\mathbf{N}$ is a deviatoric and unit-magnitude tensor, the logarithmic strain may be expressed as $\mathbf{E} = \frac{1}{3}K_1 \mathbf{1} + K_2 \mathbf{N}$.

[3] *Notation:* The symbols ∇, Div and Curl denote the gradient, divergence, and curl with respect to the material point $\mathbf{x}$ in the reference body B; grad, div, and curl denote these operators with respect to the point $\mathbf{y} = \chi(\mathbf{x}, t)$ in the deformed body $\mathcal{B}_t$. We write $\operatorname{tr} \mathbf{A}$, $\det \mathbf{A}$, and $\operatorname{dev} \mathbf{A}$ to denote the trace, determinant, and deviatoric part of a tensor $\mathbf{A}$, respectively.

[4] See, for example, Criscione (2004) for a discussion of this issue in the context of invariant-based free-energy functions for incompressible materials.

3. The third invariant is $K_3 = 3\sqrt{6}\det(\mathbf{N})$ and represents the mode of distortion. The pre-factor $3\sqrt{6}$ is present so that $-1 \leq K_3 \leq 1$. The third invariant is constant for a given distortion mode (e.g., $K_3 = -1$ in simple compression, $K_3 = 0$ in simple shear, and $K_3 = 1$ in simple tension) and hence, K_3 remains fixed during the simple compression/tension experiments utilized for material characterization. In terms of the principal stretches, the third invariant may be expressed as $K_3 = 3\sqrt{6}(\ln\lambda_1 - (1/3)K_1)(\ln\lambda_2 - (1/3)K_1)(\ln\lambda_3 - (1/3)K_1)/K_2^3$.

As shown by Criscione et al. (2000), the Cauchy stress is then given through the derivatives of the free-energy function $\psi = \tilde{\psi}(K_1, K_2, K_3)$ by

$$\mathbf{T} = J^{-1}\left[\frac{\partial\tilde{\psi}}{\partial K_1}\mathbf{1} + \frac{\partial\tilde{\psi}}{\partial K_2}\mathbf{N} + \frac{\partial\tilde{\psi}}{\partial K_3}\frac{1}{K_2}\mathbf{Y}\right] \tag{7.1}$$

where $\mathbf{Y} = 3\sqrt{6}\mathbf{N}^2 - \sqrt{6}\mathbf{1} - 3K_3\mathbf{N}$.[5]

7.3 Decomposition of the free-energy function

We take the free-energy density function $\tilde{\psi}(K_1, K_2, K_3)$ to be additively decomposed as follows:

$$\tilde{\psi}(K_1, K_2, K_3) = G_0\left[X(K_1)K_2^2 + L(K_2, K_3)\right] + Bf(K_1), \tag{7.2}$$

where G_0 and B are the ground-state shear and bulk moduli, respectively, and $X(K_1)$, $L(K_2, K_3)$, and $f(K_1)$ are phenomenological fitting functions. The interpretation of each term is as follows:

1. For a material undergoing large volumetric deformation, interaction between the volumetric and distortional contributions to the free energy is expected. The $G_0X(K_1)K_2^2$ term characterizes this coupling between the volumetric and distortional responses. For simplicity, we assume that this term only involves low-order K_2-dependence, i.e., that it only depends on K_2 through K_2^2, and is independent of the third invariant K_3. The volumetric dependence of this term may be more general through the function $X(K_1)$. More complex forms of volumetric/distortional coupling may certainly be invoked, but we find that this simple form is capable of capturing experimental data while enabling a streamlined material parameter estimation procedure – discussed further in Appendix B. The function $X(K_1)$ may be interpreted as encompassing the volumetric-strain-dependence of the instantaneous shear modulus. We require that $X(K_1 = 0) = 1$, and for the purpose of stability – discussed further in Section 9 – we also require that the function $X(K_1)$ remain positive over the intended K_1-range of application.

2. The $G_0L(K_2, K_3)$ term represents the higher-order distortional response, i.e., higher-order than the K_2^2-dependence of the first term, which we take to be uncoupled from the volumetric response for simplicity. This term is intended to capture stiffening behavior as the magnitude of distortion, K_2, increases, and the inclusion of K_3-dependence allows for mode-dependence

[5] Equation (7.1) may be obtained by recognizing that for an isotropic, hyperelastic material, the Kirchhoff stress $\mathbf{T}_K = J\mathbf{T}$ is given through the derivative of the free-energy function with respect to the spatial logarithmic strain tensor – i.e., $\mathbf{T}_K = \partial\tilde{\psi}/\partial\mathbf{E}$ – and then utilizing the chain rule along with the identities $\partial K_1/\partial\mathbf{E} = \mathbf{1}$, $\partial K_2/\partial\mathbf{E} = \mathbf{N}$, and $\partial K_3/\partial\mathbf{E} = \mathbf{Y}/K_2$.

of the higher-order distortional response. We require that $L(K_2 = 0, K_3) = \partial L/\partial K_2|_{K_2=0} = 0$, and that, following Criscione et al. (2000), $\partial L/\partial K_3$ goes to zero as order K_2^3 or higher as K_2 goes to zero. Moreover, we require that $\partial L/\partial K_2 > 0$ for all $K_2 > 0$ and $-1 \leq K_3 \leq 1$, so that the function $L(K_2, K_3)$ increases monotonically with K_2.

3. Finally, $Bf(K_1)$ describes the purely volumetric response. We require that $f(K_1 = 0) = 0$ and $df/dK_1|_{K_1=0} = 0$. Furthermore, for the purpose of stability, we require that $d^2f/dK_1^2 > 0$ for all K_1, i.e., that df/dK_1 is a monotonically increasing function of K_1.

Using (7.2) in (7.1), we obtain the following expression for the Cauchy stress:

$$\mathbf{T} = J^{-1}\left[\left(G_0\frac{dX}{dK_1}K_2^2 + B\frac{df}{dK_1}\right)\mathbf{1} + G_0\left(2X(K_1)K_2 + \frac{\partial L}{\partial K_2}\right)\mathbf{N} + G_0\frac{\partial L}{\partial K_3}\frac{1}{K_2}\mathbf{Y}\right]. \tag{7.3}$$

Note that the first term in (7.3), namely, the term involving $G_0(dX/dK_1)K_2^2\mathbf{1}$, represents a shear-induced mean stress that arises due to the coupled volumetric/distortional response.

7.4 Specialization of the free-energy function

To fit to the experimental data collected in Section 6 for low, moderate, and high density Poron XRD, we choose specific forms for the phenomenological functions appearing in (7.2). We emphasize that, while these forms are intended to capture data for Poron XRD, future modification may be necessary to apply the modeling approach to other foam materials.

1. Based on experimental data, we find that a form for the function $X(K_1)$ that linearly depends on K_1 but with different slopes before and after the onset of the plateau regime in compression is sufficient to capture the response. Accordingly, we adopt the following simple phenomenological form for dX/dK_1:

$$\frac{dX}{dK_1} = \frac{1}{2}\left(X_1' + X_2'\right) + \frac{1}{2}\left(X_1' - X_2'\right)\tanh\left[\frac{1}{\Delta_\mathrm{K}}(K_1 - K_1^0)\right], \tag{7.4}$$

where $K_1^0 < 0$ is the value of K_1 denoting the transition to the plateau regime, $\Delta_\mathrm{K} > 0$ is a parameter denoting the K_1-range across which the assumed hyperbolic-tangent-type transition in the value of dX/dK_1 transitions from X_1' prior to the plateau regime in compression (i.e., $K_1 \gtrsim K_1^0$) to X_2' after the onset of the plateau regime in compression (i.e., $K_1 \lesssim K_1^0$). To capture experimental data, the value of X_2' is small compared to X_1'. Integrating (7.4) with respect to K_1 and applying the condition $X(K_1 = 0) = 1$, we obtain the following phenomenological form for $X(K_1)$:

$$X(K_1) = \frac{1}{2}\left(X_1' + X_2'\right)K_1 + \frac{\Delta_\mathrm{K}}{2}\left(X_1' - X_2'\right)\ln\left[\frac{\cosh\left((K_1 - K_1^0)/\Delta_\mathrm{K}\right)}{\cosh\left(K_1^0/\Delta_\mathrm{K}\right)}\right] + 1. \tag{7.5}$$

2. The higher-order distortional response is taken to be given through

$$L(K_2, K_3) = C_0K_2^p + C_1\left(1 + K_3\right)K_2^q, \tag{7.6}$$

where $C_0 > 0$ and $C_1 > 0$ are constant parameters and $p > 2$ and $q > 2$ are higher-order exponents. We note that since $K_3 = -1$ in compression, the second term does not affect the response in compression. This term is present to allow for different higher-order responses in compression and tension to be specified.

3. Finally, the purely volumetric response function is fitted to

$$\frac{df}{dK_1} = \frac{J^{C_2} - 1}{C_2} + C_3 J \left[J^{-r} - \left(\frac{1 - J_{\min}}{J - J_{\min}} \right)^r \right], \tag{7.7}$$

where $J = \exp(K_1)$ is the volume ratio and $J_{\min}$, r, C_2, and C_3 are constant parameters. We note that the parameter $J_{\min}$ represents the minimum allowable value of J and that df/dK_1 diverges as J approaches $J_{\min}$ from above. The parameter $J_{\min}$ is limited to be within the range $0 < J_{\min} < 1$ and may be interpreted as $J_{\min} = 1 - \phi_0$, where ϕ_0 is the void volume fraction of the undeformed foam. The first term in (7.7) is intended to capture the response in tension and prior to the plateau regime in compression, while the second term is intended to capture the rapidly stiffening behavior in compression. We note that $d^2 f/dK_1^2|_{K_1=0}$ does not precisely equal one. However, since the first term is intended to capture the response prior to the onset of the plateau regime, its contribution will dominate the second derivative at $K_1 = 0$, so that $d^2 f/dK_1^2|_{K_1=0} \approx 1$, and B approximately represents the ground-state bulk modulus.[6] Upon integrating (7.7) with respect to K_1 (for $r \neq 1$) and applying the condition $f(K_1 = 0) = 0$, we obtain the following functional form for f:

$$f = \frac{J^{C_2} - C_2 \ln J - 1}{C_2^2} + \frac{C_3}{r-1} \left[\frac{-1}{J^{r-1}} + \frac{(1 - J_{\min})^r}{(J - J_{\min})^{r-1}} + J_{\min} \right]. \tag{7.8}$$

7.5 Material parameters for Poron XRD

We estimate the material parameters appearing in our constitutive model – a total of fourteen parameters – for Poron XRD from the simple compression/tension data in Fig. 1. For ease of presentation, the discussion of our heuristic procedure for material parameter estimation is relegated to Appendix B. The material parameters for all three densities of Poron XRD determined using this procedure are listed in Table 2. Four of the material parameters are density-dependent – G_0, B, $J_{\min}$, and C_1 – and the remaining ten parameters are density-independent and are not refit for each of the three foam densities. Figure 1 compares simple compression/tension experimental data (solid lines) with corresponding calculations using the fitted model (dashed lines). The quality of the comparison between the experimental data and the fitted model for both the axial engineering stress and the lateral engineering strain data and for all three densities is quite reasonable.

8 Validation experiments and simulations

In this section, we validate the predictive capability of our hyperelastic constitutive theory by comparing model predictions against experimental measurements in settings involving inhomogeneous deformation. To probe the model in a variety of situations, i.e., compression, shear, and

[6] Using (7.7), the exact expression for the ground-state bulk modulus is $B_0 = B(d^2 f/dK_1^2|_{K_1=0}) = B[1 + C_3 r J_{\min}/(1 - J_{\min})]$. To fit the rapidly stiffening behavior in compression, we take $C_3 \ll 1$, and hence, $B_0 \approx B$.

Density	Density-dependent				Density-independent									
	G_0 [kPa]	B [kPa]	$J_{\min}$	C_1	K_1^0	Δ_K	X_1'	X_2'	C_0	p	q	r	C_2	C_3
Low	34.5	58.7	0.12	2.5										
Moderate	65.2	117.4	0.16	1.9	-0.21	0.2	3.7	0.22	0.1	4	5	2	9	0.026
High	102.0	193.8	0.19	1.9										

Table 2: Material parameters for low, moderate, and high density Poron XRD foams. In total, fourteen parameters are utilized, with four density-dependent parameters and ten density-independent parameters.

tension-dominated situations, we consider three specific types of validation tests: (1) spherical and conical indentation, (2) simple-shear-like deformation both without and with a fixed amount of pre-compression, and (3) tension of a specimen with circular holes. The constitutive model of Section 7 has been numerically implemented in Abaqus/Standard (Abaqus, 2018) using a user-material (UMAT) subroutine, and throughout this section, we obtain model predictions in inhomogeneous deformation scenarios using finite-element calculations in Abaqus/Standard.

8.1 Spherical and conical indentation

We begin by considering indentation – a validation case that involves compression-dominated deformation directly beneath the indenter – for both spherical and conical indenter geometries. As discussed in Section 6, indentation experiments are conducted on foam specimens with a square 25.4×25.4 mm^2 cross section and a height of $H = 12.9$ mm. One square face of each specimen is constrained by a bonded aluminum backer, and the specimen is indented on the opposite unconstrained face. Spherical indentation is performed using a steel indenter tip with a radius of $r = 3.97$ mm, and conical indentation is performed using an aluminum indenter tip with a base angle of $\theta = 30°$. Photographs of the experimental setup prior to deformation for spherical and conical indentation are shown in Figs. 16(a) and (c), respectively. Experiments are performed at an indenter displacement-rate of $\dot{\delta} = 2.0 \times 10^{-3}$ mm/s for spherical indentation and $\dot{\delta} = 2.5 \times 10^{-3}$ mm/s for conical indentation. The maximum indenter displacements achieved during spherical and conical indentation are around 4 mm in all cases. The experimentally-measured indenter force P versus displacement δ relations for spherical and conical indentation are shown as solid lines in Figs. 16(b) and (d), respectively. In both cases, data for all three foam densities are shown. As in Fig. 1, the shaded regions surrounding the solid curves represent one standard deviation above and below the average across all nine instances of the experiment, and the arrows indicate loading and unloading. Hysteresis is minimal, demonstrating that the chosen indenter displacement-rates are sufficiently slow.

For the corresponding finite-element simulations, we idealize the geometry as axisymmetric for computational efficiency. This involves idealizing the cuboid foam specimen as a disk of radius R_0 and height $H = 12.9$ mm. The outer radius is set to be $R_0 = 14.4$ mm, which is the average value of the outer radius of the square specimen over the angular coordinate.[7] The axisymmetric

[7]We have performed selected three-dimensional simulations, in which the experimental geometry is exactly represented, and the corresponding simulated indenter force versus displacement result is indistinguishable from the

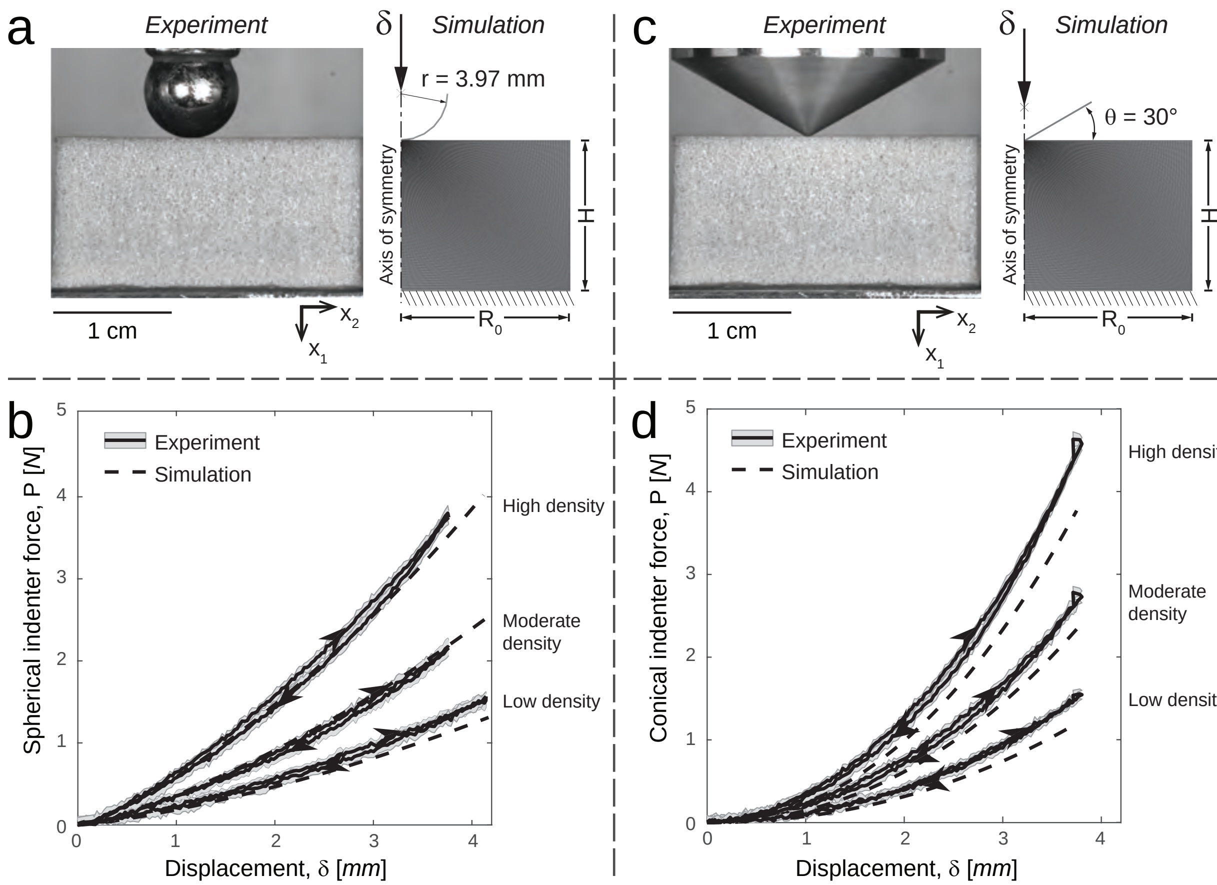

Figure 16: Spherical and conical indentation validation tests. Snapshots of the experimental setup prior to deformation and the corresponding finite-element configurations are given for (a) spherical and (c) conical indentation. Indenter force P versus indenter displacement δ for (b) spherical and (d) conical indentation. Solid lines with shaded error regions represent experimental data, and dashed lines are the predictions from the constitutive model.

finite-element configurations for spherical and conical indentation are shown in Figs. 16(a) and (c), respectively. The foam substrate is meshed using 17,236 Abaqus-CAX4H elements (four-node, axisymmetric, quadrilateral, constant-pressure elements) and the indenters are idealized as rigid surfaces. Contact between the foam substrate and the indenter is approximated as rough – i.e., no slip – in both cases.[8] Regarding boundary conditions, to model the fixed-base boundary condition, all displacement components are prescribed to be zero on the bottom face of the mesh. The left face of the mesh is coincident with the axis of symmetry, and hence, the horizontal displacement is set to zero along this face. The right face of the mesh is left unconstrained. The calculated indenter force P versus displacement δ relations – obtained without any parameter adjustment – are included as dashed lines for all three foam densities in Figs. 16(b) and (d). Generally, there is

axisymmetric result, verifying that the axisymmetric idealization is valid.

[8]We have performed corresponding simulations with frictionless interaction between the foam substrate and the indenter, and the difference between the rough and frictionless cases is negligible, indicating that the role of surface friction is small in indentation of compressible foam materials.

good agreement between the experimentally-measured and simulated responses, especially for the case of spherical indentation.[9]

8.2 Simple-shear-like deformation without and with pre-compression

Next, we validate aspects of the model related to shear-dominated deformation. We perform two types of experiments, carried out on foam cuboids with a square cross-section of side-length $W = 30\,\mathrm{mm}$ and a height of $H = 12.9\,\mathrm{mm}$. First, we subject foam cuboids to simple-shear-like deformation, in which one square face is translated parallel to the other by a shear displacement δ. In these experiments, the square faces are constrained by bonded aluminum backers, and the shear displacement is applied by moving one backer at a rate of $\dot{\delta}/H = 2.0 \times 10^{-4}\,\mathrm{s}^{-1}$ to a maximum shear displacement of $\delta/H = 0.5$ and then unloading, while the other backer remains fixed, and the distance between the backers is held at H. Notably, all rectangular side-faces remain unconstrained, so that edge-effects are present, and hence, deformation is simple-shear-like but inhomogeneous. In the second type of experiment, we consider simple-shear-like deformation with a fixed uniaxial pre-compression as an example of coupled distortional/volumetric deformation. The simple-shear-like experiment with pre-compression is carried out in two steps. First, the specimen is compressed, such that the deformed distance between the constrained faces is $0.75H$. Specimens are then allowed to rest for at least 40 minutes, while the pre-compression is held fixed in order to allow complete relaxation of viscoelastic material behavior. Second, the specimen is sheared by a shear displacement δ at the same rate of $\dot{\delta}/H = 2.0 \times 10^{-4}\,\mathrm{s}^{-1}$ to a maximum shear displacement of $\delta/H = 0.375$ and then unloaded, while the distance between the constrained faces is held fixed at $0.75H$. In both types of experiments, we utilize the double-shear fixture pictured in Fig. 17(a), which is akin to a double-lap or three-bar (e.g., ASTM D4255 Procedure B) shear design. In this configuration, two specimens are tested simultaneously in order to maintain symmetry, and therefore, the resultant shear force P is identified as half the force applied to the moving center platen. The measured normalized shear force P/W^2 versus shear displacement δ relations for all three foams densities and both without and with pre-compression are shown as solid lines in Fig. 17(c). As before, the shaded regions denote the range of one standard deviation above and below the average experimental measurement, and the arrows denote loading and unloading, demonstrating minimal hysteresis. Two features are notable in the force-displacement relations. First, in shear-dominated deformation, no plateau region is observed, and the slope of the force-displacement relation increases slightly as deformation progresses. Second, when pre-compression is applied, the force-displacement relation becomes more compliant, illustrating the interaction between volumetric and distortional aspects of the material response.

For the corresponding finite-element simulations, a fully three-dimensional model is utilized. The reference finite-element mesh, consisting of 97,200 Abaqus-C3D8H elements (eight-node, three-dimensional, hexahedral, constant-pressure elements) is shown in Fig. 17(a). Regarding boundary conditions, for simple-shear-like deformation *without* pre-compression, the right face of the mesh in Fig. 17(a) represents the fixed backer, on which all displacement components are

[9] We note that for the conical indentation case, the indenter forces predicted by the model are slightly lower than the corresponding experimental data, which may be rationalized as follows. To optimize the stability of the model, the fitted volumetric response function, df/dK_1, slightly underestimates experimental data. The under-prediction in the conical indenter force is associated with the large volumetric deformations that occur during conical indentation, as compared to spherical indentation, which is slightly less volumetrically-dominated.

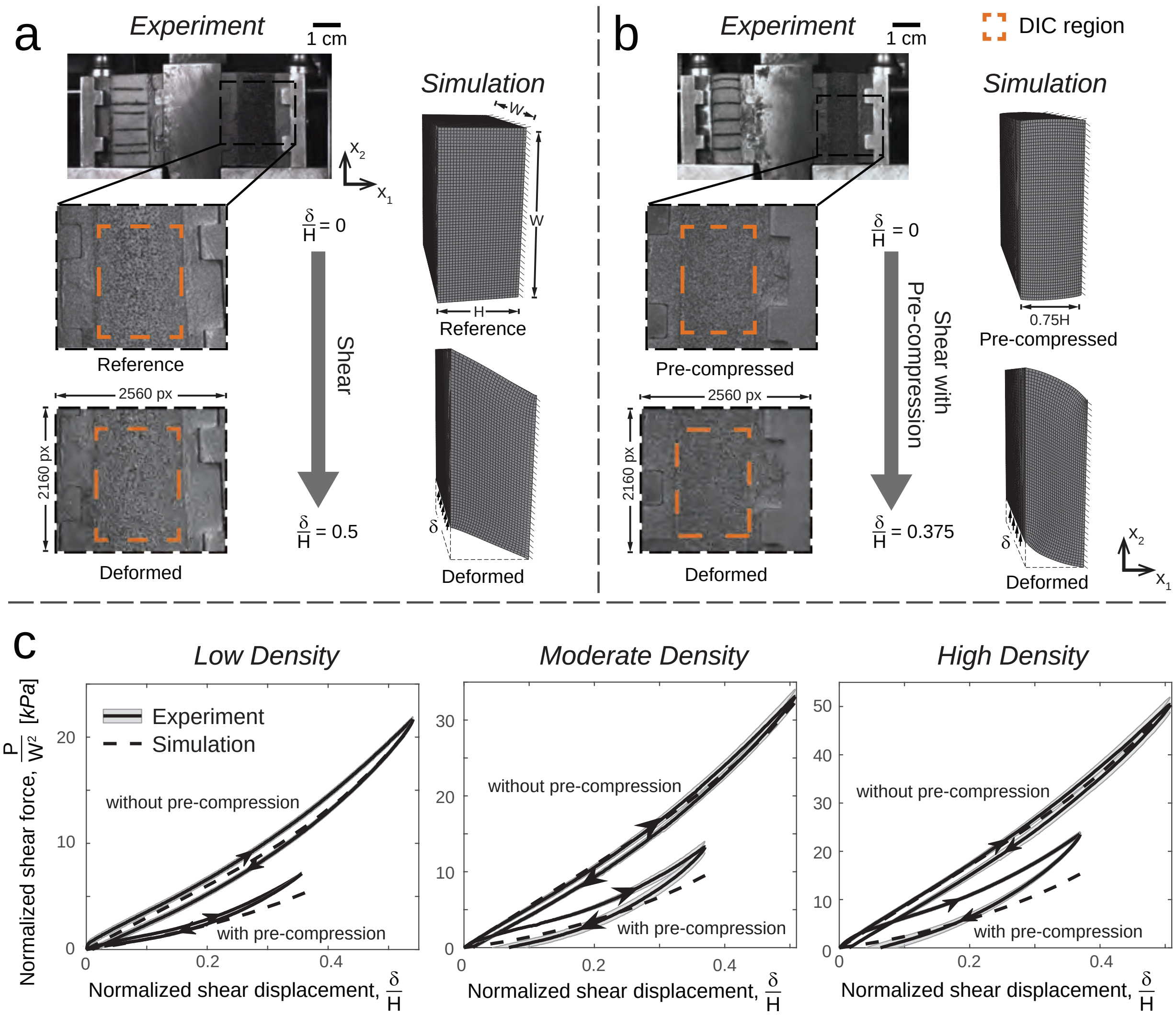

Figure 17: Simple-shear-like validation tests both without and with uniaxial pre-compression. (a) Snapshot of the double-shear fixture with two specimens prior to deformation and the experimental region-of-interest used for DIC imaging (approximately 1300×1200 px^2) in both the reference and the deformed states for the case without pre-compression. The corresponding finite-element configuration is shown on the right, also in both the reference and the deformed states. (b) Experimental images and finite-element configuration for the case with pre-compression (DIC region approximately 950×1200 px^2), displaying the pre-compressed and the deformed, sheared states. (c) Normalized shear force P/W^2 versus normalized shear displacement δ/H both without and with pre-compression and for all three densities. Solid lines with shaded error regions represent experimental data, and dashed lines are simulated predictions of the constitutive model.

prescribed to be zero. The left face of the mesh represents the moved backer, on which the vertical displacement u_2 is prescribed, while the other displacement components are constrained – i.e., $u_1 = 0$, $u_2 = \delta$, and $u_3 = 0$. The remaining faces are traction-free. The deformed mesh after a shear displacement of $\delta/H = 0.5$ is shown in Fig. 17(a), which upon close inspection, reveals the inhomogeneous nature of deformation near the boundaries in the simulation. For simple-shear-like deformation *with* pre-compression, pre-compression is applied by prescribing $u_1 = -0.25H$ and $u_2 = u_3 = 0$ on the right face of the mesh, while holding all displacement components at zero on the left face of the mesh. The deformed mesh after pre-compression is shown in 17(b), displaying some bulging in the vicinity of the traction-free faces. Then, a shear displacement is applied by fixing $u_1 = -0.25H$ and $u_2 = u_3 = 0$ on the right face of the mesh and prescribing $u_2 = \delta$ and $u_1 = u_3 = 0$ on the left face of the mesh. The deformed mesh after a shear displacement of $\delta/H = 0.375$ is shown in Fig. 17(b), displaying significant inhomogeneous deformation. The calculated shear force P versus shear displacement δ relations are included as dashed lines in Fig. 17(c) for each density both without and with pre-compression. For all densities, the model captures the features of the response both without and with pre-compression. In particular, it predicts both the lack of a plateau region in the response during shear-dominated deformation and the increased compliance with pre-compression. The ability of the model to capture the effect of pre-compression on the response in simple-shear-like deformation provides a partial validation of the coupled volumetric/distortional contribution to the free-energy function (7.2).

In addition to P versus δ relations, we also compare experimentally-measured and numerically-simulated displacement fields on the front face of the specimen. The DIC regions-of-interest are outlined with dashed lines in the reference, undeformed state and the deformed state at the maximum level of shear displacement for simple-shear-like deformation without and with pre-compression in Figs. 17(a) and (b), respectively, and contours of the two-dimensional, DIC-calculated displacement field – i.e., $u_1(x_1, x_2)$ and $u_2(x_1, x_2)$ – on the front face of the specimen in a representative experiment on the moderate density foam are shown in the left columns of Figs. 18(a) and (b). While in Fig. 18(a), the fields represent the displacement from the reference state to the deformed state, the fields in Fig. 18(b) for simple-shear-like deformation with pre-compression represent the displacement from the pre-compressed state to the deformed, sheared state.[10] The corresponding simulated displacement fields are shown in the right columns of Figs. 18(a) and (b), demonstrating that the salient features of the experimental displacement fields are captured by the model. In particular, inhomogeneous deformation occurring due to edge-effects are clearly apparent in the u_1-fields in both experiments and simulations. Overall, the magnitudes and distributions of both the u_1- and u_2-components of the displacement field are consistent between experiment and simulation.

8.3 Tension of a specimen with circular holes

Finally, we conduct a validation test to evaluate the predictive capability of the constitutive model in a tension-dominated setting. Given the favorable comparisons of model predictions and experiments across all three densities in the cases of indentation and simple-shear-like deformation, we focus only on the high density foam in this final test. To obtain inhomogeneous deformation fields, we take inspiration from the work of Wang and Chester (2018) and cut circular holes in our tension specimens. Specifically, we begin with the dogbone geometry used in the simple tension characterization experiments described in Section 6 and laser-cut six, non-overlapping circular holes, each with a radius of 2.5 mm, at arbitrarily-chosen locations in the gage-section. This creates a purposefully asymmetric geometry, which is shown in Fig. 19(a). These modified specimens

[10]This exception in the definition of the displacement field is only made in Fig. 18(b), and for notational economy, we continue to denote the displacement components as u_1 and u_2.

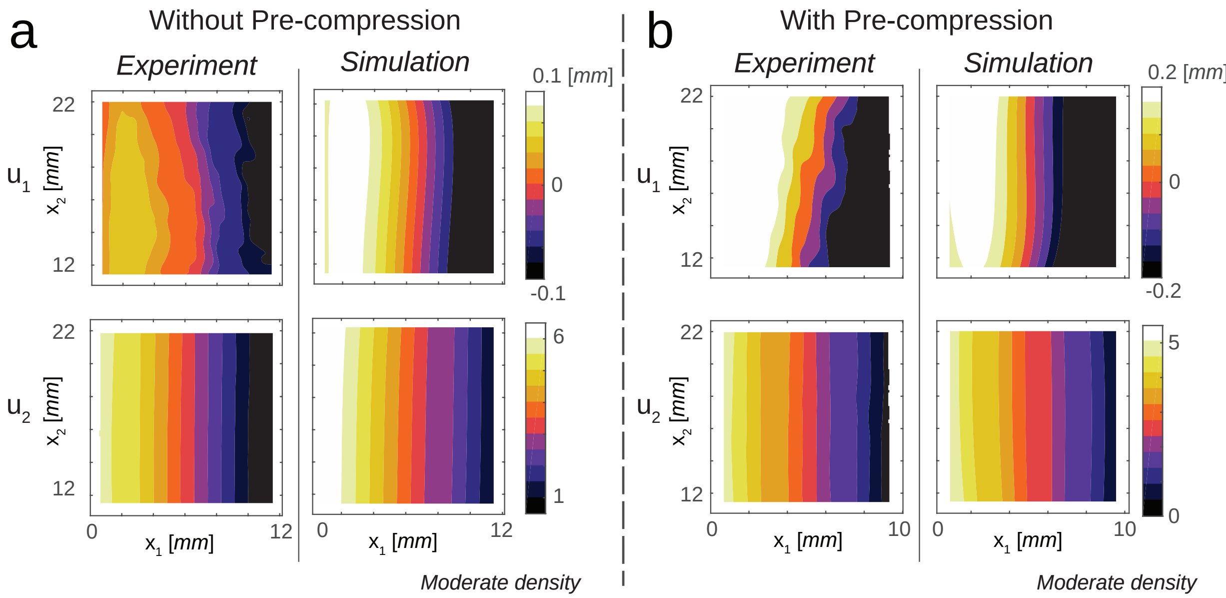

Figure 18: Contours of the two-dimensional displacement field – i.e., $u_1(x_1, x_2)$ and $u_2(x_1, x_2)$ – on the front face of the specimen in the DIC region-of-interest from both experiment and simulation for simple-shear-like deformation (a) without pre-compression and at a shear displacement of $\delta/H = 0.5$ and (b) with pre-compression and at a shear displacement of $\delta/H = 0.375$ for the moderate density foam. For simple-shear-like deformation with pre-compression, the fields represent the displacement from the pre-compressed state to the deformed, sheared state.

are then subjected to a tension-testing procedure analogous to that described in Section 6 for homogeneous simple tension experiments. The bottom grip is fixed, and the top grip moves upward at a displacement rate of $\dot{\delta} = 2.0 \times 10^{-3}$ mm/s. The measured tension force P as a function of the top grip displacement δ is shown in Fig. 19(b) as a solid line. As before, the shaded area denotes the range of one standard deviation above and below the average experimental measurement, and the arrows denote loading and unloading, demonstrating minimal hysteresis.

In the corresponding finite-element simulations, we model only the region between the grips, consisting of the gage-section and the section of the specimen between the grips and the gage-section. The specimen is modeled in three dimensions, matching the experimental geometry, and meshed with 185,216 Abaqus-C3D8H three-dimensional elements, as shown in Fig. 19(a). The front and back faces of the mesh as well as the side faces and the interior faces of the holes are traction-free. Regarding displacement boundary conditions, the bottom of the mesh is fully constrained – i.e., $u_1 = u_2 = u_3 = 0$ – and on the top surface of the mesh the vertical displacement u_2 is prescribed, while the other displacement components are constrained – i.e., $u_1 = 0$, $u_2 = \delta$, and $u_3 = 0$. Fig. 16(b) shows the numerically-predicted force-displacement response as a dashed line, showing excellent agreement with the experimentally-measured relation.

As in the simple-shear-like validation case, we also compare experimentally-measured and numerically-simulated displacement fields on the front face of the specimen. The DIC region-of-interest is shown both in the reference state as well as the deformed state after a top-grip displacement of $\delta = 8.25$ mm in Fig. 19(a), outlined with dashed lines, and contours of the two-dimensional, DIC-calculated displacement field – i.e., $u_1(x_1, x_2)$ and $u_2(x_1, x_2)$ – on the front face of

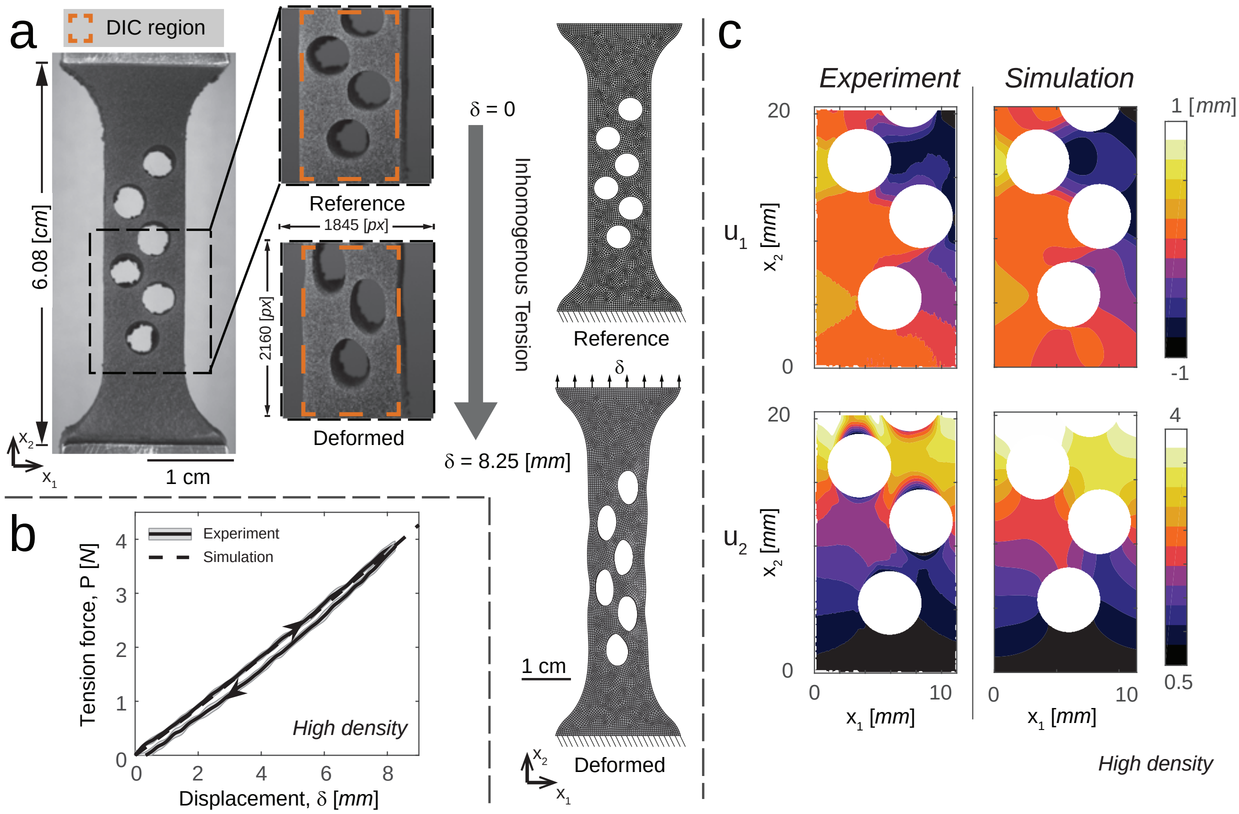

Figure 19: A tension-dominated validation test for the high density foam consisting of tension of a specimen with circular holes, in which a standard dogbone geometry is modified with six asymmetrically-placed 2.5 mm radius holes. (a) Snapshot of the experimental specimen prior to deformation and the experimental region-of-interest used for DIC imaging in both the reference and the deformed states (DIC region approximately 1100×2000 px^2) as well as the corresponding finite-element configurations. (b) The top-grip force P versus displacement δ, in which solid lines with shaded error regions represent experimental data, and dashed lines are simulated predictions of the constitutive model. (c) Contours of the two-dimensional displacement field – i.e., $u_1(x_1, x_2)$ and $u_2(x_1, x_2)$ – on the front face of the specimen in the DIC region-of-interest from both experiment and simulation.

the specimen in a representative experiment are plotted in Fig. 19(c). The corresponding simulated front-face displacement fields are plotted alongside the experimental results in Fig. 19(c). There is strong quantitative agreement between the experimentally-measured and simulated displacement fields throughout the region-of-interest. The notable differences, specifically, the displacement gradients near the tops and bottoms of the holes in the experimental results, arise as an artifact of incorporating internal material-void boundaries within an Eulerian framework for the hybrid, cumulative-iterative displacement summation scheme used in the qDIC algorithm and subsequent plotting in the reference configuration.

9 Discussion of the hyperelastic model

9.1 Stability

A common drawback of stretch-based, compressible hyperelastic models (Ogden, 1972a; Storakers, 1986) is unstable behavior that limits the deformation range over which the model may be robustly applied. In this section, we examine the stability of the proposed hyperelastic model and illustrate the limits of stable behavior. Here, we assess stability by testing the ellipticity of the quasi-static governing equations – i.e., testing that the eigenvalues of the acoustic tensor in the deformed configuration remain positive for given homogeneous base states of deformation (e.g., Thomas, 1961; Hill, 1962; Triantafyllidis and Aifantis, 1986; Bigoni, 2012). For a homogeneous base state of deformation, the spatial acoustic tensor for a hyperelastic material is

$$Q_{ik}(\mathbf{n}) = \mathbb{C}_{ijkl} n_j n_l \quad \text{with} \quad \mathbb{C}_{ijkl} = J^{-1} F_{jn} F_{lq} \frac{\partial^2 \psi}{\partial F_{in} \partial F_{kq}}, \tag{9.1}$$

where $\mathbb{C}_{ijkl}$ are the spatial moduli, evaluated at the base state, and $\mathbf{n}$ is a unit vector. Details of the steps leading to (9.1) as well as an expression for the spatial moduli $\mathbb{C}_{ijkl}$ that is appropriate for use with a logarithmic-strain-based free-energy function are given in Appendix C. If the eigenvalues of $\mathbf{Q}(\mathbf{n})$ for a given base state of deformation remain positive for all unit vectors $\mathbf{n}$, the ellipticity of the governing equations is maintained, and homogeneous deformation is stable. However, if an eigenvalue of $\mathbf{Q}(\mathbf{n})$ is negative for any unit vector $\mathbf{n}$, the localization of deformation into bands becomes possible. To test for stability, we consider base states of deformation described by a spatial logarithmic strain tensor, $\mathbf{E}$, with invariants $\{K_1, K_2, K_3\}$ and principal directions $\{\mathbf{l}_1, \mathbf{l}_2, \mathbf{l}_3\}$ and all unit vectors $\mathbf{n}$ in three dimensions – i.e., $\mathbf{n} = \cos\theta \sin\gamma \mathbf{l}_1 + \sin\theta \sin\gamma \mathbf{l}_2 + \cos\gamma \mathbf{l}_3$ over the ranges $0 \le \theta \le 2\pi$ and $0 \le \gamma \le \pi$. In this way, we may identify whether unstable behavior is possible for a given combination of invariants $\{K_1, K_2, K_3\}$.[11]

Representative stability maps, generated using the free-energy density function introduced in Section 7 and the material parameters for the moderate density foam from Table 2, are shown in Fig. 20. Three specific modes of loading are considered in Fig. 20: (a) $K_3 = 1$ (simple tension), (b) $K_3 = -1$ (simple compression), and (c) $K_3 = 0$ (simple shear). Stable combinations of $\{K_1, K_2, K_3\}$ are denoted as white regions, while combinations of $\{K_1, K_2, K_3\}$ in which at least one eigenvalue of $\mathbf{Q}(\mathbf{n})$ is negative for at least one unit vector $\mathbf{n}$ are denoted as gray regions. In Figs. 20(a) and (b), the deformation paths for simple tension and simple compression are shown as solid lines, and in Fig. 20(c), an idealized homogeneous loading path for simple shear, representative of the inhomogeneous simple-shear-like deformation of Section 8.2, is shown. In all cases, the deformation paths traverse stable states.

While large regions of stable behavior are evident in Fig. 20, unstable behavior is also observed. The sources of unstable behavior may be linked to features of the model. First, the unstable regions in the bottom left corners of Figs. 20(a), (b), and (c) arise because $X(K_1)$ is negative in this range when the material parameters for the moderate density foam are utilized. The phenomenological form for $X(K_1)$ (7.5) is an increasing function of K_1, which is enforced to be positive over the fitted range; however, for sufficiently negative values of K_1, $X(K_1) < 0$, leading to unstable behavior.

[11] We also utilize the analytical necessary and sufficient conditions for strong ellipticity of Dacorogna (2001) as an independent verification of the results presented in this section.

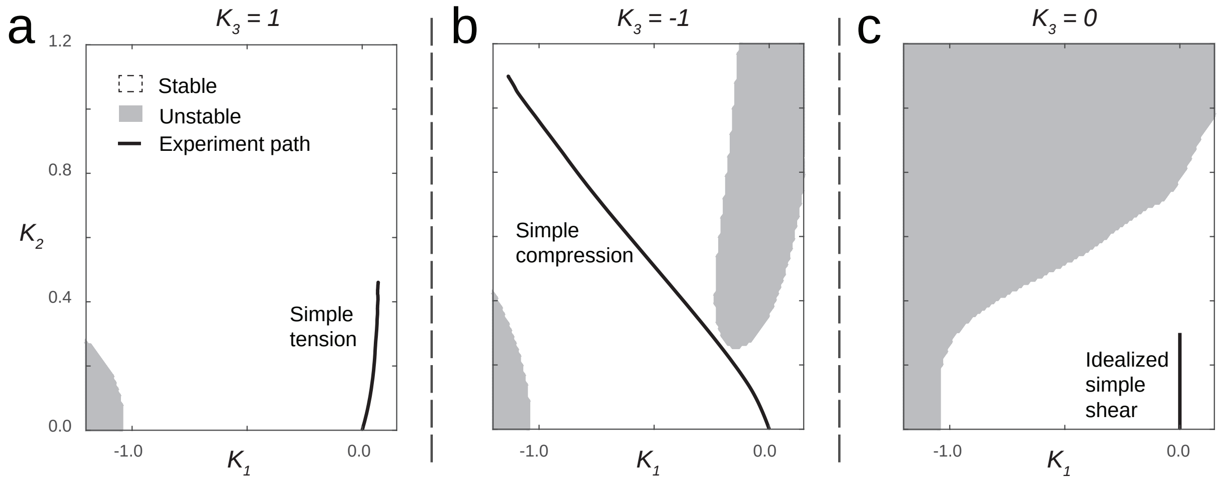

Figure 20: Stability diagrams calculated using a loss-of-ellipticity test as a function of the invariants of the logarithmic strain K_1 and K_2 for several cases of fixed K_3: (a) $K_3 = 1$ (simple tension), (b) $K_3 = -1$ (simple compression), and (c) $K_3 = 0$ (simple shear). The white regions indicate stable behavior, while gray regions indicate the potential for unstable behavior. Solid lines correspond to representative deformation paths from simple tension, simple compression, and idealized simple shear, respectively.

If necessary, the functional form (7.5) may be extended to be positive for all K_1 to increase stable behavior. Second, since $dX/dK_1 > 0$ for all K_1, the shear-induced mean stress, $G_0(dX/dK_1)K_2^2$, is positive and may be of arbitrarily large magnitude as K_2 increases, leading to unstable behavior. In particular, the unstable region in the upper right domain of Fig. 20(b) is due to this effect. This feature is due to the low-order K_2-dependence of the coupled volumetric/distortional response and cannot be remedied by modifying the forms of the fitting functions. Instead, it would require an alternate structure for the decomposition of the free-energy function (7.2). Finally, unstable behavior for high values of K_2 can arise due to the higher-order distortional response function, $L(K_2, K_3)$, and its dependence on K_3. In particular, the unstable behavior in the top region of Fig. 20(c) is due to this effect. The functional form (7.6) may be extended with higher-order K_2-terms – perhaps motivated by locking behavior in the distortional response – to suppress unstable behavior for large values of K_2. In sum, the model exhibits robust, largely-stable behavior as evidenced by Fig. 20 as well as the numerical solutions obtained across a diverse set of inhomogeneous deformation scenarios in Section 8.

9.2 Comparison to other models

In this section, we compare the ability of the proposed model to capture experimental data with that of other important hyperelastic models for porous elastomers in the literature. We begin with the classic model of Blatz and Ko (1962) – a phenomenological, invariant-based free-energy function for porous elastomers – which depends on the second and third principal invariants of $\mathbf{C}$ as follows:

$$\psi = \frac{G_0}{2}\left(\frac{I_2}{I_3} + 2\sqrt{I_3} - 5\right), \tag{9.2}$$

where G_0 is the ground-state shear modulus of the foam. We note that (9.2) represents a simplified version of a broader three-parameter model and implies a ground-state Poisson's ratio of 0.25. Since the ground-state Poisson's ratio of the moderate density Poron XRD foam is about 0.27, we utilize the simplified form (9.2) along with the previously-fitted value of $G_0 = 65.2\,\text{kPa}$ (Table 2). The resulting engineering stress versus axial strain and lateral strain versus axial strain response in simple compression/tension for the Blatz-Ko model is shown in Figs. 21(a) and (b) using square (□) markers along with the experimental data for the moderate density foam. As expected for the highly-porous foam under consideration, the Blatz-Ko model does a reasonable job capturing data in the low to moderate strain regime, i.e., axial engineering strains between approximately -0.1 and 0.2, but is not applicable beyond this regime.

Next, we consider two homogenization-based models for porous elastomers with spherical voids: the model of Danielsson et al. (2004) and the more recent model of Shrimali et al. (2019). Both models consider microstructures consisting of closed-cell voids and do not account for buckling in the elastomeric-matrix microstructure during compression. Therefore, they are limited in scope to low to moderate porosity foams, and we do not expect these models to capture experimental data for the highly-porous, open-cell foam under consideration. However, since these models are two of only a handful of explicit, compressible hyperelasticity models, we include them in our discussion for the sake of comparison. First, the approach of Danielsson et al. (2004), when specialized to the case of a neo-Hookean matrix, yields the following free-energy function that depends on the invariants $I_1 = \operatorname{tr}\mathbf{C}$ and $J = \det\mathbf{F}$:

$$\psi = \frac{G_\mathrm{m}}{2}\left[I_1\left(2 - \frac{1}{J} - \frac{\phi_0 + 2(J-1)}{J^{2/3}(1+(J-1)/\phi_0)^{1/3}}\right) - 3(1-\phi_0)\right], \tag{9.3}$$

where G_m is the ground-state shear modulus of the matrix material and ϕ_0 is the void volume fraction of the undeformed porous material. The ground-state shear modulus of the foam material is then $G_0 = G_\mathrm{m}(1-\phi_0)$. From Table 2, we take $G_0 = 65.2\,\text{kPa}$ and estimate $\phi_0 = 1 - J_\mathrm{min} = 0.84$, so that $G_\mathrm{m} = 407.5\,\text{kPa}$. The corresponding engineering stress versus axial strain and lateral strain versus axial strain response in simple compression/tension is shown in Figs. 21(a) and (b) using triangle (△) markers. We note that $\phi_0 = 1 - J_\mathrm{min}$ is a rough estimate of the initial void volume fraction. For this reason, we have considered values of ϕ_0 over the range $0.75 \le \phi_0 \le 0.95$, i.e., the typical range for the low, moderate, and high density Poron XRD foams, with $G_0 = 65.2\,\text{kPa}$ fixed and confirmed that within this range, the precise value of ϕ_0 has a minimal impact on the response shown in Figs. 21(a) and (b). Second, the homogenization-based free-energy function of Shrimali et al. (2019) – also specialized to the case of a neo-Hookean matrix – is

$$\psi = \frac{3G_\mathrm{m}(1-\phi_0)}{2(3+2\phi_0)}(I_1 - 3) + \frac{3G_\mathrm{m}}{2J^{1/3}}\left[2J - 1 - \frac{(1-\phi_0)J^{1/3}(3J^{2/3}+2\phi_0)}{3+2\phi_0} - \frac{\phi_0^{1/3}J^{1/3}(2J+\phi_0-2)}{(J-1+\phi_0)^{1/3}}\right], \tag{9.4}$$

where G_m and ϕ_0 continue to denote the ground-state shear modulus of the matrix material and the undeformed void volume fraction. The ground-state shear modulus of the foam material for this model is $G_0 = 3G_\mathrm{m}(1-\phi_0)/(3+2\phi_0)$, and again, we take $G_0 = 65.2\,\text{kPa}$ and $\phi_0 = 0.84$, so that $G_\mathrm{m} = 635.7\,\text{kPa}$ for this case. The corresponding response is included in Figs. 21(a) and (b) using star ($*$) markers. As for the model of Danielsson et al. (2004), we have confirmed that the response shown in Figs. 21(a) and (b) for the model of Shrimali et al. (2019) is minimally affected as the value of ϕ_0 is varied over the range $0.75 \le \phi_0 \le 0.95$, while $G_0 = 65.2\,\text{kPa}$ remains fixed. As

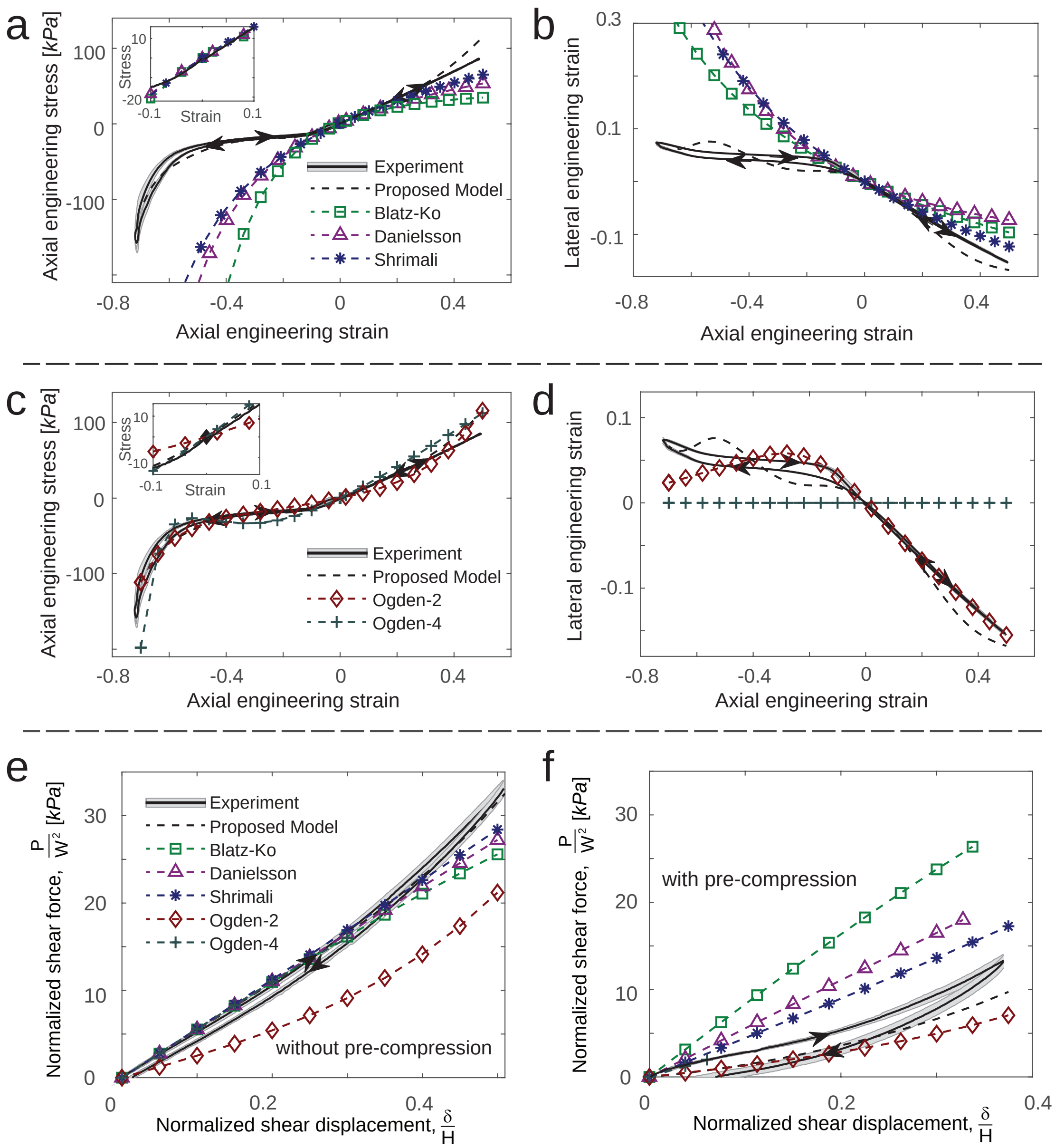

Figure 21: Comparison of fits obtained using hyperelastic models for porous elastomers in the literature with the proposed approach for the moderate density Poron XRD foam. (a) Axial engineering stress and (b) lateral engineering strain versus axial engineering strain fits for the proposed model, the Blatz and Ko (1962) model (Blatz-Ko), the Danielsson et al. (2004) model (Danielsson), and the Shrimali et al. (2019) model (Shrimali). (c) Axial engineering stress and (d) lateral engineering strain versus axial engineering strain fits for a two-term Ogden-Storakers fit (Ogden-2) and a four-term Ogden-Storakers fit (Ogden-4) (Ogden, 1972a; Storakers, 1986). (*Insets (a) and (c)*) Close-up of the moderate-strain regime. Normalized shear force P/W^2 versus normalized shear displacement δ/H for simple-shear-like deformation both (e) without and (f) with pre-compression for all models considered as well as experimental data for the moderate density Poron XRD foam.

expected, both models yield similar predictions and are capable of capturing data in the moderate strain regime but do not capture the response beyond this regime – especially the response in the plateau regime in compression.

Finally, we consider the stretch-based Ogden-Storakers model (Ogden, 1972a; Storakers, 1986). This is the most commonly utilized phenomenological hyperelasticity model for highly-compressible foams and is built in to Abaqus (2018) as the "hyperfoam" material. The free-energy function for the Ogden-Storakers model is given through the principal stretches $\{\lambda_1, \lambda_2, \lambda_3\}$ and $J = \lambda_1\lambda_2\lambda_3$ as

$$\psi = \sum_{n=1}^{N} \frac{2G_n}{\alpha_n^2} \left[\lambda_1^{\alpha_n} + \lambda_2^{\alpha_n} + \lambda_3^{\alpha_n} - 3 + \frac{1}{\beta_n} \left(J^{-\alpha_n\beta_n} - 1 \right) \right], \tag{9.5}$$

where N is the number terms and $\{G_n, \alpha_n, \beta_n\}$ are material properties for each term. We consider two-term and four-term fits, which we refer to as Ogden-2 and Ogden-4, respectively. For both cases, we utilize the material parameter fitting routines built in to Abaqus. The six parameters of the Ogden-2 fit were determined to be $\{G_1 = 24.4\,\text{kPa}, \alpha_1 = 8.31, \beta_1 = -0.154, G_2 = 4.18\,\text{kPa}, \alpha_2 = -1.39, \beta_2 = 7.71\}$, and the corresponding fitted response is shown in Figs. 21(c) and (d) using diamond ($\Diamond$) markers. Although the Ogden-2 fit captures the overall shape of the axial stress and lateral strain versus axial strain responses, the accuracy of the fit in the moderate-strain regime is sacrificed, as shown in the inset of Fig. 21(c). Regarding the Ogden-4 fit, we found that to enable the nonlinear fitting routine in Abaqus to converge, the lateral strain response must be fixed to zero, so that all $\beta_n = 0$ (see Fig. 21(d)). Hence, there are eight fitted parameters in total for the Ogden-4 fit, which were determined to be $\{G_1 = 568\,\text{kPa}, \alpha_1 = 0.867, G_2 = 610\,\text{kPa}, \alpha_2 = 0.859, G_3 = -1.71\,\text{MPa}, \alpha_3 = 0.165, G_4 = 627\,\text{kPa}, \alpha_4 = -0.477\}$. Although the axial stress versus axial strain response of the Ogden-4 fit – shown in Fig. 21(c) using plus (+) markers – more closely matches experimental data in the moderate-strain regime compared to the Ogden-2 fit, the response is non-monotonic in compression, which suggests unstable behavior. Indeed, the loss-of-ellipticity test reveals unstable behavior for a large set of deformation states for the Ogden-4 fit. For this class of highly-compressible, open-cell elastomeric foams, it is typically quite difficult to obtain a fit using stretch-based models that captures both the axial stress and lateral strain versus axial strain responses and behaves stably over a wide range of deformation states, and the inclusion of additional terms does not change this observation. For example, we have considered five-term and six-term Ogden-type fits, while taking all $\beta_n = 0$ so that the fits involve ten and twelve parameters, respectively, and we observe unstable behavior similar to that of the Ogden-4 fit.

We also compare predictions of all models considered in this section against the experimental data from inhomogeneous simple-shear-like deformation both without and with pre-compression described in Section 8.2. Model predictions are obtained using finite-element simulations, and the calculated shear force P versus shear displacement δ relations are shown in Figs. 21(e) and (f) along with experimental data for the moderate density foam. The Blatz-Ko model ($\square$) does not capture the increased compliance in shear with pre-compression, and while both homogenization-based models ($\triangle$ and $*$) do predict some increase in compliance with pre-compression, they do not quantitatively capture the normalized force versus displacement response in simple-shear-like deformation with pre-compression. The Ogden-2 fit ($\Diamond$) does not capture the experimental data for simple-shear-like deformation without pre-compression but is consistent with the data for simple-shear-like deformation with pre-compression. Finally, due to instabilities in the fitted model, numerical solutions using the Ogden-4 fit (+) cannot be obtained beyond moderate shear displacements

– namely, $\delta/H = 0.3$ and $\delta/H = 0.08$ for simple-shear-like deformation without and with pre-compression, respectively. These results illustrate the difficulties in robustly capturing experimental data for highly-compressible, open-cell elastomeric foams and the improved predictions enabled by the proposed approach.

10 Characterization and viscoelastic constitutive modeling of elastomeric foams at elevated strain-rates

The rate-dependent nature of elastomeric foams is an important aspect of their mechanical response, and developing predictive models for this behavior is important for use in design of these materials in practice. In this section, we describe our methodology for experimentally characterizing and constitutively modeling viscoelastic foams over the elevated strain-rate range of 10^{-3}-$10^{-1}\,\mathrm{s}^{-1}$ and apply our methodology to the high-density Poron XRD foam.

10.1 Experimental program

The experimental program for elevated strain-rate characterization of the polyurethane-based Poron XRD foam largely follows that of Section 6. Compression and tension specimens are the same as described in Section 6.2. For all elevated rate characterization experiments, a 3.25 hour or more wait time between repeated tests or alignment on a given specimen was maintained. The same system as described in Section 6.3 was operated at a higher crosshead speed in order to attain elevated strain-rates over the range of 10^{-3}-$10^{-1}\,\mathrm{s}^{-1}$. Since the apparatus involves a screw-driven stepper-motor system, displacement control is precise and contains few artifacts (e.g., due to inertia or feedback-loop control schemes) over this elevated strain-rate range. At the cross-head velocity required for simple tension at a strain-rate of $10^{-1}\,\mathrm{s}^{-1}$, which was the highest case, the actuator velocity reversal (i.e., constant positive velocity switching to constant negative velocity) is accomplished in approximately 0.05 s for an experiment with total test time of 10 s. The load cell and camera were operated using synchronized timing at a sampling frequency of up to 25 Hz via a LabView interface – approximately 250 data points for the fastest testing condition. This yielded both sufficient control and temporal resolution to effectively utilize this system for experiments at strain-rates over the range of 10^{-3}-$10^{-1}\,\mathrm{s}^{-1}$. In our experiments over the range of strain-rates 10^{-3}-$10^{-1}\,\mathrm{s}^{-1}$, no localization was observed, and thus, the same post-processing procedure as described in Section 6.4 is used to collect engineering axial strain, lateral strain, and stress data. Compression/tension experimental data for the high-density Poron XRD foam is shown in Fig. 22 for strain-rates of $10^{-3}\,\mathrm{s}^{-1}$, $10^{-2}\,\mathrm{s}^{-1}$, and $10^{-1}\,\mathrm{s}^{-1}$. As before, the black curves represent the average over all repetitions of the experiment, and the shaded areas represent one standard deviation above and below the average. Notably, there is strain-rate stiffening in the initial response and overall higher force levels in the loading potions of the curves. The onset of densification occurs earlier at higher strain-rates, and importantly, the energy dissipation dramatically increases with increasing rate, as evidenced by the increased hysteresis in the engineering stress/strain response.

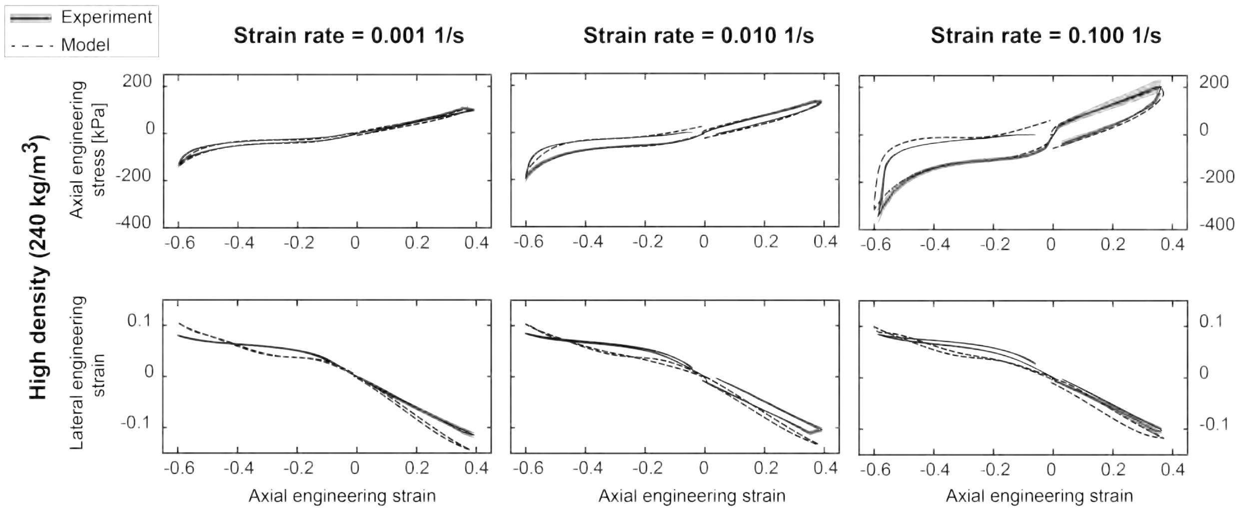

Figure 22: (Top) Axial engineering stress versus axial engineering strain and (bottom) lateral engineering strain versus axial engineering strain curves for high-density Poron XRD foam at strain-rates of $10^{-3}\,\mathrm{s}^{-1}$, $10^{-2}\,\mathrm{s}^{-1}$, and $10^{-1}\,\mathrm{s}^{-1}$.

10.2 Viscoelastic constitutive modeling

Next, we describe our isotropic, viscoelastic model for nonlinear, finite-deformation, rate-dependent behavior of non-localizing elastomeric foams. Our constitutive modeling approach is based upon a decomposition of the response into a hyperelastic, equilibrium response and a series of dissipative, non-equilibrium contributions. For conceptual clarity, this approach may be thought of as a nonlinear and finite-deformation generalization of the Maxwell-Wiechert model of linear viscoelasticity, shown schematically in Fig. 23.[12] With reference to the schematic, the left branch represents the equilibrium, hyperelastic response of the material, which is described by the model discussed in Section 7 with ψ_{eq} given by (7.2). The contribution to the Cauchy stress due to the equilibrium mechanism $\mathbf{T}_{\mathrm{eq}}$ is given by (7.3).

Then, the non-equilibrium, time-dependent material response is described by three nonlinear, Maxwell-like, non-equilibrium mechanisms in parallel with the equilibrium branch. For each mechanism – denoted by α – the deformation gradient $\mathbf{F}$ is multiplicatively decomposed (Kröner, 1960; Lee, 1969) into elastic and viscous parts as follows: $\mathbf{F} = \mathbf{F}^{\mathrm{e}(\alpha)}\mathbf{F}^{\mathrm{v}(\alpha)}$, where $\mathbf{F}^{\mathrm{e}(\alpha)}$, $J^{\mathrm{e}(\alpha)} = \det \mathbf{F}^{\mathrm{e}(\alpha)} > 0$, is the non-equilibrium elastic distortion and $\mathbf{F}^{\mathrm{v}(\alpha)}$, $J^{\mathrm{v}(\alpha)} = \det \mathbf{F}^{\mathrm{v}(\alpha)} > 0$, is the viscous distortion. The free energy due to each non-equilibrium mechanism $\psi_{\mathrm{neq}}^{(\alpha)}$ is based on the elastic logarithmic finite-strain tensor, utilizing the following definitions: $\mathbf{F}^{\mathrm{e}(\alpha)} = \mathbf{R}^{\mathrm{e}(\alpha)}\mathbf{U}^{\mathrm{e}(\alpha)}$, polar decomposition of $\mathbf{F}^{\mathrm{e}(\alpha)}$; $\mathbf{U}^{\mathrm{e}(\alpha)} = \sum_{i=1}^{3} \lambda_i^{\mathrm{e}(\alpha)} \mathbf{r}_i^{\mathrm{e}(\alpha)} \otimes \mathbf{r}_i^{\mathrm{e}(\alpha)}$, spectral decomposition of $\mathbf{U}^{\mathrm{e}(\alpha)}$; and $\mathbf{E}^{\mathrm{e}(\alpha)} = \sum_{i=1}^{3} (\ln \lambda_i^{\mathrm{e}(\alpha)}) \mathbf{r}_i^{\mathrm{e}(\alpha)} \otimes \mathbf{r}_i^{\mathrm{e}(\alpha)}$, the elastic logarithmic finite-strain tensor. The invariants

[12]To be clear, this illustration is only meant to guide ideas – our approach is not that of linear viscoelasticity. Our model is highly nonlinear and accounts for coupled distortional and volumetric deformation. Motivating nonlinear finite-deformation constitutive equations through rheological analogs is common in the literatures for polymer viscoplasticity (Mulliken and Boyce, 2006; Dupaix and Boyce, 2007; Anand et al., 2009; Silberstein and Boyce, 2010) and viscoelasticity of incompressible elastomers (Bergström and Boyce, 1998; Reese and Govindjee, 1998; Chester, 2012; Toyjanova et al., 2014).

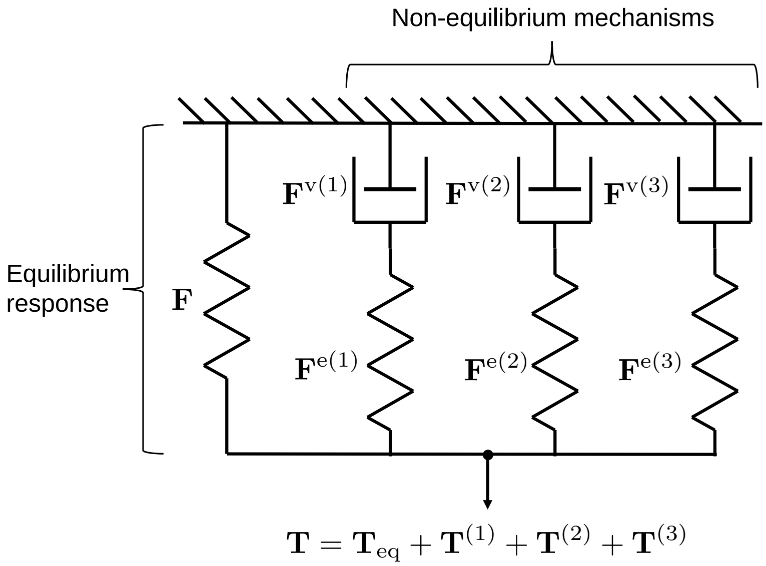

Figure 23: A rheological schematic of the Maxwell-Wiechert-type nonlinear, finite-deformation, viscoelastic constitutive model.

of $\mathbf{E}^{\mathrm{e}(\alpha)}$ are defined as in Section 7.2, i.e., $K_1^{\mathrm{e}(\alpha)} = \mathrm{tr}\,(\mathbf{E}^{\mathrm{e}(\alpha)})$, $K_2^{\mathrm{e}(\alpha)} = |\mathrm{dev}\,(\mathbf{E}^{\mathrm{e}(\alpha)})|$, and $K_3^{\mathrm{e}(\alpha)} = 3\sqrt{6}\,\det(\mathrm{dev}\,(\mathbf{E}^{\mathrm{e}(\alpha)})/K_2^{\mathrm{e}(\alpha)})$. Then, we take the constitutive equation for the non-equilibrium free-energy density $\tilde{\psi}_{\mathrm{neq}}^{(\alpha)}(K_1^{\mathrm{e}(\alpha)}, K_2^{\mathrm{e}(\alpha)}, K_3^{\mathrm{e}(\alpha)})$ for each mechanism α to be decomposed as follows:

$$\tilde{\psi}_{\mathrm{neq}}^{(\alpha)}(K_1^{\mathrm{e}(\alpha)}, K_2^{\mathrm{e}(\alpha)}, K_3^{\mathrm{e}(\alpha)}) = G_{\mathrm{neq}}^{(\alpha)}\left[X(K_1^{\mathrm{e}(\alpha)})K_2^{\mathrm{e}(\alpha)2} + L(K_2^{\mathrm{e}(\alpha)}, K_3^{\mathrm{e}(\alpha)})\right] + B_{\mathrm{neq}}^{(\alpha)} f(K_1^{\mathrm{e}(\alpha)}), \quad (10.1)$$

where $G_{\mathrm{neq}}^{(\alpha)}$ and $B_{\mathrm{neq}}^{(\alpha)}$ are the ground-state, non-equilibrium shear and bulk moduli, respectively, for each mechanism α, and X, L, and f are the same phenomenological fitting functions introduced in Section 7.4. The material parameters appearing in X, L, and f remain the same for the non-equilibrium branches as for the equilibrium branch with the exception of the parameters C_1 and p appearing in L, for which new parameters $C_{1\mathrm{neq}}$ and p_{neq} are introduced. The same values of $C_{1\mathrm{neq}}$ and p_{neq} are used for all non-equilibrium mechanisms. To reduce the number of fitting parameters, the ratio of the ground-state, non-equilibrium shear and bulk moduli, $G_{\mathrm{neq}}^{(\alpha)}/B_{\mathrm{neq}}^{(\alpha)}$, is taken to be constant across all mechanisms α and the same as G_0/B in the equilibrium response. Therefore, the fitting parameters associated with the non-equilibrium elastic responses are $\{G_{\mathrm{neq}}^{(1)}, G_{\mathrm{neq}}^{(2)}, G_{\mathrm{neq}}^{(3)}, C_{1\mathrm{neq}}, p_{\mathrm{neq}}\}$.

The stress conjugate to each elastic strain, $\mathbf{E}^{\mathrm{e}(\alpha)}$, is referred to as the Mandel stress:

$$\begin{aligned}\mathbf{M}^{\mathrm{e}(\alpha)} = \frac{\partial\tilde{\psi}_{\mathrm{neq}}^{(\alpha)}}{\partial\mathbf{E}^{\mathrm{e}(\alpha)}} &= \left(G_{\mathrm{neq}}^{(\alpha)}\frac{dX}{dK_1^{\mathrm{e}(\alpha)}}K_2^{\mathrm{e}(\alpha)2} + B_{\mathrm{neq}}^{(\alpha)}\frac{df}{dK_1^{\mathrm{e}(\alpha)}}\right)\mathbf{1} \\ &\quad + G_{\mathrm{neq}}^{(\alpha)}\left(2X(K_1^{\mathrm{e}(\alpha)})K_2^{\mathrm{e}(\alpha)} + \frac{\partial L}{\partial K_2^{\mathrm{e}(\alpha)}}\right)\mathbf{N}^{\mathrm{e}(\alpha)} + G_{\mathrm{neq}}^{(\alpha)}\frac{\partial L}{\partial K_3^{\mathrm{e}(\alpha)}}\frac{1}{K_2^{\mathrm{e}(\alpha)}}\mathbf{Y}^{\mathrm{e}(\alpha)}, \quad (10.2)\end{aligned}$$

where $\mathbf{N}^{\mathrm{e}(\alpha)} = \mathrm{dev}\,(\mathbf{E}^{\mathrm{e}(\alpha)})/K_2^{\mathrm{e}(\alpha)}$ and $\mathbf{Y}^{\mathrm{e}(\alpha)} = 3\sqrt{6}\mathbf{N}^{\mathrm{e}(\alpha)2} - \sqrt{6}\mathbf{1} - 3K_3^{\mathrm{e}(\alpha)}\mathbf{N}^{\mathrm{e}(\alpha)}$. The contribution to the Cauchy stress due to each non-equilibrium mechanism α is given through $\mathbf{T}^{(\alpha)} =$

Density	Non-equilibrium							
	$G^{(1)}_{\mathrm{neq}}$ [kPa]	$\tau^{(1)}$ [s]	$G^{(2)}_{\mathrm{neq}}$ [kPa]	$\tau^{(2)}$ [s]	$G^{(3)}_{\mathrm{neq}}$ [kPa]	$\tau^{(3)}$ [s]	$C_{1\mathrm{neq}}$	p_{neq}
High	28	60	50	8	800	0.2	2	4

Table 3: Non-equilibrium material parameters for high density Poron XRD foam. In total, eight parameters are needed in addition to the equilibrium material parameters given in Table 2.

$J^{\mathrm{e}(\alpha)-1}\mathbf{R}^{\mathrm{e}(\alpha)}\mathbf{M}^{\mathrm{e}(\alpha)}\mathbf{R}^{\mathrm{e}(\alpha)\top}$, and the total Cauchy stress is then $\mathbf{T} = \mathbf{T}_{\mathrm{eq}} + \sum_{\alpha=1}^{3} \mathbf{T}^{(\alpha)}$ (Anand et al., 2009).

Finally, the evolution of $\mathbf{F}^{\mathrm{v}(\alpha)}$ for each non-equilibrium mechanism α is given by

$$\dot{\mathbf{F}}^{\mathrm{v}(\alpha)} = \mathbf{D}^{\mathrm{v}(\alpha)}\mathbf{F}^{\mathrm{v}(\alpha)}, \quad \mathbf{F}^{\mathrm{v}(\alpha)}(\mathbf{X}, t = 0) = \mathbf{1}, \tag{10.3}$$

with the viscous stretching, $\mathbf{D}^{\mathrm{v}(\alpha)}$, given constitutively by

$$\mathbf{D}^{\mathrm{v}(\alpha)} = \frac{1}{2\eta^{(\alpha)}}\mathrm{dev}\left(\mathbf{M}^{\mathrm{e}(\alpha)}\right) + \frac{1}{9\kappa^{(\alpha)}}\mathrm{tr}\left(\mathbf{M}^{\mathrm{e}(\alpha)}\right)\mathbf{1}, \tag{10.4}$$

where $\eta^{(\alpha)}$ and $\kappa^{(\alpha)}$ are the shear and bulk viscosities for mechanism α. We reduce the number of material parameters by taking the ground-state relaxation time of the distortional and volumetric responses to be equal for each mechanism α, i.e., $\tau^{(\alpha)} = \eta^{(\alpha)}/G^{(\alpha)}_{\mathrm{neq}} = \kappa^{(\alpha)}/K^{(\alpha)}_{\mathrm{neq}}$. The fitting parameters associated with the non-equilibrium viscous responses are $\{\tau^{(1)}, \tau^{(2)}, \tau^{(3)}\}$.

Our viscoelastic model has been fit to our simple compression/tension experimental data for the high-density Poron XRD foam material at strain-rates of 10^{-3}, 10^{-2}, and 10^{-1} s^{-1}, shown in Fig. 22 with solid lines denoting experimental data and dashed lines denoting the model fit. To capture the non-quasistatic response over three decades of strain-rate, eight additional parameters are required, which are summarized in Table 3, keeping in mind that $G^{(\alpha)}_{\mathrm{neq}}/B^{(\alpha)}_{\mathrm{neq}} = G_0/B$ for all α and $\tau^{(\alpha)} = \eta^{(\alpha)}/G^{(\alpha)}_{\mathrm{neq}} = \kappa^{(\alpha)}/B^{(\alpha)}_{\mathrm{neq}}$ for each α. Of particular note, the model is able to capture the observed rate-dependence in the engineering stress/strain response, including the increasing hysteresis upon unloading seen with increasing strain-rate. Importantly, the model also captures the lateral strain behavior reasonably well. The ability to simultaneously describe strain-rate sensitivity, unloading behavior, and lateral behavior makes our model more complete than other existing viscoelastic modeling approaches in the literature (cf., e.g., Yang and Shim (2004); Bergström (2006); Anani and Alizadeh (2011); Briody et al. (2012); Ju et al. (2015)).

11 Concluding remarks

11.1 Summary

The major contributions of this work are summarized below:

- We have introduced a new 2D DIC technique, based on our previously developed finite deformation IDM FIDVC technique, that incorporates the concept of a cross-correlation quality factor. Two q-factors were utilized in this new qDIC technique, the peak-to-correlation-energy ratio and the peak-to-information-entropy. The q-factors improved the robustness and accuracy of the DIC for distorted speckle patterns arising from large finite deformations. By including the q-factors as a metric for image decorrelation, an intelligent hybrid incremental-cumulative switching scheme was implemented. The new qDIC algorithm showed improved performance over our previous FIDIC across all validation and benchmarking cases, i.e., rigid-body, homogeneous and inhomogenous modes of deformation displacement fields. To increase access to DIC and promote engagement in the development process of tools widely used in experimental mechanics, the open source codebase for qDIC is freely available to download from the Franck Lab GitHub page (https://github.com/FranckLab).

- We presented an extensive new set of quasi-static (low strain-rate) experiments on three densities of the polyurethane-based, open-cell elastomeric foam "Poron XRD". Experiments consisted of homogeneous simple compression/tension as well as three types of inhomogeneous experiments: spherical and conical indentation, simple-shear-like deformation without and with pre-compression, and tension of a specimen with circular holes.

- A phenomenological, isotropic, finite-deformation, hyperelastic constitutive model based on invariants of the logarithmic, Hencky strain was proposed. A key simplifying assumption of our modeling approach is that volumetric/distortional coupling only involves low-order dependence on the magnitude of distortional deformation – which leads to a more straightforward interpretation of the fitting functions and a systematic path for material parameter estimation from simple compression/tension data (see Appendix B). In compression and tension, the fitted model for each of the three densities of Poron XRD faithfully captures the nonlinear stress versus axial strain and lateral strain versus axial strain responses, in particular, the tension/compression asymmetry featuring a nearly-flat plateau regime in compression. All simple compression/tension experimental data and resulting fitted model data for Poron XRD has been made available to the community via GitHub (https://github.com/FranckLab).

- The constitutive model was implemented in Abaqus (2018) using a user-material subroutine, which was used to obtain model predictions in inhomogeneous deformation settings for the purpose of validation. The model predictions were shown to be consistent with experimental data in the inhomogenous validation cases across compression, shear, and tension-dominated settings. The user-material subroutine implementation of the constitutive model and sample input files for several of the validation cases have been made available to the community (https://github.com/HenannResearchGroup).

- The characterization and modeling methodology has been extended to the elevated strain-rate range of 10^{-3}-10^{-1} s^{-1}. We presented a set of homogeneous simple compression/tension experiments on the high-density Poron XRD foam and proposed a phenomenological, finite-deformation viscoelastic constitutive model, based on a decomposition of the response into a hyperelastic, equilibrium response and a series of dissipative, non-equilibrium mechanisms. The fitted model captures the observed rate-dependence of the engineering stress/strain response, including hysteretic behavior upon unloading, as well as the lateral strain versus axial strain response.

11.2 Limitations and future work

There are numerous avenues for improvement and future work – several of which are discussed below:

- Although notably improved performance is observed for the custom qDIC technique, more sophisticated q-factor based DIC schemes are possible in future development. To wit, future work includes implementing high-order shape function optimization with q-factors as a part of the matching routine to initialize the IDM.

- This project focused on a single polyurethane-based, open-cell elastomeric foam material over a moderate range of densities. We expect that the mechanical behavior of other open-cell foam materials may be well captured by the proposed models, so long as the material does not exhibit discernible strain localization. Future work will apply the proposed modeling approach to other elastomeric foam materials.

- We expect that improvements will be made to the phenomenological fitting functions utilized in the present work, either driven by additional experimental data for different elastomeric foam materials or motivated by micromechanical arguments.

- Furthermore, while the hyperelastic model has been tested in compression, shear, and tension-dominated situations, model validation has not exhaustively spanned all combinations of the invariants $\{K_1, K_2, K_3\}$. For example, it remains to test the proposed model in equibiaxial tension, in which $K_1 > 0$ and $K_3 = -1$ (cf., e.g., the simple compression, $K_1 < 0$ and $K_3 = -1$, or simple tension, $K_1 > 0$ and $K_3 = 1$, modes used in model calibration).

- Regarding the viscoelastic constitutive model, it remains to experimentally characterize and calibrate the model for the low and moderate density Poron XRD foams and to validate the viscoelastic constitutive model at elevated loading rates using the compression, shear, and tension-dominated cases employed to validate the hyperelastic model. Furthermore, we envision extending the viscoelastic constitutive model to the strain-rate range 10^0-$10^2\ \mathrm{s}^{-1}$.

- The polymeric matrix material of the foam may be temperature sensitive, in some cases dramatically so, and this effect may be coupled with the rate-sensitivity of the matrix material. All experiments in the present work were conducted under approximately isothermal conditions at room temperature. Accordingly, the model also assumes isothermal conditions, and the effect of variable temperature is not captured. To use the model at elevated or reduced temperature, a new set of experiments at the temperature of interest would be required. Preliminary data gathered in spherical indentation experiments at an equivalent nominal strain-rate of $5 \times 10^{-2}\ \mathrm{s}^{-1}$ – shown in Fig. 24 – illustrates the significant effect of ambient temperature on both the apparent stiffness as well as the dissipation, which can be seen in the amount of hysteresis, of foam materials. Of particular note is the large increase in apparent stiffness and hysteresis for temperatures below room temperature (21°C), as illustrated in the middle panel of Fig. 24. Similarly of note is the reduction in hysteresis and softening of the material at temperatures above room temperature.

- Finally, very-low-density elastomeric foam materials with a "reticulated" microstructure may exhibit strain localization into compaction bands under uniform external loading. The foam

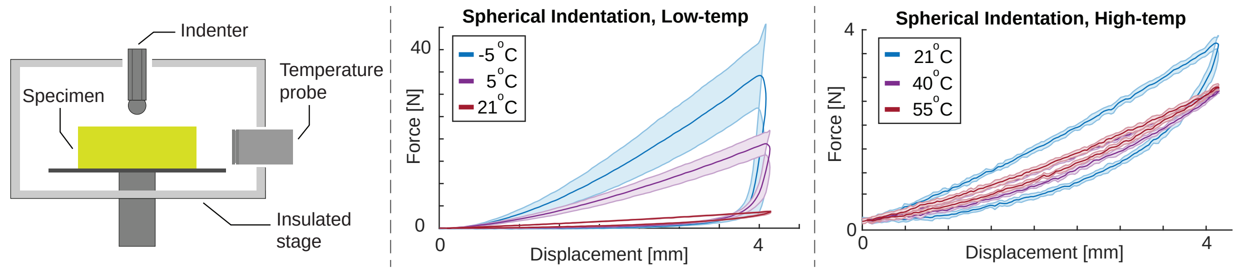

Figure 24: Preliminary spherical indentation data highlighting the important role of temperature on the mechanical response of polyurethane foams. Left panel depicts a schematic of the temperature-controlled indentation chamber. Middle and right panels show the measured indentation force versus displacement over a range of temperatures, illustrating a significant increase in the apparent stiffness and hysteresis of the response with decreasing temperature. All data is for the polyurethane-based Poron XRD foam of moderate (192.2 kg/m^3) density.

material considered in the present work did not exhibit localization, and localization behavior is not accounted for in the model. Developing a model that captures this behavior will be the subject of future work.

A Digital image correlation parameters and strain validation

The digital image correlation details for typical cases of each experimental DIC configuration used during a given experiment are provided in Table 4. Noise-floor resolution is defined as the standard deviation of the DIC displacement reconstructed from sequential, nominally zero-displacement images. Spatial resolution is estimated to be half of the minimum subset size.

To document the process of strain computation using a global plane fit, Fig. A.1(a) shows a fitting plane result with a comparison between the measured field and the noise floor for a typical experiment (specimen 2, experiment 2) on the low density foam for an incremental displacement between -0.261 and -0.266 global axial engineering strain. The zero-displacement noise floor for a single image in the pair, generated by adding Poisson noise (shot noise) and white Gaussian noise (0 mean, 0.75% variance, sensor noise) at a typical noise floor between deformed images, is of similar magnitude to the differences between the fitted plane and the experimental displacement measurement. For the same case, the spatial distribution of the locally-differentiated strain component – i.e., $e_{11}(x_1, x_2)$ – is presented in Fig. A.1(b) for both the zero-displacement noise and -0.266 global axial engineering strain cases. Strain was computed from cumulated displacements via an Optimal-9 differentiation kernel, per Bar-Kochba et al. (2015), and the virtual strain gauge size was 80 px (640 μm). The distribution of measured strain values is generally a single-peak Gaussian (see Fig. A.1(c)), revealing the underlying random nature of the spatial variance in strain (Wang and Cuitiño, 2002)

Specification	Simple compression	Simple tension	Shear without pre-compression	Shear with pre-compression	Tension with holes
Technique	Single Camera q-factor Based Digital Image Correlation				
Pre-filtering	Gaussian, [3px, 0.2]				
Min. Subset Size [px]	16				
Min. Step Size [px]	8				
Correlation criterion	Iterative FFT-based ZNCC				
Interpolation	Bicubic splines				
Camera noise [%]	0.30	0.25	0.25	0.25	0.25
Image size [px^2]	1200x350	800x1900	1300x1200	950x1200	1100x2000
Measurement points	6560	23750	24375	17813	34375
Number of images	260 (0.033 Hz)	250 (0.040 Hz)	180 (0.033 Hz)	200 (0.033 Hz)	235 (0.143 Hz)
Pixel-to-μm conversion	1px = 10μm	1px=8μm	1px=8μm	1px=8μm	1px = 8μm
Resolution: spatial (est.)	8px = 80μm	8px = 64μm	8px = 64μm	8px = 64μm	8px = 64μm
Resolution: noise [px]	0.05	0.0075	0.046	0.033	0.05

Table 4: Typical digital image correlation specification details for the experimental calibration and validation test cases. In most cases, values reported are from the high density, specimen 3, experiment 1 data and are typical.

B Material parameter estimation procedure

The constitutive model described in Section 7 involves 14 material parameters that are used to represent the hyperelastic behavior of non-localizing, open-cell elastomeric foams. This Appendix provides a heuristic procedure for estimating the values of these parameters for a generic elastomeric foam material. The procedure is illustrated by estimating the material parameters for the high density Poron XRD foam, using the experimental data from simple compression/tension experiments shown in Fig. 1(c).

The first step of the procedure is to determine the ground-state shear and bulk moduli, G_0 and B. The ground-state Young's modulus and Poisson's ratio are extracted from the experimental data via a linear least squares regression to the compression and tension experimental data in the axial engineering strain range of approximately -0.02 to 0.02 and used to calculate G_0 and B. For the high density foam, $G_0 = 102.0\,\text{kPa}$ and $B = 193.8\,\text{kPa}$. Second, the phenomenological functions $X(K_1)$, $L(K_2, K_3)$, and $f(K_1)$ are iteratively fit to data extracted from the axial stress and lateral strain versus axial strain data in simple compression, in which $K_3 = -1$ is fixed. The parameters used to fit the compression response consist of $\{X_1', K_1^0, \Delta_K, X_2'\}$ for $X(K_1)$, $\{C_0, p\}$ for $L(K_2, K_3)$, and $\{J_{min}, C_2, C_3, r\}$ for $f(K_1)$. Finally, the remaining parameters – namely, $\{C_1, q\}$ for $L(K_2, K_3)$ – are then estimated from the simple tension experimental data, in which $K_3 = 1$ is fixed. The

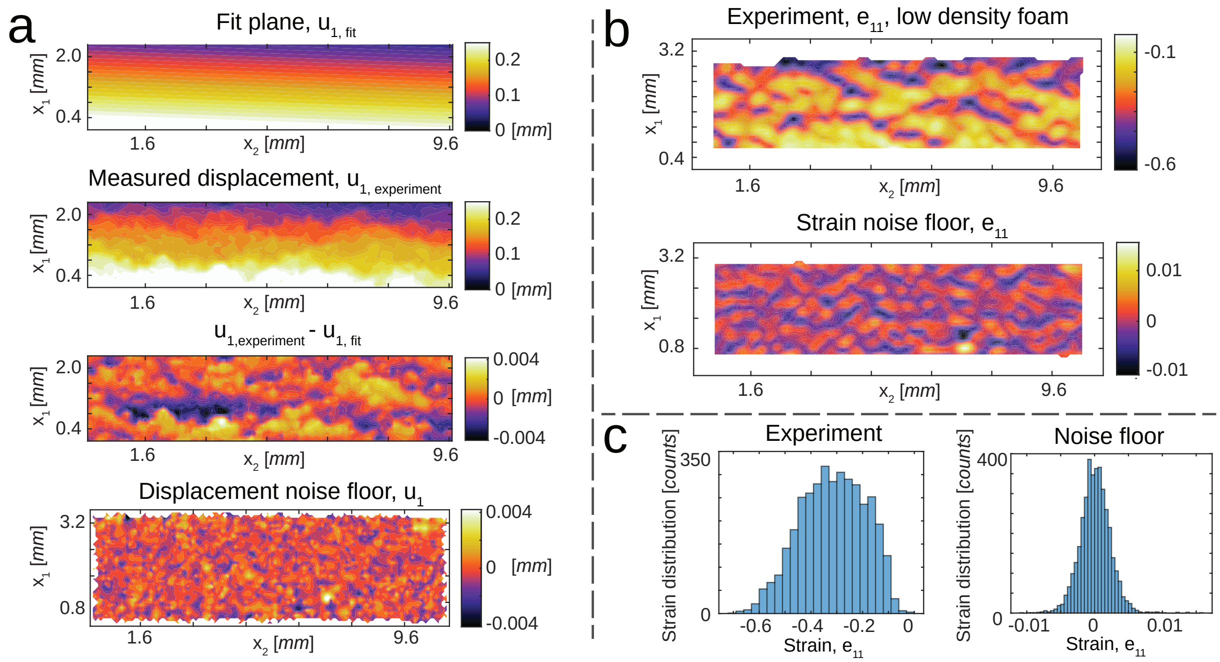

Figure A.1: Spatial distribution of displacement and strain for a typical low density foam at -0.26 global axial engineering strain. (a) Incremental displacement from -0.261 to -0.266 global axial engineering strain with the zero-displacement noise profile, demonstrating the deviation from the best fit plane is of similar magnitude as the noise floor. (b) Comparison between experimental strain distribution at -0.26 global axial engineering strain to the noise floor for strain measurement for the image pair. (c) Histogram of experimental and noise floor strain values, showing a broad, slightly skewed Gaussian-like distribution for the experiment with mean centered about the applied global axial engineering strain and a zero-mean Gaussian-like profile for the noise floor.

processes for estimating the compression-based and tension-based parameters are discussed in the following sections, and Figure A.2 outlines the steps in this workflow.

B.1 Estimation of compression-based parameters

In simple compression, the principal stretches are $\lambda_1 = \lambda_2 = \lambda_{\mathrm{lat}} > 1$ and $\lambda_3 = \lambda_{\mathrm{ax}} < 1$, and the logarithmic strain invariants are $K_1 = \ln(\lambda_{\mathrm{ax}}\lambda_{\mathrm{lat}}^2)$, $K_2 = (\sqrt{6}/3)\ln(\lambda_{\mathrm{lat}}/\lambda_{\mathrm{ax}})$, and $K_3 = -1$, so that the histories of K_1 and K_2 during compression may be determined from the kinematic measurements. The principal engineering stresses are $S_1 = S_2 = 0$ and $S_3 = S_{\mathrm{ax}} < 0$. Using (7.3) and the definition of the first Piola stress, $\mathbf{S} = J\mathbf{T}\mathbf{F}^{-\top}$, the components of the constitutive equation for the stress are

$$\begin{aligned} S_{\mathrm{ax}} &= \frac{1}{\lambda_{\mathrm{ax}}}\left[\left(G_0\frac{dX}{dK_1}K_2^2 + B\frac{df}{dK_1}\right) - \frac{2}{\sqrt{6}}G_0\left(2X(K_1)K_2 + \left.\frac{\partial L}{\partial K_2}\right|_{K_3=-1}\right)\right], \\ 0 &= \frac{1}{\lambda_{\mathrm{lat}}}\left[\left(G_0\frac{dX}{dK_1}K_2^2 + B\frac{df}{dK_1}\right) + \frac{1}{\sqrt{6}}G_0\left(2X(K_1)K_2 + \left.\frac{\partial L}{\partial K_2}\right|_{K_3=-1}\right)\right]. \end{aligned} \tag{B.1}$$

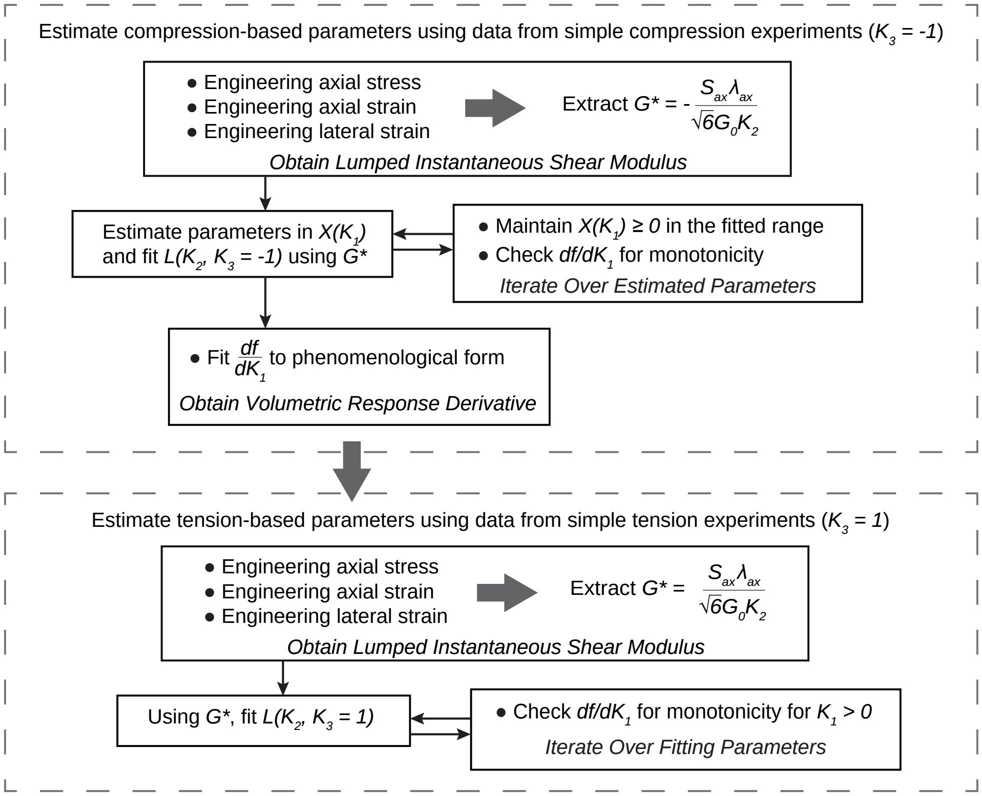

Figure A.2: Outline of the procedure for estimating material parameters from experimental data for simple compression and tension. Compression-based parameters are estimated first, followed by the estimation of tension-based parameters.

Next, combining $(B.1)_1$ and $(B.1)_2$ in order to eliminate df/dK_1 and rearranging, we obtain

$$G^* = X(K_1) + \frac{1}{2K_2}\left.\frac{\partial L}{\partial K_2}\right|_{K_3=-1} = -\frac{S_{\text{ax}}\lambda_{\text{ax}}}{\sqrt{6}G_0K_2}. \tag{B.2}$$

where G^* is a normalized lumped instantaneous shear modulus. All quantities on the right-hand-side of (B.2) – namely, the histories of S_{ax}, λ_{ax}, and K_2 during simple compression as well as the ground-state shear modulus G_0 – are known, so that (B.2) may be used to determine the history of G^* during simple compression, which may, in turn, be used to estimate the parameters appearing in $X(K_1)$ and $L(K_2, K_3)$. The measured G^* history during simple compression, projected onto the G^*-K_1-plane and the G^*-K_2-plane, is shown as solid lines in Figs. A.3(a) and (b), respectively. An iterative process is necessary to estimate the material parameters appearing in the $X(K_1)$ and $L(K_2, K_3 = -1)$ functions, while ensuring that – for the purpose of stability – a monotonically increasing fitting function for df/dK_1 may be used to capture data. A method for choosing an initial guess for the parameters appearing in $X(K_1)$ is as follows:

1. The parameter X_1' is the slope of $X(K_1)$ prior to the plateau regime in compression. The value of X_1' may be estimated from the slope of the projection of G^* versus K_1 at $K_1 = 0$, as illustrated in Fig. A.3(a).

2. The parameter K_1^0 is the value of K_1 denoting the transition to the plateau regime in $X(K_1)$. The value of K_1^0 may be estimated as the center of the K_1-range, in which the slope of G^* versus K_1 in the projection of Fig. A.3(a) changes rapidly during simple compression, as illustrated in Fig. A.3(a).

3. The parameter Δ_K is the width of the K_1-range across which the value of dX/dK_1 transitions from X_1' to X_2'. The value of Δ_K may be estimated from the width of the transition range in K_1 for G^* versus K_1 in the projection of Fig. A.3(a) during simple compression, as illustrated in Fig. A.3(a).

4. The parameter X_2' is the slope of $X(K_1)$ after the onset of the plateau regime in compression. The value of X_2' is estimated to be small compared to X_1' – i.e., $X_2' \sim O(X_1'/10)$. For the purpose of stability, it is important that the choice of this parameter results in $X(K_1) > 0$ over the entire fitted range of K_1.

Guided by Fig. A.3(a), we estimate the material parameters appearing in the $X(K_1)$ function to be $X_1' = 3.7$, $K_1^0 = -0.21$, $\Delta_K = 0.2$, and $X_2' = 0.22$ for the Poron XRD foam material.

Once the parameters of the $X(K_1)$ function are estimated, the next step is to estimate the parameters of the $L(K_2, K_3 = -1)$ function, namely, C_0 and p. Rearranging (B.2), we obtain

$$\left.\frac{\partial L}{\partial K_2}\right|_{K_3=-1} = 2K_2\left(-\frac{S_{\rm ax}\lambda_{\rm ax}}{\sqrt{6}G_0K_2} - X(K_1)\right). \tag{B.3}$$

Using the measured data and the previously-estimated parameters, (B.3) may be used to determine C_0 and p, which we have estimated to be $C_0 = 0.1$ and $p = 4$ for the Poron XRD foam material. Projections of the fitted G^* history during simple compression, i.e., $G^* = X(K_1) + (1/(2K_2))\partial L/\partial K_2|_{K_3=-1}$, using the estimated material parameters are shown as dashed lines in Figs. A.3(a) and (b).

With initial estimates for X_1', K_1^0, Δ_K, X_2', C_0, and p in hand, we check that a monotonically increasing fitting function for df/dK_1 may be used to capture data. Rearranging $(B.1)_2$, we obtain the following expression for df/dK_1:

$$\frac{df}{dK_1} = -\frac{G_0}{B}\left[\frac{1}{\sqrt{6}}\left(2X(K_1)K_2 + \left.\frac{\partial L}{\partial K_2}\right|_{K_3=-1}\right) + \frac{dX}{dK_1}K_2^2\right]. \tag{B.4}$$

Again, all quantities on the right-hand-side of (B.4) are either measured data or previously-fitted parameters and are therefore known. The df/dK_1 history during simple compression (B.4) is shown as a solid line in Fig. A.3(c), using the previously-estimated parameters. This history is non-monotonic[13] but may be reasonably captured by a monotonically-increasing fitting function. If the df/dK_1 history is too non-monotonic, the material parameters of the $X(K_1)$ function should be adjusted. Typically, the parameter X_1' should be decreased from its initial estimated value, and the parameter X_2' should be increased – all while ensuring that $X(K_1) \geq 0$ over the fitted K_1-range. Then, the $L(K_2, K_3 = -1)$ function is refit, and the resulting df/dK_1 history may be checked again for near-monotonicity. In this way, the material parameters of the $X(K_1)$ function are iteratively

[13]We note that the non-monotonic behavior in the df/dK_1 history of Fig. A.3(c) arises due to the presence of the shear-induced mean stress term, $(dX/dK_1)K_2^2$, in (B.4).

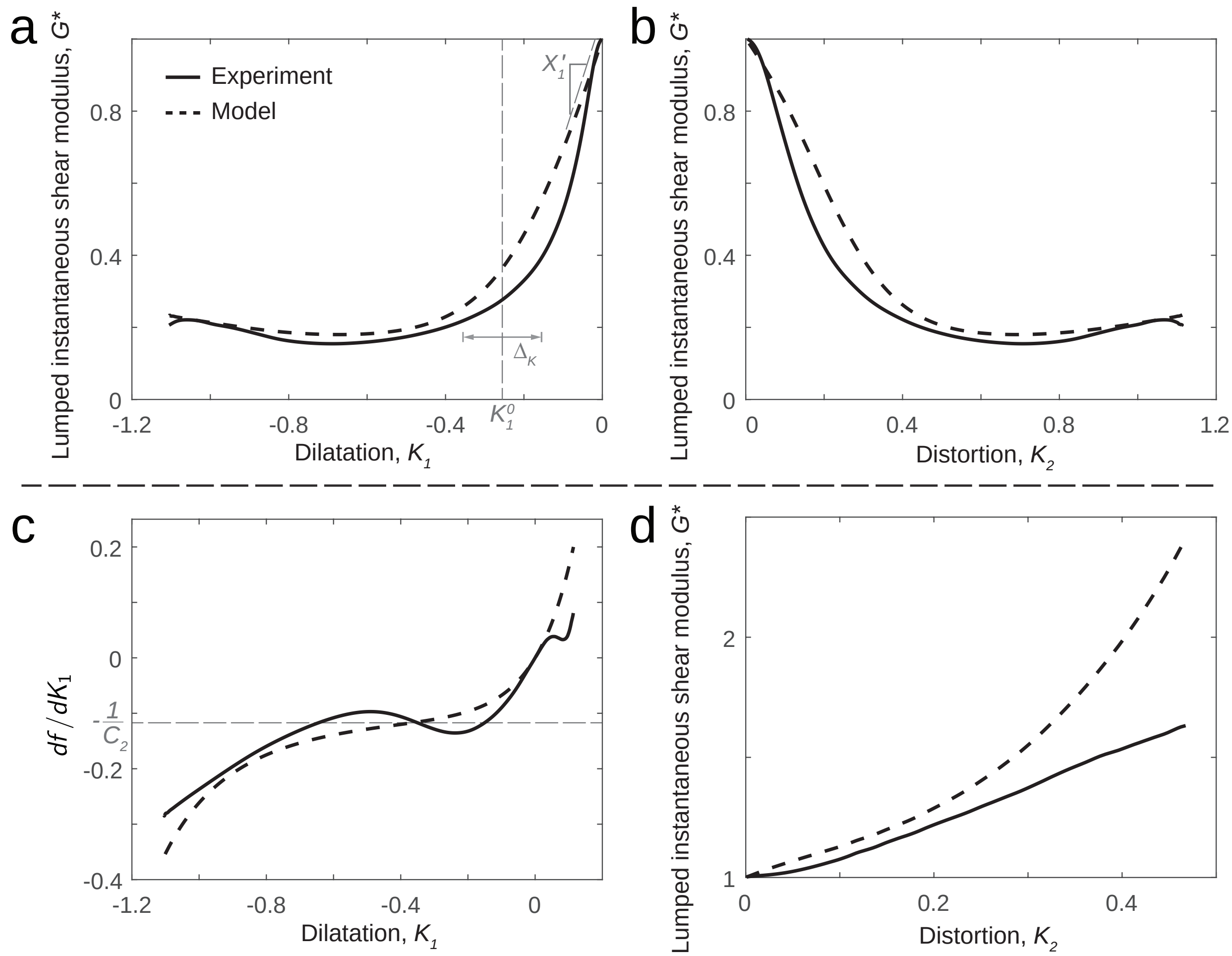

Figure A.3: Projections of the normalized lumped instantaneous shear modulus, G^*, plotted as a function of (a) the dilatation, K_1, and (b) the distortion, K_2, for a simple compression loading history ($K_3 = -1$). (c) The first derivative of the volumetric response function $f(K_1)$ with respect to K_1, df/dK_1, plotted as a function of K_1. (d) Projection of the normalized lumped instantaneous shear modulus, G^*, plotted as a function of the distortion, K_2, for a simple tension loading history ($K_3 = 1$). Solid lines denote experimental data for the high density Poron XRD foam material; dashed lines denote the model fit; and interpretations of the material parameters X_1', K_1^0, Δ_K, and C_2 are illustrated.

adjusted until the df/dK_1 history may be reasonably captured by a monotonically-increasing fitting function. Once this is achieved, the parameters $J_{\min}$, C_2, C_3, and r may be estimated. The parameter $J_{\min}$ represents the minimum allowable value of J and may be interpreted as $J_{\min} = 1-\phi_0$, where ϕ_0 is the void volume fraction. Therefore, $\ln J_{\min}$ is the minimum allowable value of K_1, and df/dK_1 diverges as $K_1 \to \ln J_{\min}$. The parameter C_2 sets the value of df/dK_1 in the plateau region. More specifically, the value of df/dK_1 in the plateau region is slightly more negative than $(-1/C_2)$, as illustrated in Fig. A.3(c). Finally, the parameters C_3 and r are adjustable parameters that may be chosen so that the model response matches the stiffening behavior after the plateau regime. The values of the parameters for the high density Poron XRD foam material, determined using this procedure, are $J_{\min} = 0.19$, $C_2 = 9$, $C_3 = 0.026$, and $r = 2$, and the fitted df/dK_1 function is plotted as a dashed line in Fig. A.3(c).[14]

B.2 Estimation of tension-based parameters

Once the response in simple compression has been fit, experimental data from simple tension is used to estimate the remaining parameters in the $L(K_2, K_3)$ function, namely, C_1 and q. As in the material parameter estimation procedure described above for simple compression, estimating these parameters is an iterative process, since it must be ensured that df/dK_1 may be reasonably captured by a monotonically-increasing fitting function over the positive K_1-range of application. In simple tension, the principal stretches are $\lambda_1 = \lambda_{\mathrm{ax}} > 1$ and $\lambda_2 = \lambda_3 = \lambda_{\mathrm{lat}} < 1$; the logarithmic strain invariants are $K_1 = \ln(\lambda_{\mathrm{ax}}\lambda_{\mathrm{lat}}^2)$, $K_2 = (\sqrt{6}/3)\ln(\lambda_{\mathrm{ax}}/\lambda_{\mathrm{lat}})$, and $K_3 = 1$; and the principal engineering stresses are $S_1 = S_{\mathrm{ax}} > 0$ and $S_2 = S_3 = 0$. The components of the constitutive equation for the stress are then

$$\begin{aligned} S_{\mathrm{ax}} &= \frac{1}{\lambda_{\mathrm{ax}}}\left[\left(G_0\frac{dX}{dK_1}K_2^2 + B\frac{df}{dK_1}\right) + \frac{2}{\sqrt{6}}G_0\left(2X(K_1)K_2 + \left.\frac{\partial L}{\partial K_2}\right|_{K_3=1}\right)\right], \\ 0 &= \frac{1}{\lambda_{\mathrm{lat}}}\left[\left(G_0\frac{dX}{dK_1}K_2^2 + B\frac{df}{dK_1}\right) - \frac{1}{\sqrt{6}}G_0\left(2X(K_1)K_2 + \left.\frac{\partial L}{\partial K_2}\right|_{K_3=1}\right)\right], \end{aligned} \tag{B.5}$$

and combining $(\mathrm{B.5})_1$ and $(\mathrm{B.5})_2$ in order to eliminate df/dK_1 and rearranging, we obtain the normalized lumped instantaneous shear modulus, G^*, in tension:

$$G^* = X(K_1) + \frac{1}{2K_2}\left.\frac{\partial L}{\partial K_2}\right|_{K_3=1} = \frac{S_{\mathrm{ax}}\lambda_{\mathrm{ax}}}{\sqrt{6}G_0K_2}, \tag{B.6}$$

which may be rearranged as

$$\left.\frac{\partial L}{\partial K_2}\right|_{K_3=1} = 2K_2\left(\frac{S_{\mathrm{ax}}\lambda_{\mathrm{ax}}}{\sqrt{6}G_0K_2} - X(K_1)\right). \tag{B.7}$$

Using the measured data and previously-estimated parameters, (B.7) may be used to estimate the remaining two parameters appearing in the $L(K_2, K_3 = 1)$ function, C_1 and q. Then, rearranging $(\mathrm{B.5})_2$, we obtain the following expression for df/dK_1 during simple tension:

$$\frac{df}{dK_1} = \frac{G_0}{B}\left[\frac{1}{\sqrt{6}}\left(2X(K_1)K_2 + \left.\frac{\partial L}{\partial K_2}\right|_{K_3=1}\right) - \frac{dX}{dK_1}K_2^2\right]. \tag{B.8}$$

Using the estimated values for the parameters C_1 and q, (B.8) is used to check that the df/dK_1 history is nearly-monotonic for $K_1 > 0$. If this is not the case, the value of C_1 should be increased

[14] We note that the material parameter estimation procedure described in this section ensures that the fitted engineering stress versus axial engineering strain response remains monotonic in simple compression in order to maximize stable behavior. However, the model fit to the lateral engineering strain versus axial engineering strain response can be slightly non-monotonic (see Fig. 1). Since non-monotonicity in the lateral strain response does not affect stability, and since the oscillations in the lateral strain response are on the order of 0.01 whereas the axial strain varies over an order of 0.1, we do not prioritize the elimination of the relatively low amplitude oscillations in the fitted lateral strain response in the present work.

from its initial estimated value. If it is necessary to substantially increase C_1 to obtain a monotonic df/dK_1 history for $K_1 > 0$, so that the G^* history from simple tension is significantly overestimated, the estimation of the compression-based parameters should be repeated using a reduced value for X_1', and in this way, the parameters are iteratively adjusted until the df/dK_1 history is nearly monotonic. Using this process, we estimate the parameters for the high density Poron XRD foam material to be $C_1 = 1.9$ and $q = 5$, and the resulting fitted G^* history during simple tension, projected in the G^*-K_2-plane, is shown in Fig. A.3(d) as a dashed line, along with the measured G^* history as a solid line. It is evident that a compromise is made in which G^* is overestimated in simple tension in order to obtain a suitable df/dK_1 history.

C Loss of ellipticity

In this appendix, we provide background for the loss of ellipticity analysis utilized in Section 9.1. We consider a time-dependent, incremental process superimposed upon a time-independent base state of deformation (Ogden, 1984). The base state is described by a motion field $\boldsymbol{\chi}(\mathbf{x})$, which satisfies the governing equations. Then, denoting small increments with a superposed dot, the incremental displacement field is expressed referentially as $\dot{\mathbf{u}}(\mathbf{x}, t)$ or, alternatively, expressed spatially as $\dot{\mathbf{u}}(\boldsymbol{\chi}^{-1}(\mathbf{y}), t)$. The associated incremental deformation gradient and incremental spatial displacement gradient fields are $\dot{\mathbf{F}} = \nabla\dot{\mathbf{u}}$ and $\dot{\mathbf{H}} = \operatorname{grad}\dot{\mathbf{u}} = \dot{\mathbf{F}}\mathbf{F}^{-1}$, respectively. The first Piola stress in the base state is given by $\mathbf{S} = J\mathbf{T}\mathbf{F}^{-\top} = \partial\psi/\partial\mathbf{F}$, and the increments in the first Piola stress are obtained by linearizing this constitutive equation: $\dot{\mathbf{S}} = \mathbb{C}_{\mathrm{R}}\dot{\mathbf{F}}$, where $\mathbb{C}_{\mathrm{R}} = \partial^2\psi/\partial\mathbf{F}\partial\mathbf{F}$ are the material moduli, evaluated in the base state. The stress increments, pushed forward to the deformed body, are given by $\dot{\mathbf{T}} = J^{-1}\dot{\mathbf{S}}\mathbf{F}^{\top} = \mathbb{C}\dot{\mathbf{H}}$, where

$$\mathbb{C}_{ijkl}(\mathbf{y}) = J^{-1}F_{jn}F_{lq}\frac{\partial^2\psi}{\partial F_{in}\partial F_{kq}}, \tag{C.1}$$

are the spatial moduli, evaluated at the base state. The incremental form of the equations of motion are

$$\operatorname{div}\dot{\mathbf{T}} = \operatorname{div}(\mathbb{C}\dot{\mathbf{H}}) = \rho\frac{\partial^2\dot{\mathbf{u}}}{\partial t^2}, \tag{C.2}$$

where $\rho = J^{-1}\rho_{\mathrm{R}}$ is the spatial mass density, ρ_{R} is the referential mass density, and $\partial(\bullet)/\partial t$ is the spatial time derivative. Straightforward application of the chain rule leads to the following expression for the spatial tangents:

$$\mathbb{C}_{ijkl} = \frac{1}{2J}\mathbb{D}_{ijmn}\mathbb{L}_{mnpq}\mathbb{B}_{pqkl} - T_{il}\delta_{jk} \tag{C.3}$$

with

$$\mathbb{D} = \frac{\partial\mathbf{T}_{\mathrm{K}}}{\partial\mathbf{E}}, \quad \mathbb{L} = \frac{\partial\ln(\mathbf{B})}{\partial\mathbf{B}}, \quad \text{and} \quad \mathbb{B}_{ijkl} = \delta_{ik}B_{jl} + \delta_{jk}B_{il}, \tag{C.4}$$

where $\mathbf{T}_{\mathrm{K}} = J\mathbf{T}$ is the Kirchhoff stress. For a free-energy function based on logarithmic strain invariants, $\tilde{\psi}(K_1, K_2, K_3)$, straightforward calculations involving the chain rule lead to the following expression for the constitutive contribution to the spatial tangents:

$$
\begin{aligned}
\mathbb{D}_{ijkl} = \frac{\partial T_{\mathrm{K},ij}}{\partial E_{kl}} = & \frac{\partial^2\tilde{\psi}}{\partial K_1^2}\delta_{ij}\delta_{kl} + \left(\frac{\partial^2\tilde{\psi}}{\partial K_2^2} - \frac{\partial\tilde{\psi}}{\partial K_2}\frac{1}{K_2} - \frac{\partial\tilde{\psi}}{\partial K_3}\frac{3K_3}{K_2^2}\right)N_{ij}N_{kl} + \frac{\partial^2\tilde{\psi}}{\partial K_3^2}\frac{1}{K_2^2}Y_{ij}Y_{kl} \\
& + \left(\frac{\partial^2\tilde{\psi}}{\partial K_1 \partial K_2} - 2\sqrt{6}\frac{\partial\tilde{\psi}}{\partial K_3}\frac{1}{K_2^2}\right)\left(\delta_{ij}N_{kl} + N_{ij}\delta_{kl}\right) \\
& + \frac{\partial^2\tilde{\psi}}{\partial K_1 \partial K_3}\frac{1}{K_2}\left(\delta_{ij}Y_{kl} + Y_{ij}\delta_{kl}\right) \\
& + \left(\frac{\partial^2\tilde{\psi}}{\partial K_2 \partial K_3}\frac{1}{K_2} - 3\frac{\partial\tilde{\psi}}{\partial K_3}\frac{1}{K_2^2}\right)\left(N_{ij}Y_{kl} + Y_{ij}N_{kl}\right) \\
& + \left(\frac{\partial\tilde{\psi}}{\partial K_2}\frac{1}{K_2} - \frac{\partial\tilde{\psi}}{\partial K_3}\frac{3K_3}{K_2^2}\right)\left(\mathbb{I}_{ijkl} - \frac{1}{3}\delta_{ij}\delta_{kl}\right) \\
& + \frac{3\sqrt{6}}{2}\frac{\partial\tilde{\psi}}{\partial K_3}\frac{1}{K_2^2}\left(\delta_{ik}N_{jl} + \delta_{il}N_{jk} + N_{ik}\delta_{jl} + N_{il}\delta_{jk}\right).
\end{aligned}
\tag{C.5}
$$

Then, we consider a homogeneous base state of deformation in an infinite domain – so that the base-state motion field χ varies linearly in $\mathbf{x}$, and the base-state deformation gradient $\mathbf{F}$, spatial logarithmic strain tensor $\mathbf{E}$, and spatial moduli $\mathbb{C}$ are all spatially constant – and consider solutions for the incremental displacement field in the following form:

$$
\dot{\mathbf{u}} = \hat{\mathbf{u}}\, g(k(\mathbf{n}\cdot\mathbf{y} - ct)), \tag{C.6}
$$

where $k\mathbf{n}$ is a wave vector, k is the wave-vector magnitude, $\mathbf{n}$ is the unit vector along the direction of the wave vector, c is the wave speed, $\hat{\mathbf{u}}$ is the amplitude of the incremental displacement, and g is a continuous and sufficiently differentiable (but otherwise arbitrary) function. Upon substituting (C.6) into (C.2), we obtain the following eigenvalue problem: $\mathbf{Q}(\mathbf{n})\hat{\mathbf{u}} = \rho c^2\hat{\mathbf{u}}$ with eigenvalues ρc^2 and eigenvectors $\hat{\mathbf{u}}$, where $Q_{ik}(\mathbf{n}) = \mathbb{C}_{ijkl}n_j n_l$ is the acoustic tensor in the deformed configuration for a unit vector $\mathbf{n}$, which is utilized to assess stability in Section 9.1.

References

Abaqus (2018). Reference manuals. Dassault Systèmes Simulia Corp.

Anand, L. (1979). On H. Hencky's approximate strain-energy function for moderate deformations. *Journal of Applied Mechanics 46*, 78–82.

Anand, L. (1986). Moderate deformations in extension-torsion of incompressible isotropic elastic materials. *Journal of the Mechanics and Physics of Solids 34*, 293–304.

Anand, L., N. M. Ames, V. Srivastava, and S. A. Chester (2009). A thermo-mechanically coupled theory for large deformations of amorphous polymers. part i: Formulation. *International Journal of Plasticity 25*, 1474–1494.

Anani, Y. and Y. Alizadeh (2011). Visco-hyperelastic constitutive law for modeling of foam's behavior. *Materials and Design 32*, 2940–2948.

Bar-Kochba, E., J. Toyjanova, E. Andrews, K. Kim, and C. Franck (2015). A fast iterative digital volume correlation algorithm for large deformations. *Experimental Mechanics 55*, 261–274.

Bay, B. K. (2008). Methods and applications of digital volume correlation. *The Journal of Strain Analysis for Engineering Design 43*, 745–760.

Bay, B. K., T. S. Smith, D. P. Fyhrie, and M. Saad (1999). Digital volume correlation: three-dimensional strain mapping using x-ray tomography. *Experimental mechanics 39*, 217–226.

Bergström, J. (2006). Advanced finite element modeling of polymer foam components. In *Proceedings of the ABAQUS Users' Conference*, pp. 81–94.

Bergström, J. and M. C. Boyce (1998). Constitutive modeling of the large strain time-dependent behavior of elastomers. *Journal of the Mechanics and Physics of Solids 46*, 931–954.

Bigoni, D. (2012). *Nonlinear solid mechanics: bifurcation theory and material instability*. Cambridge University Press.

Blaber, J., B. Adair, and A. Antoniou (2015). Ncorr: Open-source 2d digital image correlation matlab software. *Experimental Mechanics 55*, 1105–1122.

Blatz, P. J. and W. L. Ko (1962). Application of finite elastic theory to the deformation of rubbery materials. *Transactions of the Society of Rheology 6*, 223–251.

Bossuyt, S. (2013). *Optimized Patterns for Digital Image Correlation*, pp. 239–248. New York, NY: Springer New York.

Briody, C., B. Duignan, S. Jerrams, and J. Tiernan (2012). The implementation of a visco-hyperelastic numerical material model for simulating the behaviour of polymer foam materials. *Computational Material Science 64*, 47–51.

Brydon, A. D., S. G. Bardenhagen, E. A. Miller, and G. T. Seidler (2005). Simulation of the densification of real open-celled foam microstructures. *Journal of the Mechanics and Physics of Solids 53*, 2638–2660.

Charonko, J. J. and P. P. Vlachos (2013). Estimation of uncertainty bounds for individual particle image velocimetry measurements from cross-correlation peak ratio. *Measurement Science and Technology 24*, 065301.

Chen, W., Z. Lu, B. Pan, J. Guo, and Y. Li (2012). Nonlinear behavior of bumper foams under uniaxial compressive cyclic loading. *Materials and Design 35*, 491–497.

Chen, Y., W. Guo, P. Yang, J. Zhao, Z. Guo, L. Dong, and Z. Zhong (2018). Constitutive modeling of neo-hookean materials with spherical voids in finite deformation. *Extreme Mechanics Letters 24*, 47–57.

Chester, S. A. (2012). A constitutive model for coupled fluid permeation and large viscoelastic deformation in polymeric gels. *Soft Matter 8*, 8223–8233.

Chu, T. C., W. F. Ranson, and M. A. Sutton (1985). Applications of digital-image-correlation techniques to experimental mechanics. *Experimental Mechanics 25*, 232–244.

Ciambella, J. and G. Saccomandi (2014). A continuum hyperelastic model for auxetic materials. *Proceeding of the Royal Society of London A 470*, 20130691.

Crammond, G., S. Boyd, and J. Dulieu-Barton (2013). Speckle pattern quality assessment for digital image correlation. *Optics and Lasers in Engineering 51*, 1368–1378.

Criscione, J. C. (2004). Rivlin's representation formula is ill-conceived for the determination of response functions via biaxial testing. In *The Rational Spirit in Modern Continuum Mechanics*, pp. 197–215. Springer.

Criscione, J. C., J. D. Humphrey, A. S. Douglas, and W. C. Hunter (2000). An invariant basis for natural strain which yields orthogonal stress response terms in isotropic hyperelasticity. *Journal of the Mechanics and Physics of Solids 48*, 2445–2465.

Dacorogna, B. (2001). Necessary and sufficient conditions for strong ellipticity of isotropic functions in any dimension. *Discrete And Continuous Dynamical Systems, Series B 1*, 257–263.

Danielsson, M., D. M. Parks, and M. C. Boyce (2004). Constitutive modeling of porous hyperelastic materials. *Mechanics of Materials 36*, 347–258.

Deshpande, V. S. and N. A. Fleck (2001). Multi-axial yield behaviour of polymer foams. *Acta Materialia 49*, 1859–1866.

Diani, J. and P. Gilormini (2005). Combining the logarithmic strain and the full-network model for a better understanding of the hyperelastic behavior of rubber-like materials. *Journal of the Mechanics and Physics of Solids 53*, 2579–2596.

Dong, Y. and B. Pan (2017). A review of speckle pattern fabrication and assessment for digital image correlation. *Experimental Mechanics 57*, 1161–1181.

Dupaix, R. B. and M. C. Boyce (2007). Constitutive modeling of the finite strain behavior of amorphous polymers in and above the glass transition. *Mechanics of Materials 39*, 39–52.

Elliott, J. A., A. H. Windle, J. R. Hobdell, G. Eeckhaut, R. J. Oldman, W. Ludwig, E. Boller, P. Cloetens, and J. Baruchel (2002). *In-situ* deformation of an open-cell flexible polyurethane foam characterised by 3d computed microtomography. *Journal of Materials Science 37*, 1547–1555.

Estrada, J. B. and C. Franck (2015). Intuitive interface for the quantitative evaluation of speckle patterns for use in digital image and volume correlation techniques. *Journal of applied mechanics 82*, 095001.

Franck, C., S. Hong, S. A. Maskarinec, D. A. Tirrell, and G. Ravichandran (2007). Three-dimensional full-field measurements of large deformations in soft materials using confocal microscopy and digital volume correlation. *Experimental Mechanics 47*, 427–438.

Fu, J., P. F., and R. P. D. (2013). Elastic stiffness characterization using three-dimensional full-field deformation obtained with optical coherence tomography and digital volume correlation. *Journal of Biomedical Optics 18*, 18–18–16.

Gibson, L. J. and M. F. Ashby (1997). *Cellular solids: structures and properties, 2nd edn.* Cambridge University Press.

Gong, L. and S. Kyriakides (2005). Compressive response of open cell foams. part ii: Initiation and evolution of crushing. *International Journal of Solids and Structures 42*, 1381–1399.

Gong, L., S. Kyriakides, and W. Jang (2005). Compressive response of open-cell foams. part i: Morphology and elastic properties. *International Journal of Solids and Structures 42*, 1355–1379.

Guo, Z., F. Caner, X. Peng, and B. Moran (2008). On constitutive modelling of porous neo-hookean composites. *Journal of the Mechanics and Physics of Solids 56*, 2338–2357.

Hencky, H. (1931). The law of elasticity for isotropic and quasi-isotropic substances by finite deformations. *Journal of Rheology 2*, 169–176.

Hencky, H. (1933). The elastic behavior of vulcanised rubber. *Rubber Chemistry and Technology 6*, 217–224.

Hild, F. and S. Roux (2012). Comparison of local and global approaches to digital image correlation. *Experimental Mechanics 52*, 1503–1519.

Hill, R. (1962). Acceleration waves in solids. *Journal of the Mechanics and Physics of Solids 10*, 1–16.

Hilyard, N. C. and A. Cunningham (1994). *Low Density Cellular Plastics: Physical Basis of Behavior*. Chapman & Hall.

Horgan, C. O. and J. G. Murphy (2009). A generalization of Hencky's strain-energy density to model the large deformations of slightly compressible solid rubbers. *Mechanics of Materials 41*, 943–950.

Horner, J. L. and J. R. Leger (1985). Pattern recognition with binary phase-only filters. *Applied Optics 24*, 609–611.

Hua, T., H. Xie, S. Wang, Z. Hu, P. Chen, and Q. Zhang (2011). Evaluation of the quality of a speckle pattern in the digital image correlation method by mean subset fluctuation. *Optics and Laser Technology 43*, 9–13.

Jambunathan, K., X. Y. Ju, B. N. Dobbins, and S. Ashforth-Frost (1995). An improved cross correlation technique for particle image velocimetry. *Measurement Science and Technology 6*, 507.

Javidi, B. (1989). Nonlinear joint power spectrum based optical correlation. *Applied Optics 28*, 2358–2367.

Jemiolo, S. and S. Turteltaub (2000). Parametric model for a class of foam-like isotropic hyperelastic materials. *Journal of Applied Mechanics 67*, 248–254.

Ju, M. L., H. Jmal, R. Dupuis, and E. Aubry (2015). Visco-hyperelastic constitutive model for modeling the quasi-static behavior of polyurethane foam in large deformation. *Polymer Engineering and Science 55*, 1795–1804.

Ju, M. L., S. Mezghani, H. Jmal, R. Dupuis, and E. Aubry (2013). Parameter estimation of a hyperelastic constitutive model for the description of polyurethane foam in large deformation. *Cellular Polymers 32*, 21–40.

Kakavas, P. A. (2000). A new development of the strain energy function for hyperelastic materials using a logarithmic strain approach. *Journal of Applied Polymer Science 77*, 660–672.

Kröner, E. (1960). Allgemeine kontinuumstheorie der versetzungen und eigenspannungen. *Archive for Rational Mechanics and Analysis 4*, 273–334.

Kumar, B. V. K. V. and L. Hassebrook (1990). Performance measures for correlation filters. *Applied Optics 29*, 2997–3006.

Lakes, R., P. Rosakis, and A. Ruina (1993). Microbuckling instability in elastomeric cellular solids. *Journal of Materials Science 28*, 4667–4672.

Landauer, A. K., X. Li, C. Franck, and D. L. Henann (2019). Experimental characterization and hyperelastic constitutive modeling of open-cell elastomeric foams. *Journal of the Mechanics and Physics of Solids*, in press, doi:10.1016/j.jmps.2019.103701.

Landauer, A. K., M. Patel, D. L. Henann, and C. Franck (2018). A q-factor-based digital image correlation algorithm (qDIC) for resolving finite deformations with degenerate speckle patterns. *Experimental Mechanics 58*, 815–830.

Lecompte, D., A. Smits, S. Bossuyt, H. Sol, J. Vantomme, D. V. Hemelrijck, and A. Habraken (2006). Quality assessment of speckle patterns for digital image correlation. *Optics and Lasers in Engineering 44*, 1132–1145.

Lee, E. H. (1969). Elastic plastic deformation at finite strain. *Journal of Applied Mechanics 36*, 1–6.

LePage, W. S., S. H. Daly, and J. A. Shaw (2016). Cross polarization for improved digital image correlation. *Experimental Mechanics 56*, 969–985.

Lewis, J. P. (1995). Fast normalized cross-correlation. In *Vision interface*, Volume 10, pp. 120–123.

Liu, Q. and G. Subhash (2004). A phenomenological constitutive model for foams under large deformations. *Polymer Engineering and Science 44*, 463–473.

Liu, X. Y., R. L. Li, H. W. Zhao, T. H. Cheng, G. J. Cui, Q. C. Tan, and G. W. Meng (2015). Quality assessment of speckle patterns for digital image correlation by shannon entropy. *Optik–International Journal for Light and Electron Optics 126*, 4206–4211.

Lopez-Pamies, O. and P. Ponte Castañeda (2007a). Homogenization-based constitutive models for porous elastomers and implications for microscopic instabilities: I – analysis. *Journal of the Mechanics and Physics of Solids 55*, 1677–1701.

Lopez-Pamies, O. and P. Ponte Castañeda (2007b). Homogenization-based constitutive models for porous elastomers and implications for microscopic instabilities: II – results. *Journal of the Mechanics and Physics of Solids 55*, 1702–1728.

Luo, P. F., Y. J. Chao, M. A. Sutton, and W. H. Peters (1993). Accurate measurement of three-dimensional deformations in deformable and rigid bodies using computer vision. *Experimental Mechanics 33*, 123–132.

Michell, J. H. (1899). On the direct determination of stress in an elastic solid, with application to the theory of plates. *Proceedings of the London Mathematical Society s1-31*, 100–124.

Mills, N. J. and A. Gilchrist (2000). Modelling the indentation of low density polymer foams. *Cellular Polymers 19*, 389–412.

Mulliken, A. D. and M. C. Boyce (2006). Mechanics of the rate-dependent elastic-plastic deformation of glassy polymers from low to high strain rates. *International Journal of Solids and Structures 43*, 1331–1356.

Murphy, J. G. (2000). Strain energy function for a poisson power law function in simple tension of compressible hyperelastic materials. *Journal of Elasticity 60*, 151–164.

Neilsen, M. K., R. D. Krieg, and H. L. Schreyer (1995). A constitutive theory for rigid polyurethane foam. *Polymer Engineering and Science 35*, 387–394.

Nogueira, J., A. Lecuona, P. A. Rodríguez, J. A. Alfaro, and A. Acosta (2005). Limits on the resolution of correlation piv iterative methods. practical implementation and design of weighting functions. *Experiments in Fluids 39*, 314–321.

Ogden, R. (1984). *Non-Linear Elastic Deformation*. Dover Publications.

Ogden, R. W. (1972a). Large deformation isotropic elasticity: On the correlation of theory and experiment for compressible rubberlike solids. *Proceedings of the Royal Society of London. Series A, Mathematical and Physical Sciences 328*, 567–583.

Ogden, R. W. (1972b). Large deformation isotropic elasticity: On the correlation of theory and experiment for incompressible rubberlike solids. *Proceedings of the Royal Society of London. Series A, Mathematical and Physical Sciences 326*, 565–584.

Pan, B., Z. Lu, and H. Xie (2010). Mean intensity gradient: an effective global parameter for quality assessment of the speckle patterns used in digital image correlation. *Optics and Lasers in Engineering 48*, 469–477.

Pan, B., D. Wu, and Y. Xia (2012). Incremental calculation for large deformation measurement using reliability-guided digital image correlation. *Optics and Lasers in Engineering 50*, 586–592.

Pan, B., H. Xie, Z. Wang, K. Qian, and Z. Wang (2008). Study on subset size selection in digital image correlation for speckle patterns. *Optics Express 16*, 7037–7048.

Petre, M. T., A. Erdemir, and P. R. Cavanagh (2006). Determination of elastomeric foam parameters for simulations of complex loading. *Computer Methods in Biomechanics and Biomedical Engineering 9*, 231–242.

Pierron, F., S. A. McDonald, D. Hollis, P. Withers, and A. Alderson (2011). Assessment of the deformation of low density polymeric auxetic foams by x-ray tomography and digital volume correlation. In *Applied Mechanics and Materials*, Volume 70, pp. 93–98. Trans Tech Publications.

Reese, S. and S. Govindjee (1998). A theory of finite viscoelasticity and numerical aspects. *International Journal of Solids and Structures 35*, 3455–3482.

Reu, P. (2013). A study of the influence of calibration uncertainty on the global uncertainty for digital image correlation using a monte carlo approach. *Experimental Mechanics 53*, 1661–1680.

Sabuwala, T. and G. Gioia (2013). Skeleton-and-bubble model of polyether-polyurethane elastic open-cell foams for finite element analysis at large deformations. *Journal of the Mechanics and Physics of Solids 61*, 886–911.

Scarano, F. (2002). Iterative image deformation methods in piv. *Measurement Science and Technology 13*, R1.

Schreier, H., J.-J. Orteu, and M. A. Sutton (2009). *Image correlation for shape, motion and deformation measurements*. Springer US.

Schrijer, F. F. J. and F. Scarano (2008). Effect of predictor–corrector filtering on the stability and spatial resolution of iterative piv interrogation. *Experiments in Fluids 45*, 927–941.

Shannon, C. (1948). A mathematical theory of communication. *Bell System Technical Journal 27*, 379–423.

Shrimali, B., V. Lefèvre, and O. Lopez-Pamies (2019). A simple explicit homogenization solution for the macroscopic elastic response of isotropic porous elastomers. *Journal of the Mechanics and Physics of Solids 122*, 364–380.

Shulmeister, V., M. W. D. van der Burg, E. van der Giessen, and R. Marissen (1998). A numerical study of large deformations of low-density elastomeric open-cell foams. *Mechanics of Materials 30*, 125–140.

Silberstein, M. N. and M. C. Boyce (2010). Constitutive modeling of the rate, temperature, and hydration dependent deformation response of nafion to monotonic and cyclic loading. *Journal of Power Sources 195*, 5692–5706.

Stoilov, G., V. Kavardzhikov, and D. Pashkouleva (2012). A comparative study of random patterns for digital image correlation. *Journal of Theoretical and Applied Mechanics 42*, 55–66.

Storakers, B. (1986). On material representation and constitutive branching in finite compressible elasticity. *Journal of the Mechanics and Physics of Solids 34*, 125–145.

Sutton, M. A. (2013). Computer vision-based, noncontacting deformation measurements in mechanics: a generational transformation. *Applied Mechanics Reviews 65*, 050802–23.

Sutton, M. A., W. J. Wolters, W. H. Peters, W. F. Ranson, and S. McNeill (1983). Determination of displacements using an improved digital correlation method. *Image and Vision Computing 1*, 133–139.

Tang, M., G. Huang, H. Zhang, Y. Liu, H. Chang, H. Song, D. Xu, and Z. Wang (2017). Dependences of rheological and compression mechanical properties on cellular structures for impact-protective materials. *ACS Omega 2*, 2214–2223.

Thomas, T. Y. (1961). *Plastic Flow and Fracture in Solids*. Academic Press.

Toyjanova, J., E. Hannen, E. Bar-Kochba, E. M. Darling, D. L. Henann, and C. Franck (2014). 3d viscoelastic traction force microscopy. *Soft Matter 10*, 8095.

Triantafyllidis, N. and E. Aifantis (1986). A gradient approach to localization of deformation. i. hyperelastic materials. *Journal of Elasticity 16*, 225 – 237.

Wang, S. and S. Chester (2018). Experimental characterization and continuum modeling of inelasticity in filled rubber-like materials. *International Journal of Solids and Structures 136-137*, 125 – 136.

Wang, Y. and A. M. Cuitiño (2000). Three-dimensional nonlinear open-cell foams with large deformations. *Journal of the Mechanics and Physics of Solids 48*, 961–988.

Wang, Y. and A. M. Cuitiño (2002). Full-field measurements of heterogeneous deformation patterns on polymeric foams using digital image correlation. *International Journal of Solids and Structures 39*, 3777–3796.

Wang, Y., G. Gioia, and A. M. Cuitiño (2000). The deformation habits of compressed open-cell solid foams. *Journal of Engineering Materials and Technology 122*, 376–378.

Wang, Y., P. Lava, P. Reu, and D. Debruyne (2016). Theoretical analysis on the measurement errors of local 2d dic: part i temporal and spatial uncertainty quantification of displacement measurements. *Strain 52*, 110–128.

Westerweel, J. and F. Scarano (2005). Universal outlier detection for piv data. *Experiments in Fluids 39*, 1096–1100.

Widdle Jr., R. D., A. K. Bajaj, and P. Davies (2008). Measurement of the poisson's ratio of flexible polyurethane foam and its influence on a uniaxial compression model. *International Journal of Engineering Science 46*, 31–49.

Xiao, H. (2013). An explicit, direct approach to obtain multi-axial elastic potentials which accurately match data of four benchmark tests for rubbery materials – part 2: General deformations. *Acta Mechanica 224*, 479–498.

Xue, Z., J. J. Charonko, and P. P. Vlachos (2014). Particle image velocimetry correlation signal-to-noise ratio metrics and measurement uncertainty quantification. *Measurement Science and Technology 25*, 115301.

Yang, L. M. and V. P. W. Shim (2004). A visco-hyperelastic constitutive description of elastomeric foam. *International Journal of Impact Engineering 30*, 1099–1110.

Yaofeng, S. and J. H. Pang (2007). Study of optimal subset size in digital image correlation of speckle pattern images. *Optics and Lasers in Engineering 45*, 967–974.

Zhang, J., Z. Lin, A. Wong, N. Kikuchi, V. C. Li, and A. F. Yee (1997). Constitutive modeling and material characterization of polymeric foams. *Journal of Engineering Materials and Technology 119*, 284–291.